2011

FABRICATION AND STUDY OF MOLECULAR DEVICES AND PHOTOVOLTAIC DEVICES BY METAL/DIELECTRIC/METAL STRUCTURES

Bing Hu
University of Kentucky, binghu.hu@gmail.com

Recommended Citation

Hu, Bing, "FABRICATION AND STUDY OF MOLECULAR DEVICES AND PHOTOVOLTAIC DEVICES BY METAL/DIELECTRIC/METAL STRUCTURES" (2011). *University of Kentucky Doctoral Dissertations*. 222.
https://uknowledge.uky.edu/gradschool_diss/222

ABSTRACT OF DISSERTATION

Bing Hu

College of Engineering

University of Kentucky

2011

FABRICATION AND STUDY OF MOLECULAR DEVICES AND PHOTOVOLTAIC DEVICES BY METAL/DIELECTRIC/METAL STRUCTURES

ABSTRACT OF DISERTATION

A dissertation submitted in partial fulfillment of the requirements for the degree of Doctor of Philosophy in the College of Engineering at the University of Kentucky

By

Bing Hu

Lexington, Kentucky

Director: Dr. Bruce J. Hinds, Professor of Materials Engineering

Lexington, Kentucky

2011

ABSTRACT OF DISSERTATION

FABRICATION AND STUDY OF MOLECULAR DEVICES AND PHOTOVOLTAIC DEVICES BY METAL/DIELECTRIC/METAL STRUCTURES

A new class of electrodes with nanometer-scale contact spacing can be produced at the edge of patterned metal/insulator/metal this film structures. A key challenge is to produce insulator layers with low leakage current and have pristine metal contacts for controlled molecular contacts. Atomic layer deposition of high quality Al_2O_3 thin films onto Au electrodes was enabled by surface modification with a self-assembled monolayer of -OH groups that react with a monolayer of trimethylaluminum gas source. Ar ion milling was then used to expose the edge of the Au/dielectric/Au structure for molecular electrode contacts. The junctions are characterized by atomic force microscope and tunnel current properties. The Au/self-assembled monolayer/Al_2O_3/Au tunnel junction, with a very thin oxide insulator layer (15.4 Å), is stable and has a small tunneling current density of about 0.20 ~ 0.75 A/cm^2 at 0.5 V. Organometalic cluster molecules were attached to bridge the electrodes. Through tunnel current modeling, low temperature and photo current measurements, molecular current was found to be consistent with direct tunneling through the organic tethers to available states at the metal center

This novel electrode was also used to study the efficiency of organic conducting thin films where the photovoltaic efficiency can be improved when the electrode separation distance is below the exciton diffusion length. Copper (II) phthalocyanine (CuPc) was thermally evaporated between the nano-gap electrodes formed by Au/Al_2O_3/Au tunnel junctions. A large photocurrent enhancement over 50 times that of bulk CuPc film was observed when the electrode gap distance approached 10 nm. CuPc diffusion length is seen to be 10 nm consistent with literature reports. All devices show diode *I-V* properties due to a large Schottky barrier contact resistance between the small top Au electrode and the CuPc film.

To add another dimension of nm-scale patterning, nanowires can be used as line-of-sight shadowmasks provided that nanowire location and diameter can be controlled. Lateral ZnO nanowires were selectively grown from the edge of a Si/Al_2O_3/Si multi-layer structure for potential integration into devices utilizing Si processing technology. Microstructural studies demonstrate a 2-step growth process in which the tip region, with a diameter ~ 10 nm, rapidly grew from the Al_2O_3 surface. Later a base growth with a diameter ~ 22 nm overgrew the existing narrow ZnO nanowire halting further tip growth. Kinetics studies showed surface diffusion on the alumina seed surface determined ZnO nanowire growth rate.

KEYWORDS: Molecular Devices, Tunnel Junctions, Photovoltaic Devices, Organic Semiconductor, Oxide Nanowires.

Bing Hu

Student's Signature

05/31/2011

Date

FABRICATION AND STUDY OF MOLECULAR DEVICES AND PHOTOVOLTAIC DEVICES BY METAL/DIELECTRIC/METAL STRUCTURES

By

Bing Hu

Director of Dissertation

Bruce J. Hinds, Ph.D

Director of Graduate Studies

Stephen E. Rankin, Ph.D

RULES FOR THE USE OF DISSERTATIONS

Unpublished dissertations submitted for the Doctor's degree and deposited in the University of Kentucky Library are as a rule open for inspection, but are to be used only with due regard to the rights of the authors. Bibliographical references may be noted, but quotations or summaries of parts may be published only with the permission of the author, and with the usual scholarly acknowledgements.

Extensive copying or publication of the dissertation in whole or in part also requires the consent of the Dean of the Graduate School of the University of Kentucky.

A library that borrows this dissertation for use by its patrons is expected to secure the signature of each user.

Name	Date

DISSERTATION

Bing Hu

College of Engineering

University of Kentucky

2011

FABRICATION AND STUDY OF MOLECULAR DEVICES AND PHOTOVOLTAIC DEVICES BY METAL/DIELECTRIC/METAL STRUCTURES

DISSERTATION

A dissertation submitted in partial fulfillment of the requirements for the degree of Doctor of Philosophy in the College of Engineering at the University of Kentucky

By

Bing Hu

Lexington, Kentucky

Director: Dr. Bruce J. Hinds, Professor of Materials Engineering

Lexington, Kentucky

2011

This doctoral study is dedicated to my beloved family members:

My father Jiajiong Hu

My mother Chunyi Han

My wife Zhengchun Lu

& my daughter Sophia Yongxuan Hu

& Victoria Yongting Hu

ACKNOWLEGEMENTS

I deeply appreciate Dr. Bruce J. Hinds, my advisor, for his excellent guidance and support during my graduate study, research work, and dissertation preparation. I am thankful to the Air Force Office of Scientific Research (DEPSCoR) under Agreement No. F49620-02-1-0225, NSF CAREER (Grant No. 0348544), and NSF NIRT (Grant No. 0609064) for funding this dissertation work.

I would like to thank Dr. Chuck May, Zhifang Fan, and Brian Wajdyk for training me and giving me the opportunity to serve and contribute voluntarily in partially maintaining the facility in Center for Nanoscale Science and Engineering (CeNSE). Thanks to Dr. Janet K. Lumpp and Dr. John Bulk for sharing the facility.

I express my thanks to former lab mates, Dr. Nitin Chopra and Dr. Pawan Tyagi, for helping me the start of thesis experiments. I also would like to thank Jingyuan Yao for helping sample preparation and Jonathon Wagner for checking my writings. The valuable discussion and kind help from my lab mates, Dr. Ji Wu, Dr. Xinhua Sun, Dr. Jacob Goldsmith, Xin Zhan, Xin Su, and Karen Gerstandt are highly appreciated.

I am thankful to the Chairman, the Director of Graduate Studies, the Faculties and Staff members (especially Mr. Bruce Cole) of Chemical and Materials Engineering Department for providing various facilities and for their support. Help in electron microscopy work by Larry Rice, Dr. Alen Dozier, and Dr. Jia Ye is also highly appreciated.

I would also like to thank all my Advisory Committee Members, Dr. Stephen E. Rankin, Dr. John Balk, and Dr. Janet K. Lumpp for showing interest in my research work and for their advice and consistent cooperation.

Finally, I am extremely thankful to my parents and my wife, whose blessings and encouragement has always been a part of my life and played a very critical role in getting me so far.

TABLE OF CONTENTS

LIST OF TABLES

LIST OF FIGURES

Chapter 1

Introduction

1.1 Development of Integrated Circuit (IC) industry

In electronics, an integrated circuit (also known as IC, microcircuit, silicon chip, or chip) is a chip of a semiconductor crystal in which many active or passive components have been miniaturized and integrated together to form a sophisticated circuit (1). ICs are widely used in all electronic equipments today and have revolutionized the whole electronic world.

The IC industry has grown rapidly in the past half century. In 1958, Jack Kilby in Texas Instruments demonstrated the first working IC made of germanium. Half a year later, Robert Noyce in Fairchild Semiconductor made the first Silicon IC (2). It was considered to be ridiculously optimistic to achieve a working IC consisting more than dozens of transistors at that time because the yield of each transistor was very low. With the technique development of thin film deposition, photolithography, etching, ion implant, impurity diffusion, and thermal oxidation, the IC industry has experienced four generations:

(1) Small-Scale Integration (SSI) having several transistors, early 1960s to middle 1960s.

(2) Medium-Scale Integration (MSI) having hundreds of transistors, in the late 1960s.

(3) Large-Scale Integration (LSI) having tens of thousands of transistors, in the middle 1970s.

(4) Very Large-Scale Integration (VLSI) having hundreds of thousands of transistors, and beyond, starting in 1980s and continuing through the present.

Since the last quarter of 2009, Intel began revenue production of i-series central processing units (CPUs) based on 32 nm logic technologies and the six-core i7 has over 1 billion transistors (3). Intel is continuing to develop 28 nm technologies for static random access memories (SRAMs) and demonstrated working 22 nm SRAM chips. Recently, Intel proclaimed its new fab building plan at Arizona for 14 nm products. IBM, collaborating with AMD, Samsung, GLOBALFOUNDRIES, and Synopsys, also has developed their own 22 nm technique and is focusing on 14 nm technology development currently.

1.2 Limitation of Moore's Law

Forty years ago, Intel co-founder Gordon Moore stated that the chip density would double every two years (4), as well known as "Moore's Law". Gradually, people have accepted that the transistor's density or clock speed doubles every 18 months. This predictive statement can be observed in Figure 1.1. With the current rate of technological advancement, Moore's Law will be accurate for no more than 15 years before the minimum feature size reaches a molecular scale.

There are several limitations for conventional techniques to decease the feature size beyond 10 nm. The first limitation is the wavelength of the light source. The general photolithography technique can only reach a critical dimension (CD) around 100 nm with a KrCl Excimer laser (157 nm). To reach a CD below 100 nm, E-beam lithography is generally used while its low throughput prevents the applications for mass production. Other options to reach the 10 nm scale include extreme UV lithography ($\lambda \approx$ 10-20 nm) and X-ray lithography ($\lambda <$ 1 nm). However, these techniques have difficulties of exposing radiation focusing, mask materials, and photoresists. Scientists and engineers have made great effort for the extreme UV lithography and SRAMs based on 22 nm technology has been achieved by Intel recently.

The second limitation is the thickness of the insulator layer in the field-effect transistor (FET) polysilicon-gate region. Several years ago, a 2 nm of thermally grown silicon oxide from the current channel was used to insulate the gate current. In order to keep Moore's Law, the oxide layer has had to be attenuated continuously. However, this SiO_2 layer will not insulate effectively if the thickness is below 1.2 nm (5). High-k dielectric gate materials, normally HfO_2, have replaced SiO_2 as the insulating layer between the gate and current channel for Intel 45 nm processor technology. It is assumed that the HfO_2 thickness will approach the limit when the gate length is below 10 nm.

The third limitation is the electromigration of metal lines. This phenomenon will be more obvious when the dimension of metal lines gets smaller. Electromigration can break metal lines or crack the surrounding dielectric (6). Copper is now used instead of aluminum to reduce the electromigration phenomenon but it is not as easily processed as aluminum during fabrication. Considering further advancements in IC fabrication techniques, the fact remains that the technologies and materials currently in use will reach their limits someday in future. Instead of the top-down route, the bottom-up route is another way for device fabrication. More and more scientists have started to focus on the fundamental components such as a single molecule or small groups of molecules to build up working electronic devices.

1.3 Development of molecular devices

Molecular devices can be divided into molecular rectifiers, molecular switches and molecular-scale wires, according to their applications. Carbon nanotubes (CNTs) are also considered as a kind of macro molecules and have become one of the hottest research areas among molecular devices.

1.3.1 Molecular rectifiers

The concept of a molecular device was introduced in 1974. A. Aviram and M.A. Ratner made a historical perspective that the molecule they studied would work as a molecular rectifier (7). Figure 1.2a shows the molecular structure including an acceptor tetracyanoquinodimethane connected by a methylene bridge to a donor tetrathiofulvalene. Theatrical calculations showed that a rectification of current should be possible (Figure 1.2b). In 1997, R.M. Metzger *et al.* observed strong rectification behavior when studying Langmuir-Blodgett (LB) films of ɣ-(n-hexadecyl)quinolinium tricyanoquinodimethanide between metal electrodes (8). In the same year, J. Joachim *et al.* described the first single-molecule electromechanical amplifier consisting of a single C_{60}

molecule between a scanning tunneling microscope (STM) tip and a conductive substrate (9). Their studies show excellent conductance through C_{60} because its molecular orbitals are shifted and broadened when the C_{60} is pressed by the STM tip. A gain of 5 is obtained by comparing the output voltage of 100 mV with the input voltage of 20 mV. $(4\text{-}HOC_6H_4)_5HC_{60}$, a derivative of C_{60}, also shows rectification properties. A maximum rectification ratio of 47.5 was observed for this molecule (10).

1.3.2 Molecular switches

Molecular switches, the possible basic control units in future nano-devices, have been achieved using single molecules (11-14), carbon nanotubes (15), and nanoparticles (16-18). In 1998, S.T. Tans *et al.* fabricated an FET based on a carbon nanotube (15). A single carbon nanotube was connected by two Pt electrodes and the doped Si substrate acted as a back-gate. The experimental *I-V* curves indicate the current flow control by the gate voltage. Coulomb blockade was also observed based on the staircase *I-V* profiles. Recently, a light-driven molecular switch based on azobenzene molecules was reported (19, 20). The trans conformation of azobenzene can be isomerized to the cis conformation with a beam of light with a wavelength of 365 nm and the reverse isomerization happens with a beam of light with a wavelength of 420 nm. The conductance difference between the trans and cis conformations enables the use of the azobenzene and possibly its derivatives as a single-molecule light-driven molecular switch with ON and OFF states. Applications of azobenzene include as photo-switchable molecular glue for DNA to control biological functions (21) and the ionotropic glutamate receptor to control ion channels in cells (22). Many models have been built for molecular devices. For example, Y. Wada has proposed to use polythiophene chains or other molecular wires as the source, drain and gate. The calculated switching speed approaches 1 THz (12). However, the challenge to make reproducible low-resistance contacts to the electrodes prevents their real production.

1.3.3 Molecular wires

Molecular-scale wires are also necessary for future molecular devices. Most researchers in this area are focusing on linear, conjugated oligomers (23-26). Many potential molecules have been synthesized, such as metal-terminated carbon chains (molecule 1 in Figure 1.3) (27), oligomeric linear prophyrin arrays (molecule 2 in Figure 1.3) (28),and oligo(phenylene ethynylene)s (molecule 3 in Figure 1.3) (29, 30). J.R. Reimers *et al.* (31) studied over 100 such molecules as potential molecular wires (for example, molecule 4 in Figure 1.3) and concluded that π delocalization dominates the electronic properties of those systems. Higher delocalization supports longer distance communication between parts of molecules. In 1996, L.A. Bumm *et al.* succeeded in measuring the conductivity of one such molecule (molecule 5 in Figure 1.3) embedded in a self-assembled monolayer (SAM) of dodecanethiolate by STM (26). STM images illustrated that this conjugated organic oligomers have a greater conductivity than dodecanethiolate.

1.3.4 Carbon nanotubes

The carbon nanotube is a very important platform for molecular devices and has many applications. Recently, carbon nanotubes have demonstrated promise for molecular scale wires due to their high conductance. The electrical properties of single-wall carbon nanotubes (SWCNTs) are dependent on their specific chirality and diameter (32, 33). P.J. de Pablo *et al.* characterized SWCNTs distributing between Au electrodes (34). They found that the contact resistance between Au and CNTs is 44 kΩ and the tube resistivity is 0.15 Ω μm^{-1}. These results indicate a great potential of CNTs as molecule-scale wires when the contact problem can be solved.

CNTs are also a good candidate for data storage. In 2000, C.M. Lieber *et al.* proposed a nonvolatile random access memory (RAM) based on a suspended crossbar array of CNTs (35). The status of the crossbar can be switched between suspended (ON) and contact (OFF) states. The ON state shows the domination of a van der Waals interaction between two crossed CNTs by applying voltage pulses of an opposite polarity. The ON state can be switched to the OFF state by applying a larger voltage pulse of an identical polarity. Experiment results show that the bias voltage for switching the crossbar ON is +/-5 V and that for switching OFF is 40 V. Information of ON or OFF of each crossbar can be read by measuring the resistance because the ON resistance is much lower than the OFF resistance. Such RAM devices were calculated to having a density of 10^{12} elements per cm^2 and an operating frequency of 100 GHz.

The most important and promising application of CNTs is their use for mass transport. Our group successfully fabricated the well-ordered nanoporous membranes by incorporating an array of aligned CNTs across a polymer film (36). Extremely high fluid velocities through the aligned CNT membrane were observed because of a frictionless surface at the carbon-nanotube wall (37). For example, the observed water flow velocity is 43.9 cm s^{-1}at 1 bar, which is around 10^5 times larger than the expected value of 5.7×10^{-4} cm s^{-1}. Functionalization molecules were grafted at the entrance to CNTs' cores and work as a gatekeeper for a selective transportation of different molecules (ruthenium bipyridine [Ru-(bipy)$_3^{2+}$] and methyl viologen [MV^{2+}]) (38). These functionalized CNTs membranes have also been employed as the active element of a switchable transdermal nicotine delivery device able to switch between high (1.3 ± 0.65 μmol/hr-cm^2) and low (0.33 ± 0.22 μmol/hr-cm^2) fluxes, which coincides with therapeutic demand levels for nicotine cessation treatment (39).

With rapid development of molecular electronics, devices will become smaller, faster, and more efficient than conventional electronics. We should not be astonished when we hold molecular computers in our hands in several decades.

1.4 Electronic study of molecules

Studying electronic properties of molecules is the fundamental step to approach molecular devices. A variety of techniques, such as Langmuir-Blodgett (LB) film deposition (8, 40-42), scanning probe microscope (SPM) (9, 43, 44), hanging Hg drop electrode (45), metal wire crossing (46), and nanopores (47, 48) have been used to study the electronic transparency of molecules.

The first technique used to study electrical properties of molecules is the Langmuir-Blodgett (LB) method (49). A monolayer of organic materials was deposited between suitable substrates. C.M. Fisher *et al.* (41) used this technique to make Au/LB film/Au structures and measured the tunnel current through octasubstituted palladiumphthalocyanine (PcPd). J.R. Heath *et al.* (42) fabricated tunnel junctions with a structure of Al/Al_2O_3/Rotaxane LB film/Ti/Al and combined them together to obtain

AND and OR logic gates. The idea of hanging Hg drop electrode is similar as the normal LB route. An alkanethiol SAM forms on an Hg drop and builds up the tunnel structure of Hg/SAM/SAM/Hg (45). Thereby, the electric conductance of alkanethiol molecules can be measured. The drawback of the LB film or SAM technique is an easy electrical short between electrodes. B.D. Boer *et al.* (48) developed a new design to support electrodes with patterned photoresist and molecules bridge electrodes *via* pores throughout photoresist. The molecular junctions they made show excellent stability and reproducibility.

To study devices with fewer molecules, J.G. Kushmerick *et al.* (46) covered a Au wire with desired molecules and put another Au wire on it to form a cross-wire tunnel junction. The number of molecules between the crossed wires can be controlled to be around 1000. The distance between top and bottom wires was controlled by a Lorentz force generated by a DC current flowing through one wire in a magnetic field. C. Zhou *et al.* (47) used E-beam lithography and a following plasma etching to open a pore with a diameter of 30 nm in a suspended SiN membrane. Then, a Au film was deposited from the bottom side. No gold particles entered the nanopore because the Au crystallite size of 50 nm is larger than the pore diameter. Finally, a SAM layer of 4-thioacetylbiphenyl formed between Au electrodes through the nanopore.

Among all techniques mentioned in the first paragraph of this section, SPM is the most popular one for molecular study in the past decade. This technology includes scanning tunneling microscope (STM) and atomic force microscope (AFM). This technology uses cantilevers as one electrode with a tip area of 10 ~ 100 nm^2. This decreases the probability of an electrical short dramatically. Another advantage of this method is its ability to probe the electron current through a single molecule (9). However, SPM is only a tool to study molecular electronic properties and can not to be integrated into molecular devices.

1.5 Single molecule devices

Fabricating single molecular devices is a goal for molecular device miniaturization. The main challenge is the precise control of a nano-gap between electrodes. Several techniques, including SPM (9, 43, 50), mechanical break junction (51, 52), electromigration break junction (53-58), tip-end junction (59) and shadow lithography (60), have been developed to fabricate single-molecular-devices (SMD).

SPM is the most popular method to study molecular electrical properties. It is also the first technique to measure a single molecule [46]. The advantage of this SPM technique is getting electrical and morphological information of the studied single molecule simultaneously. STM study on C_{60} is a typical example (9). The C_{60} resistance was about 54.8 MΩ corresponding to an electronic transparency of $T = 2.3\times10^{-4}$. When an increasing compression was applied by the STM tip, the resistance of C_{60} decreased rapidly towards a quantum resistance limit of $R_0 = h/2e^2$ (～12.9 kΩ). The molecular resistance measured by SPM is always larger than the real resistance. This is because a little gap between the tip and the molecule. W. Ho *et al.* used STM to build a metal-molecule-metal junction composed of two chainlike Au clusters and a single Cu(II) phthalocyanine (CuPc) molecule. The CuPc molecule was manipulated by the STM tip to bridge two Au clusters (50). Although the molecular *I/V* properties of this tunnel junction was not studied, this work shows a new insight to fabricate a single molecular device by the STM technique.

The principle of mechanical and electromigration break junction techniques are illustrated in Figure 1.4a & b, respectively. In either case, when a lithographically patterned narrow metal line is broken by a mechanical force or eletromigration, molecules are introduced onto the two clean fracture surfaces to bridge the nano-gap. D.C Ralph *et al.* (53) used the later technique to study two related molecules containing a Co ion and observed the single-electron phenomena of Coulomb blockade and the Kondo effect. His group also realized a control of the electrode spacing *via* a combination of the mechanical and electromigration break junction techniques (52).

The shadow lithography technique is also used to study SMDs. Z. Bao *et al.* prepared tip-end junctions by depositing a Au layer on one side of a tip and evaporating another layer of Au on the other side of the same tip to form a nano-gap (59). T. Bjornholm *et al.* (60) used a suspended mask to cast two Au electrodes with a nano-gap. By using an oblique evaporation angle together with *in situ* conductance measurements, the tunneling gap between two electrodes can be well tuned to a few nanometers. The resistance of a few GΩ at 100K indicates a gap width of 2 nm. Then, molecules were introduced on the electrodes and single molecular transistors were observed.

Although single molecular transistors have been fabricated successfully by those techniques, the risk of electron tunneling through nano-scale metallic islands rather than the single molecule still exists. And, all of these techniques suffer from yield issues.

Therefore, fabricating a gap with a molecular scale without a risk of nano-scale metallic islands and a high yield is of interest in the SMD field.

1.6 Mechanism of electron transport through molecules

Metal/molecules/metal is the basic structure for molecular devices, as shown in Figure 1.5a. When the tunneling current is coherent in the bulk transport, this structure can be considered as a tunnel junction having a uniform barrier layer (Figure 1.5b). The current transport through individual molecules is different from bulk transport because of the inherently small size of molecules. The later part will be introduced in Section 1.6.4.

1.6.1 Bulk current transport through a molecular layer

1.6.1.1 Current tunneling through a potential barrier

To investigate tunneling, consider an electron incident from the top metal electrode to the bottom electrode in Figure 1.6. The barrier layer has a potential energy of V, which profile is give by

$$V = \begin{cases} V_0, & 0 \le x \le a, \\ 0, & x < 0,\ x > a, \end{cases} \tag{1.1}$$

According to the classical physics, the electron will pass the potential barrier with a 100% certainty when the electron energy E is larger than V_0 and the electron will be reflected from the barrier with a 100% certainty when E is smaller than V_0. However, quantum mechanics show a more complicated behavior. Starting with Schrödinger's equation,

$$\left(-\frac{\hbar^2}{2m^*}\frac{d^2}{dx^2}+V(x)\right)\Psi(x)=E\Psi(x), \tag{1.2}$$

In region I ($x < 0$) where $V = 0$, equation (1.2) turns to

$$-\frac{\hbar^2}{2m^*}\frac{d^2}{dx^2}\Psi_1(x)=E\Psi_1(x), \tag{1.3}$$

which has solutions

$$\Psi_1(x)=Ae^{ik_1x}+Be^{-ik_1x}, \tag{1.4}$$

where

$$k_1^2=\frac{2m^*E}{\hbar^2}. \tag{1.5}$$

In region II ($0 \leq x \leq a$) where $V = V_0$, equation (1.2) is

$$\left(-\frac{\hbar^2}{2m^*}\frac{d^2}{dx^2}+V(x)\right)\Psi_2(x)=E\Psi_2(x), \tag{1.6}$$

which has solutions

$$\Psi_2(x)=Ce^{ik_2x}+De^{-ik_2x}, \tag{1.7}$$

where

$$k_2^2=\frac{2m^*(E-V_0)}{\hbar^2}. \tag{1.8}$$

In region III (x > a), equation (1.2) is

$$-\frac{\hbar^2}{2m^*}\frac{d^2}{dx^2}\Psi_3(x)=E\Psi_3(x), \tag{1.9}$$

which has solutions

$$\Psi_3(x) = Fe^{ik_3x} + Ge^{-ik_3x}, \tag{1.10}$$

where

$$k_3^2 = \frac{2m^*E}{\hbar^2} = k_1^2. \tag{1.11}$$

There is no reflection when electrons enter region III, so $G = 0$ and we have

$$\begin{cases} \Psi_1(x) = Ae^{ik_1x} + Be^{-ik_1x} \\ \Psi_2(x) = Ce^{ik_2x} + De^{-ik_2x} \\ \qquad \Psi_3(x) = Fe^{ik_1x} \end{cases} \tag{1.12}$$

Considering the boundary conditions, $\Psi_1 = \Psi_2$ at $x = 0$ and $\Psi_2 = \Psi_3$ at $x = \text{a}$, we have

$$\frac{F}{A} = \frac{4k_1k_2e^{i(k_2-k_1)a}}{(k_1+k_2)^2-(k_1-k_2)^2e^{i2ak_2}} \tag{1.13}$$

So a tunneling probability is defined as

$$T = \left|\frac{F}{A}\right|^2 = \frac{4E(E-V_0)}{V_0^2\sin^2(k_2a)+4E(E-V_0)} \tag{1.14}$$

and a reflection probability is defined as

$$R = \left|\frac{B}{A}\right|^2 = \frac{V_0^2\sin^2(k_2a)}{V_0^2\sin^2(k_2a)+4E(E-V_0)}\ . \tag{1.15}$$

(1.14) can be rewritten as

$$T = \left(1 + \frac{V_0^2}{4E(E-V_0)}\sin^2(k_2a)\right)^{-1} \tag{1.16}$$

When $E > \text{V}_0$, it can be seen that a full transmission occurs when $\text{Sin}(k_2a) = 0$, that is, when

$k_2 = n\pi / a, \quad n = 0, 1, 2, 3, \ldots\ldots$ (1.17)

An important case is when $E < V_0$. This is the general condition for most electronic devices and also the case for our experiments. Therefore,

$$\sin\left(\sqrt{\frac{2m_e^*(E - V_0)}{\hbar^2}}a\right) = \sin\left(i\sqrt{\frac{2m_e^*(V_0 - E)}{\hbar^2}}a\right) = i\sinh\left(\sqrt{\frac{2m_e^*(V_0 - E)}{\hbar^2}}a\right)$$

$$\xrightarrow[a\to\infty]{} \frac{i}{2}e^{\sqrt{\frac{2m_e^*(V_0-E)}{\hbar^2}}a} = \frac{i}{2}e^{\alpha a} \quad (1.18)$$

where $$\alpha = \sqrt{\frac{2m_e^*(V_0-E)}{\hbar^2}} > 0, \quad (1.19)$$

so that $$T \to \frac{16E(V_0-E)}{V_0^2}e^{-2\alpha a}. \quad (1.20)$$

It is clear that the tunneling probability T is exponentially decaying as a function of the barrier width a. And this explains why the tunneling can become a significant problem when the gate oxide layer is very thin for metal-oxide-semiconductor field effect transistors (MOSFETs).

1.6.1.2 Molecular conductance by coherent tunneling

The current passing through molecules is affected by many factors. These factors can be divided into two groups. The intrinsic factors include molecular length, conformation, and highest occupied molecular orbital-lowest unoccupied molecular orbital (HOMO-LUMO) gap. The extrinsic factors include the electrode work function and the contact between molecules and electrodes.

Considering the coherent tunneling current, conductance G of the metal/molecule/metal junction can be described by the Landauer formula $^{(61)}$:

$$G = \frac{2e^2}{h}T \tag{1.21}$$

where T is the tunneling probability introduced in Section 1.6.1.1 and can be divided into three components:

$$T = T_{tc} \bullet T_{bc} \bullet T_{mol} \tag{1.22}$$

where T_{tc} and T_{bc} gives the efficiency of electron transport across the top and bottom contacts in Figure 1.5a. T_{mol} gives the efficiency of electron transport across the molecule which can be considered as a rectangular barrier introduced in Section 1.6.1.1. Here, T_{mol} is simplified from (1.19) and given by

$$T_{mol} = e^{(-\beta l)} \tag{1.23}$$

where l is the length of the molecule, similar as the potential barrier width a in Figure 1.6. In equation (1.18), ($V_0 - E$) is the energy gap between the particle or electron in Figure 1.6. When no bias is applied on molecules, the energy gap is ϕ, where ϕ is the barrier height for tunneling through LUMO ($\phi = (E_F - E_{LUMO})$) or through HOMO ($\phi = (E_{HOMO} - E_F)$), E_F is the Fermi level of the electrode. Figure 1.7a shows the schematic energy diagram and ϕ is set as ($E_{HOMO} - E_F$). When a bias V is applied on molecules, the average energy gap will turn to ($\phi - (eV/2)$), as shown in Figure 1.7b. Therefore, the tunneling decay parameter β is derived from (1.19) and given by:

$$\beta = 2\sqrt{\frac{2m_e^*(\phi-(eV/2))}{\hbar^2}} \tag{1.24}$$

B. Boer *et al.* summarized the study of molecular conductance and plotted the single alkane-based molecular resistance with the number of carbon atoms present in the alkane chain (62). Three large clusters of data were found to be compiled from different measurement methods. The low contact resistance group consists of STM and CP-AFM measurements, with alkanedithiol molecules chemically bonded to both electrodes, having small T_{tc} and T_{bc}. The medium contact resistance group consists of measurements on larger device areas with only one end of the molecule chemisorbed at the electrode. And, the large contact resistance group is composed of molecules without any chemistry adsorption on electrodes. All three groups show a similar exponential increase of resistance when increasing alkane chain length. The β has a value of 0.7 ~ 1.1 $Å^{-1}$.

Figure 1.8 (63) shows possible paths for current transport through molecular junctions. They are through-bond tunneling (I), through-space tunneling (II) and a combination of both (III). Lots of experiments prove that the dominant current transport is through-bond tunneling, in which the electrons follows the bond overlaps along the molecules (64).

It's well known that the current through conjugated molecules is much higher than that through saturated molecules with a similar length. The current difference is generally on the order of 1-1.5 (65). The main reason is the smaller ϕ of the π-bond of conjugated molecules (about 3 eV) compared with ϕ of the σ-bond of saturated ones (about 8 eV). This results in a tunneling decay parameter β of 0.2-0.6 $Å^{-1}$ for π-bond molecules and 0.6-1.0 $Å^{-1}$ for σ-bond molecules, according to formula (1.24) (63).

1.6.1.3 Simmons model

The tunneling decay parameter β is used to describe the transmittance property of a molecule. This part has been introduced in last section. To describe the insulating property of a dielectric layer, a barrier thickness (Å or nm) and a barrier height (eV) are generally used, especially for tunnel junctions. There are many simulation models and Simmons model (66) is the most popular one used for tunnel junctions.

The electron can pass through a tunnel junction in two ways: (1) The electron has enough thermal energy to overcome the potential barrier and flow in the conduction band; (2) The barrier is thin enough for the electron to penetrate by an electric tunnel effect. In this section, only the tunneling effect is considered.

Assuming an electron can penetrate a potential barrier of height $V(x)$ in the x direction, as shown in Figure 1.9, its penetration probability $D(E_x)$ is given by the Wentzel–Kramers–Brillouin (WBK) approximation (67):

$$D(E_x) = \exp\left\{-\frac{4\pi}{h}\int_{s1}^{s2}[2m(V(x)-E_x)]^{\frac{1}{2}}\,dx\right\} \tag{1.25}$$

where $E_x = mv_x^2/2$, and is the incident electron energy in the x direction. Therefore, the number N_1 of the electrons tunneling through this barrier from left electrode to right electrode is given by

$$N_1 = \int_0^{v_m} v_x n(v_x)\, D(E_x) dv_x = \frac{1}{m}\int_0^{E_m} n(v_x)\, D(E_x) dE_x \tag{1.26}$$

where E_m is the maximum energy of electrons in the electrode, and the $n(v_x)dv_x$ is the electron number per unit with a velocity from v_x to v_x+dv_x. The velocity distribution of electrons in the electrodes is considered to be isotropic. The electron number per unit with a velocity between a usual infinitesimal limits is given by

$$n(v)dv_x\, dv_y dv_z = \left(\frac{2m^4}{h^3}\right) f(E)dv_x\, dv_y dv_z \tag{1.27}$$

where $f(E)$ is the Fermi-Dirac distribution function. Therefore, from Equation (1.27)

$$n(v_x) = \frac{2m^4}{h^3} \iint_{-\infty}^{\infty} f(E)dv_y dv_z = \frac{4\pi m^2}{h^3} \int_0^{\infty} f(E)dE_r \tag{1.28}$$

where $v_r^2 = v_y^2 + v_z^2$, $E_r = mv_r^2/2$. Substituting Equation (1.28) in Equation (1.26) yields

$$N_1 = \frac{4\pi m^2}{h^3} \int_0^{E_m} D(E_x)\, dE_x \int_0^{\infty} f(E)dE_r \tag{1.29}$$

In a similar manner, if a positive potential V is applied on the right electrode in Figure 1.9, the tunnel probability $D(E_x)$ from the right electrode to the left electrode is given

$$N_2 = \frac{4\pi m^2}{h^3} \int_0^{E_m} D(E_x)\, dE_x \int_0^{\infty} f(E+eV)dE_r \tag{1.30}$$

Therefore, the total flow of electrons N through the barrier is

$$N = N_1 - N_2 = \frac{4\pi m^2}{h^3} \left\{ \int_0^{\infty} [f(E) - f(E+eV)]dE_r \;\right\} \times \int_0^{E_m} D(E_x)\, dE_x \tag{1.31}$$

We define

$$\gamma = \frac{4\pi m^2}{h^3}\int_0^{\infty}[f(E) - f(E + eV)]dE_r \tag{1.32}$$

Therefore, we have

$$J = \int_0^{E_m} D(E_x)\,\gamma dE_x \tag{1.33}$$

In Figure 1.9, $V_x = \eta + \varphi(x)$, Equation (1.25) becomes

$$D(E_x) = \exp\left\{-\frac{4\pi}{h}(2m)^{\frac{1}{2}}\int_{s1}^{s2}[\eta + \varphi(x) - E_x]^{\frac{1}{2}}\,dx\right\} \approx \exp\left[-A(\eta + \bar{\varphi} - E_x)^{\frac{1}{2}}\right] \tag{1.34}$$

where $\bar{\varphi}$ is the mean barrier height above Fermi level of the negatively biased electrode and defined by $\bar{\varphi} = \frac{1}{\Delta s}\int_{s1}^{s2}\varphi(x)\,dx$, and $A = (4\pi\beta\Delta s/h)\,(2m)^{1/2}$. Here, β is generally close to 1. When the temperature is 0K, we have

$$\gamma = \begin{cases} \left(\frac{4\pi me}{h^3}\right)(eV), & 0 < E_x < \eta - eV \\ \left(\frac{4\pi me}{h^3}\right)(\eta - E_x), & \eta - eV < E_x < \eta \\ 0, & E_x > \eta \end{cases} \tag{1.35}$$

Substituting Equations (1.34) & (1.35) in Equation (1.33) yields

$$J = \frac{4\pi me}{h^3}\left\{eV\int_0^{\eta-eV} \exp\left[-A(\eta+\bar{\varphi}-E_x)^{\frac{1}{2}}\right] dE_x - \bar{\varphi}\int_{\eta-eV}^{\eta} \exp\left[-A(\eta+\bar{\varphi}-E_x)^{\frac{1}{2}}\right] dE_x + \int_{\eta-eV}^{\eta} (\eta+\bar{\varphi}-E_x)\times \exp\left[-A(\eta+\bar{\varphi}-E_x)^{\frac{1}{2}}\right] dE_x\right\} \quad (1.36)$$

The first part of the integrals yields

$$\left(\frac{8\pi meV}{h^3A^2}\right)\left\{\left[A(\bar{\varphi}+eV)^{\frac{1}{2}}+1\right]\exp\left[-A(\bar{\varphi}+eV)^{\frac{1}{2}}\right] - \left[A(\bar{\varphi}+\eta)^{\frac{1}{2}}+1\right]\exp\left[-A(\bar{\varphi}+\eta)^{\frac{1}{2}}\right]\right\}$$

(1.37)

Because the second term << first term and $A(\bar{\varphi}+eV)^{\frac{1}{2}}$ >> 1, Equation (1.37) turns into

$$\left(\frac{8\pi me^2}{h^3A}\right)V(\bar{\varphi}+eV)^{\frac{1}{2}}\exp\left[-A(\bar{\varphi}+\eta)^{\frac{1}{2}}\right] \quad (1.38)$$

The second part of the integrals has a similar form as the first part. Therefore,

$$\left(\frac{8\pi me}{h^3A^2}\right)\bar{\varphi}\left\{\left[A\bar{\varphi}^{\frac{1}{2}}+1\right]\exp\left(-A\bar{\varphi}^{\frac{1}{2}}\right) - \left[A(\bar{\varphi}+eV)^{\frac{1}{2}}+1\right]\exp\left[-A(\bar{\varphi}+eV)^{\frac{1}{2}}\right]\right\} \quad (1.39)$$

The third part of the integrals has the form

$$\int z^2e^{-Az}dz = -e^{-Az}\left(\frac{z^3}{A}+\frac{3z^2}{A^2}+\frac{6z}{A^3}+\frac{6}{A^4}\right) \quad (1.40)$$

where $z^2 = \eta+\bar{\varphi}-E_x$. The third and fourth terms in the parentheses are negligible comparing with the first two terms. Therefore, Equation (1.40) turns into

$$\left(\frac{8\pi me}{h^3 A}\right)\left\{\bar{\varphi}^{\frac{1}{2}} \exp\left(-A\bar{\varphi}^{\frac{1}{2}}\right) - (\bar{\varphi} + eV)^{\frac{1}{2}} \exp\left[-A(\bar{\varphi} + eV)^{\frac{1}{2}}\right]\right\} +$$

$$\left(\frac{24\pi me}{h^3 A^2}\right)\left\{\bar{\varphi} \exp\left(-A\bar{\varphi}^{\frac{1}{2}}\right) - (\bar{\varphi} + eV) \exp\left[-A(\bar{\varphi} + eV)^{\frac{1}{2}}\right]\right\}$$

(1.41)

Substituting Equations (1.38), (1.39), and (1.41) in Equation (1.36) yields

$$J = J_0 \left\{\bar{\varphi} \exp\left(-A\bar{\varphi}^{\frac{1}{2}}\right) - (\bar{\varphi} + eV) \exp\left[-A(\bar{\varphi} + eV)^{\frac{1}{2}}\right]\right\} \tag{1.42}$$

where $J_0 = e/2\pi h(\beta \Delta s)^2$.

Generally, the tunnel junctions are considered as a rectangular potential barrier, as shown in Figure 1.7a. In this dissertation, the dielectric layer between electrodes is aluminum oxide. The barrier height of aluminum oxide is typically ranging from 1 eV to 3 eV (68). The typical applied voltage V is from 0.1 V to 0.5 V, smaller than φ/e. Figure 1.7b shows the schematic energy diagram in this intermediate-voltage range: $V < \varphi/e$. Therefore, $\Delta s = s$ and $\bar{\varphi} = (\varphi - \frac{eV}{2})$. Substituting these values to Equation (1.42), the observed current density J is described as

$$J = \frac{e}{2\pi h(\beta s)^2}\left\{\left(\varphi - \frac{eV}{2}\right) \exp\left[-\frac{4\pi\beta s}{h}(2m)^{\frac{1}{2}}\left(\varphi - \frac{eV}{2}\right)^{\frac{1}{2}}\right]\right.$$

$$\left. - \left(\varphi + \frac{eV}{2}\right) \exp\left[-\frac{4\pi\beta s}{h}(2m)^{\frac{1}{2}}\left(\varphi + \frac{eV}{2}\right)^{\frac{1}{2}}\right]\right\}$$

(1.43)

where e is electron charge, h is Planck's constant, φ is the barrier height, s is the barrier thickness, V is the applied bias and β is a parameter determined by the tunnel junction properties and the applied bias V. Here, β equals to 1. Simmons fitting is used to figure the insulating properties of most devices in this dissertation.

1.6.1.4 Coulomb blockade

The most popular structure of molecular devices is metal/molecules/metal. When the size of electrodes shrinks to a nanoscale, Coulomb blockade will become a fundamental effect. To simply this problem, consider two electrodes separated by an insulator layer first. The charge and voltage are proportional following

$$Q = C\,V, \tag{1.44}$$

where Q is the charge on the electrodes, C is the capacitance, and V is the voltage between two electrodes. The electrostatic energy stored in this capacitor is

$$E = C\,V^2 = Q^2 / 2\,C. \tag{1.45}$$

The simplest capacitor is formed by two parallel plates of a area A and a distance d. For this configuration,

$$C = \varepsilon\,A / d, \tag{1.46}$$

where ε is the permittivity of the material between two plates. Table 1.1 shows the capacitance values and energy change due to the transfer of a single electron through a nano- or micro-capacitor. Here, a vacuum is assumed between two electrodes ($\varepsilon = \varepsilon_0$).

When the tunneling area is 10 μm × 10 μm, the change in energy due to the transfer of a single electron (ΔE) is only 1.8×10^{-7} eV and is negligible. Coulomb blockade becomes obvious when the tunneling area decreases to 5 nm × 5 nm. 0.73 V is needed to apply on electrodes for a single electron to transport, as shown in Figure 1.10. J. Park *et al.* put $[Co(tpy\text{-}(CH_2)_5\text{-}SH)_2]^{2+}$ molecules between nanoscale Au electrodes and the I-V curves show the coulomb blockade phenomenon at the room temperature (53).

Temperature plays an important role in Coulomb blockade effect. Thermal energy is available when $T > 0$ K. To keep ΔE much larger than the thermal energy,

$$\frac{q_e^2}{2C} \gg \frac{1}{2} k_B T, \tag{1.47}$$

or

$$C \ll \frac{q_e^2}{k_B T}, \tag{1.48}$$

is needed to be satisfied to observe the Coulomb blockade, where k_B is Blotzmann's constant. For the nanocapacitor in Table 1.1, $T << 1.7 \times 10^5$ K, is the lab condition. However, for the microcapacitor in Table 1.1, $T << 4.3 \times 10^{-3}$ K, is very difficult to achieve.

1.6.2 Current transport through a single molecule

1.6.2.1 Double barrier tunneling

A single molecule bridging two electrodes acts as a quantum dot. This metal/single molecule/metal system can be simulated as a double barrier tunnel junction, as shown in Figure 1.11a&b. The analysis of the double barrier tunnel junction is same as procedures at Section 1.6.1.1. The only difference is that five regions should be considered and four interfaces match boundary conditions. The result for the transmission coefficient of the double barrier system in Figure 1.11b is

$$T = \left(1 + \frac{4R_1}{T_1^2} \sin^2(k_1 L - \theta)\right)^{-1}, \tag{1.49}$$

where R_1 and T_1 are the transmission and reflection coefficient for a single barrier of a width a, given by (1.15) and (1.14), respectively. L is the length of the well between barriers, and

$$\tan\theta = \frac{2k_1 k_2 \cos(k_2 a)}{(k_1^2 + k_2^2)\sin(k_2 a)}, \tag{1.50}$$

where

$$k_1^2 = \frac{2m_e^* E}{\hbar^2}, \quad k_2^2 = \frac{2m_e^*(E - V_0)}{\hbar^2}. \tag{1.51}$$

From (1.30), T will become unity when

$$\sin(k_1 L - \theta) = 0 \quad \Longrightarrow \quad k_1 L - \theta = n\pi, \;\; n = 0, 1, 2, \ldots. \tag{1.52}$$

For a simple case, assume that $V_0 \gg E$, so $|k_2| \gg |k_1| \Longrightarrow \tan\theta \to 0 \Longrightarrow \theta \to 0$, leading to $k_1 L = n\pi$. Putting this result into (1.51), we have

$$E = E_n = \frac{\hbar^2}{2m_e^*}\left(\frac{n\pi}{L}\right)^2, \tag{1.53}$$

which is exactly same as the result for quantized energy levels in a one-dimensional quantum well (69). Equation (1.53) reveals that transmission of the particle in Figure 1.10b reaches maximum when $E = E_n$, which is defined as the quasi-bound state of the well in the double barrier system.

1.6.2.2 Coulomb blockade in a double junction system

Coulomb blockade also happens for the double barrier tunnel junction with a sufficiently low temperature or a small capacitance described in Section 1.6.1.4. Figure 1.12 shows the equivalent circuit of a metal/single molecule/metal structure. For each tunnel junction, we have

$$Q_a = C_a V_a,\ Q_b = C_b V_b \,. \tag{1.54}$$

So the energy stored in the capacitors is

$$E_s = \frac{Q_a^2}{2C_a} + \frac{Q_b^2}{2C_b} = \frac{1}{2}\left(C_a V_a^2 + C_b V_b^2\right). \tag{1.55}$$

For the circuit, we have

$$\begin{cases} Q = Q_b - Q_a = nq_e \\ \quad V_s = V_a + V_b \\ \quad C_s = C_a + C_b \end{cases} \Longrightarrow \begin{cases} V_a = \frac{1}{C_s}\left(V_s C_b - nq_e\right) \\ V_b = \frac{1}{C_s}\left(V_s C_a + nq_e\right) \end{cases}. \tag{1.56}$$

Therefore, equation (1.55) can be written as

$$E_s = \frac{1}{2C_s}\left(C_a C_b V_s^2 + (nq_e)^2\right) \,. \tag{1.57}$$

Assume that there are *n* electrons on the single molecule and let one electron tunnel onto the molecule through junction b. From equation (1.56), the voltage change in junction *a* and *b* is

$$\Delta V_a = \Delta V_b = \frac{q_e}{C_s}\,. \tag{1.58}$$

At the same time, the charge change in junction *a* is

$$\Delta Q_a = C_a \Delta V_a = \frac{C_a q_e}{C_s}\,, \tag{1.59}$$

and the associated work done by the power supply is

$$W = \Delta Q_a V_s = \frac{C_a q_e}{C_s} V_s\,. \tag{1.60}$$

So, the total energy change when the electron is tunneling through junction b is

$$\Delta E = \Delta E_s - W$$

$$= \frac{1}{2C_s}\left(C_a C_b V_s^2 + (n q_e)^2\right) - \frac{1}{2C_s}\left(C_a C_b V_s^2 + \left((n+1) q_e\right)^2\right) - \frac{C_a q_e}{C_s} V_s\,. \tag{1.61}$$

The energy change should be positive ($\Delta E > 0$) and we have

$$V_s > \frac{-q_e}{C_a}\left(n + \frac{1}{2}\right). \tag{1.62}$$

Using the same procedures to deal with the electron tunneling off the molecule through junction a, we have

$$V_s > \frac{q_e}{C_b}\left(n - \frac{1}{2}\right). \tag{1.63}$$

For a symmetrical molecule, $C_a = C_b = C$. And if $n = 0$, we would get

$$|V_s| > \frac{|q_e|}{2C} \Longrightarrow E_c = \frac{q_e^2}{2C}\,, \tag{1.64}$$

same as the Coulomb blockade for the single capacitor in (1.45).

Now considering one electron already tunneling onto the molecule through junction *b*, a second electron tunnels onto the molecule through junction *b*, the energy change should be

$$\Delta E = \frac{1}{2C_s}\left(C_a C_b V_s^2 + \left((n+1)q_e\right)^2\right) - \frac{1}{2C_s}\left(C_a C_b V_s^2 + \left((n+2)q_e\right)^2\right) - \frac{C_a q_e}{C_s} V_s\,, \tag{1.65}$$

and enforcing $\Delta E > 0$ with special conditions ($C_a = C_b = C$ and $n = 0$) leads to

$$|V_s| > \frac{3|q_e|}{2C}\,. \tag{1.66}$$

In general, we have

$$|V_s| > \frac{(2m-1)|q_e|}{2C}\,, \tag{1.67}$$

where $m = 1, 2, 3, \ldots$, for 1, 2, 3, … electron tunneling events, respectively. Therefore, if electrons are tunneling through the single molecule one by one in Figure 1.12a, the *I-V* curve will show discrete voltage steps called a *Coulomb staircase*, as shown in Figure 1.13. R.C. Jaklevic *et al.* (70) used the STM technique to observe this phenomenon for an In droplet at 4.2 K, which worked as a quantum dot. R. Negishi *et al.* (71) put a Au nanoparticle between an electrode gap with a 10 nm scale and observed the Coulomb steps at 10 K. Y. Wakayama *et al.* (72, 73) deposited a porphyrin derivative molecule between SiO_2 layers to form a double-barrier tunneling junction. consisting of a

Si/SiO2/molecule/SiO2/Au structure. *I–V* characteristics of the Si/SiO2/molecule/SiO2/Au structure show a Coulomb staircase.

1.6.2.3 Electron transport through a single molecular transistor

The properties of a metal/single molecule/metal structure can be better controlled when a gate terminal covered with an insulating layer is added below the single molecule, as shown in Figure 1.14. This device is called a single molecular transistor. The gate voltage V_g is used to control the HOMO or LUMO level of this molecule. Therefore, the source-drain voltage V_s required to drive a current through the transistor can be controlled by V_g.

Following all procedures in the previous section, we have

$$\begin{cases} Q_a = C_a V_a, \; Q_b = C_b V_b, \; Q_g = C_g\left(V_g - V_b\right), \\ Q = Q_b - Q_a - Q_g = nq_e \,, \\ V_s = V_a + V_b, \; V_g = V_{gg} + V_b, \end{cases} \tag{1.68}$$

and can derive the energy stored in the capacitors is

$$E_s = \frac{Q_a^2}{2C_a} + \frac{Q_b^2}{2C_b} + \frac{Q_g^2}{2C_g} = \frac{1}{2C_s}\left(C_g C_a\left(V_s - V_g\right)^2 + C_a C_b V_s^2 + C_b C_g V_g^2 + Q^2\right), \tag{1.69}$$

where $C_s = C_a + C_b + C_g$.

Assume that an electron tunnels through junction b onto the HOMO or LUMO level of this molecule, the change of the total energy should be

$$\Delta E = \Delta E_s - \left(W_a + W_g\right) > 0$$

$$\Rightarrow \frac{1}{2C_s}(nq_e)^2 - \frac{1}{2C_s}\left((n+1)q_e\right)^2 - \frac{C_a q_e}{C_s} V_s - \frac{C_g q_e}{C_s} V_g > 0$$

$$\Rightarrow q_e\left(n+\frac{1}{2}\right)+C_aV_s+C_gV_g>0. \tag{1.70}$$

In a same way, when an electron on the HOMO or LUMO level of this molecule tunnels off the molecule through junction *a*, we can get

$$q_e\left(-n+\frac{1}{2}\right)+V_s\left(C_b+C_g\right)-C_gV_g>0. \tag{1.71}$$

At the initiation of current flow, there is no charge on the molecule (*n*=0). Therefore, the first electron tunnels into the molecule through junction *b* and we have

$$V_s>\frac{1}{C_a}\left(\frac{-q_e}{2}-C_gV_g\right) \tag{1.72}$$

derived from equation (1.70). Now *n* = 1 and the electron tunnels off the molecule through junction a. We can get

$$V_s>\frac{1}{C_b+C_g}\left(\frac{q_e}{2}+C_gV_g\right) \tag{1.73}$$

derived from equation (1.71).

Now there is an electron on the molecule. If a second electron want to tunnels through junction *b* onto the molecule and tunnels through junction *a* off the molecule, we can get

$$\begin{cases} V_s>\frac{1}{C_a}\left(\frac{-3q_e}{2}-C_gV_g\right) \\ V_s>\frac{1}{C_b+C_g}\left(\frac{3q_e}{2}+C_gV_g\right) \end{cases}, \tag{1.74}$$

similar as the equation (1.66) introduced in Section 1.6.2.2. Continuing in this manner and considering the opposing tunneling conditions, we can obtain the Coulomb diamonds shown in Figure 1.15. These special diamond patterns are the proof for single molecular transistors (53-55, 60, 74).

1.7 Organic semiconductor

An organic semiconductor is an organic material showing semiconductor properties. Organic semiconductors are composed of conjugated molecules, oligomers and polymers where electrons or holes can transport *via* π-electron overlapping with hopping and tunneling processes. Organic semiconductors have become an attractive research area with their potential application in organic solar cells with very large area production techniques similar to what has produced 'Saran wrap'.

1.7.1 Organic solar cells

Organic solar cells (OSCs) have attracted a great deal of attention because of their low production cost, inexpensive substrates and robust mechanical flexibility (75-78). However, the power conversion efficiency of OSCs are very low (normally 3~5%) (79) and hinders their widespread applications. The power conversion process in OSCs has three main steps: exciton generation by optical absorption, exciton dissociation into carriers, and carrier collection at the electrodes. Because organic semiconductors have highly localized states, generally, only a small fraction of the excitons generated by light near the donor-acceptor interface contribute to the final photocurrent because the thickness of organic polymers between electrodes is far larger than the exciton diffusion lengths (close to or below 10 nm) of these materials (80-82). Most electrons recombine with holes rather than reaching the donor-acceptor interface or electrodes. It is hypothesized that OSCs' photovoltaic efficiency can be much improved when the carrier travel distance is controlled below 10 nm scale. However, it is challenging to fabricate large area ultrathin cells (organic layer thickness less than 10 nm) between two thick electrodes without electrical shorts. Ultra-high-voltage organic molecular beam evaporation (UHV-MBE) has been used to build a donor-acceptor multiple heterojunction device (each layer thinner than 10 nm). This device showed a high external quantum efficiency of ~ 75% under an applied field (75). A more common way to reduce the travel distance of electron-hole pairs is by blending donor and acceptor layers. Using this technique, the quantum efficiency of bulk heterojunctions (83, 84) has been greatly improved. And power conversion efficiencies over 5% for metal phthalocyanine (MePc) based OSCs (85) and 7% for thieno[3,4-b]thiophene and benzodithiophene polymers (PTBs) based OSCs (86) have been realized . The interdigitated morphology (87) of bulk heterojunctions is composed of well-organized nano-structures considered to be the ideal structure for OSCs. However, these structures are difficult to fabricate over large areas because of poor controllability of polymers.

In this dissertation, we deposited the organic semiconductor between nano-gap electrodes at the exposed edge of a metal/dielectric/metal structure. The carrier travel distance can be controlled below 10 nm and a great photovoltaic enhancement was detected.

1.7.2 Organic materials in organic solar cells

Organic materials in OSCs are divided into two groups: hole-conducting materials (*p*-type) working as the electron donor and electron-conducting materials (*n*-type) working as the electron acceptor. A donor layer and an acceptor layer are generally deposited together between electrodes to get a high dissociation efficiency for electron-hole pairs in the sun light. Metal Phthalocyanine (MePc), poly(*p*-phenylenevinylene) (PPV) and its derivatives, and poly(3-hexylthiophene-2,5-diyl) (P3HT) are the popular electron donors; Perylene, buckminster fullerene C_{60} and its derivatives are the popular electron accepters (Figure 1.16).

At the beginning of solar cell development, MePc and Perylene were often incorporated into evaporated solar cells because of their stability and facile deposition by thermal evaporation (88, 89). The low charge carrier mobility in these materials makes them be regarded as insulators. To increase the charge carrier concentration, MePc was exposed to oxygen or strong oxidizing agents such as iodine (89, 90) while Perylene was exposed to hydrogen (90). The final doped MePc/Perylene bilayer devices can work as classical *p-n* junctions (91-93). In this dissertation, Copper Phthalocyanine (CuPc) was used as the organic material for the photocurrent study in Chapter 5.

In 1992, the photo-induced charge transfer from a conjugated polymer to a C_{60} layer was first reported by Sariciftci *et al* (94). Since then, the polymer-fullerene devices become the most popular solar cells for research. In 1995, Yu et al. used a blend of 2-methoxy-5-(2-ethylhexyloxy)-polyphenylenevinylene (MEH-PPV) and [6,6]-phenyl C_{61} butyric acid methyl ester (PCBM, a kind of C_{60} derivative) to build the bulk heterojunction (BHJ) and got a power efficiency of ~ 1%. This is a major breakthrough for OSCs (83). Today, organic photovoltaics are presented by BHJ OSCs based on P3HT and PCBM materials. The efficiency of these BHJ OSCs ranges from 4-5% (95-99). However, this P3HT:PCBM system is already approaching optimal device performance considering the poor material mobility properties. To improve OSCs efficiency further towards 10%, new materials and nm-scale electrode geometries are needed. For instance an array of nanoscale interpenetrating bicontinous network of p-n materials can have the appropriate electrodes within the exciton diffusion length.

1.8 The novel design of a metal/insulator/metal structure towards molecular devices

Considering the precise control of film thickness with angstrom-level by film deposition, our group has developed a novel and simple method to fabricate nano-gap electrodes with the critical dimension based on easily controlled insulator film thickness (100). As shown in Figure 1.17, a metal wire (5 μm wide, 10 nm thickness) as the bottom electrode was deposited first and another wire (5 μm wide, alumina 2nm/metal 10 nm) as the top electrode was deposited across the bottom electrode by a lift-off process. Then, molecules were introduced to bridge the top and bottom electrodes at the exposed edge of metal/dielectric/metal structure. For Ni/Al_2O_3/Au samples, the current increased after molecules attachment and returned to the background level after disconnecting molecules to the Au electrode by thiol-exchange reaction. The same reversible behavior was observed after the cycle was repeated. This control experiment illustrates that the increased current passes through molecules bridging two electrodes and do not originated from the random breakdown of electrodes. Simmons fitting analysis shows the molecular barrier thickness of ~ 1 nm and the molecular barrier height of ~ 0.7 eV, respectively.

The most obvious advantage for our fabrication method is the precise control of gap distance between two electrodes. The gap between electrodes is controlled by the dielectric film thickness. This can be controlled in an angstrom scale by a normal deposition process. This fabrication process is more stable and convenient than all techniques mentioned in chapter 1.5. Our molecular devices are also a type of reversible sensing devices. Molecules locating on the exposed metal surface are easily modified or exchanged.

1.9 Challenges

The nano-gap formed at the exposed edge of a metal/dielectric/metal structure is a good platform to study molecular conduction. The lift-off method is simple and has a low cost. But the repeatability of those experiments (100) is very poor. Several problems lead to this poor repeatability.

The lift-off process is a popular method used in university labs to pattern thin films. A good edge profile of thin films can be obtained when an anisotropic deposition or line-of-sight (e.g., thermal evaporation or e-beam evaporation) is executed on a photoresist film with an undercut profile. The sputtering process used in those experiments is not a good anisotropic deposition technique. Particles of desired materials easily adhere on the sidewall of the photoresist layer. Therefore, notches are generally formed at the edge of deposited thin film after a lift-off process, as shown in Figure 1.18a. These notches at the edge of the bottom electrodes will short the metal/dielectric/metal tunnel junctions. These notches also form at the edge of the top electrode using the same sputtering and lift-off processes. The dielectric layer covering the sidewall of the top electrode, as shown in Figure 1.18b, will impede molecules to bridge the top and bottom electrodes.

The Ni and NiFe used for electrode material is another problem. It is very difficult to keep a vacuum or a protective gas circumstance to prevent these metal materials from oxidization during the device fabrication. Therefore, an oxide layer forms at the surface of Ni or NiFe electrodes. This oxide layer will impede molecules to attach on electrodes.

1.10 Goals of this work

The major goal of this dissertation is fabricating molecular molecular electrodes with sub-nm dimensional control with a high repeatability and study molecular conduction mechanism through the well established Au-thiol connection. The nano-gap electrodes for molecular attachment are formed at the exposed edge of metal/dielectric/metal trilayer structures. To reach this goal, two problems mentioned in Section 1.9 have to be solved. Etching processes, including dry etching and wet etching, are applied to obtain a good profile of top and bottom electrodes. Chapter 2 will introduce this part of work and show the *I-V* property improvements of tunnel junctions. Pure Au is used to replace NiFe or Ni as the electrode material to eliminate the oxide layer forming on the electrode surface. This is a significant materials challenge to prepare Au/oxide/Au tunnel junctions. Due to surface energy mismatch, there is island growth instead of a continuous thin film growth of the oxide on Au electrodes. This will short with the top Au electrode easily. Chapter 3 will introduce a novel technique developed by our group to fabricate Au tunnel junctions with a lowest leakage current density in the world. Several molecules were tried to bridge the top and bottom electrodes. Control experiments and low temperature experiments were also executed to study these molecular devices. This part of work will be introduced in Chapter 4.

The nano-gap Au electrodes are also a good substrate to study photovoltaic materials in a nano-scale. It is assumed that the photovoltaic efficiency will be enhanced greatly when the travel distance of excited electron-hole pairs is less than the exciton diffusion length of the photovoltaic materials, which are mostly around 10 nm. The nano-gap Au electrodes at the exposed edge of Au/Al_2O_3/Au structures provide a way to prove this assumption. Therefore, another goal of this dissertation is studying photovoltaic properties of organic semiconductors between nano-gap electrodes. Chapter 5 will show the study of photodetectors with Au/Al_2O_3/Au/TiO_2/CuPc structures. A large photocurrent enhancement of Copper (II) Phthalocyanine (CuPc) was observed and supports our hypothesis of enhanced transport between nm-scale elctrodes.

Though the multilayer electrodes produce nm-gaps between metal contacts, the overall device is micron/submicron in length depending on the resolution of photo lithography used. In our case, ~10 linear microns of junction result in a device with ~10,000 conducting molecules. The ultimate scaling of nm-scale electrodes would be to add another perpendicular direction of nm-scale patterning over the face of the multilayer electrode. This can be achieved by a shadow lithography technique in which a nanowire is placed over the edge of the junction creating a ‘shadow’ under the nanowire. Junction areas outside of the shadow can be covered with insulator, making only a nm-scale region available for molecular contact. In this case a single molecule electrode can be made using conventional deposition/patterning techniques. Our group had demonstrated the concept with a shadow line deposition with a width of 6 nm under a CNT (101). However controlled growth of nanowires in a precise location is a challenge. ZnO nanowires (NWs) are a better choice than CNTs not use as a mask because ZnO NWs can cast a straight and uniform shadow. Chapter 6 will introduce the selective growth of ZnO NWs from the exposed edge of the Si/Al_2O_3/Si trilayer structure. The growth mechanisms on these nm-scale nucleation sites will also be discussed.

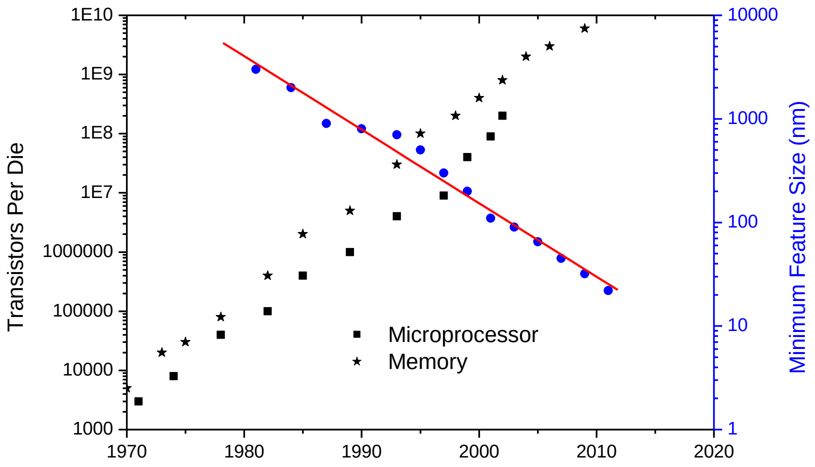

Figure 1.1. The development of the transistors per die and minimum feature size (●) over time (adapted from Intel official website http://www.intel.com/technology/mooreslaw/).

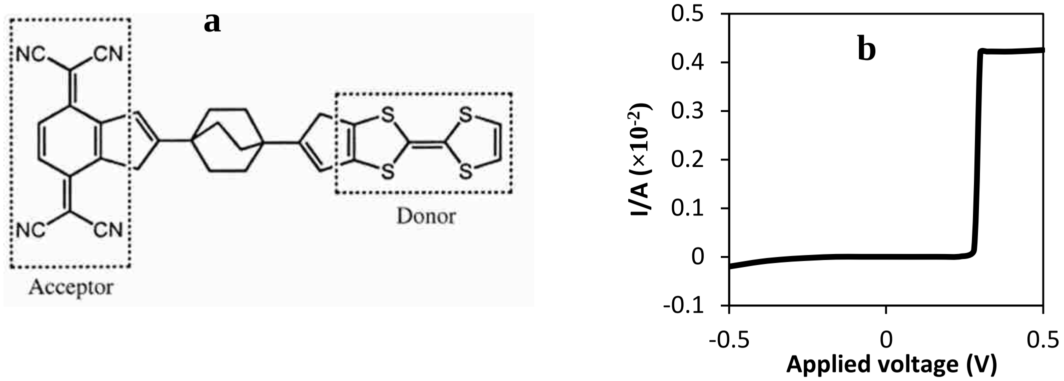

Figure 1.2 (a) An example of a rectifier molecule, (b) the calculated *I*/*V* curve of the molecule in (a). Adapted from ref.[7].

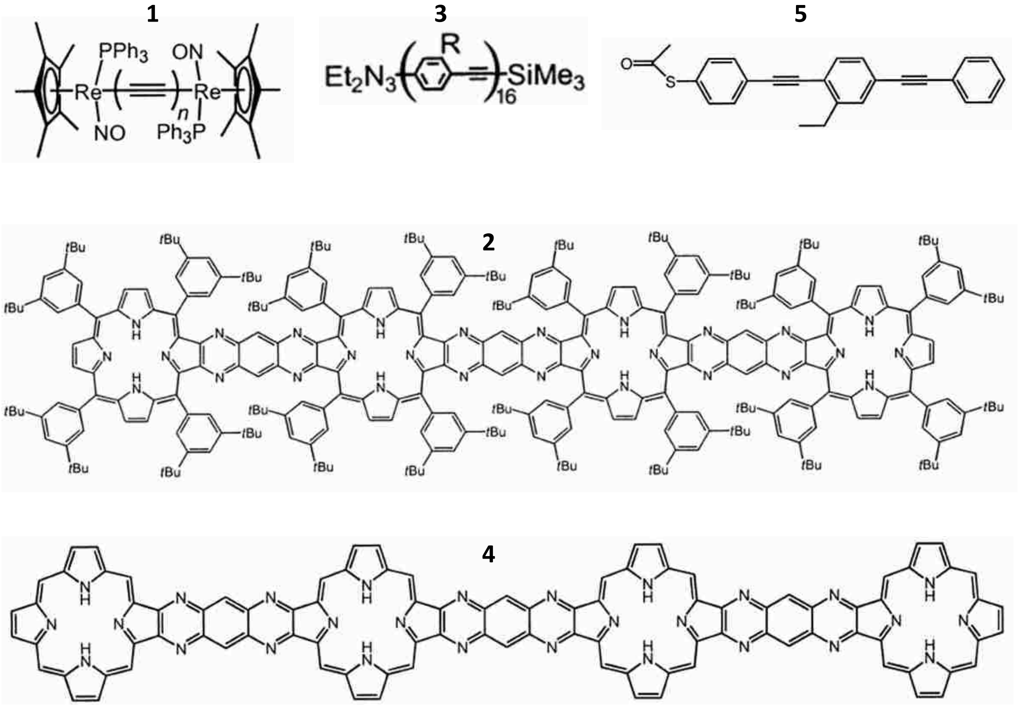

Figure 1.3. Chemical structures of metal terminated carbon chains with the Re(C≡C)Re unit (Molecule 1), oligomeric linear prophyrin arrays (Molecule 2 & 4), oligo(phenylene ethynylene)s (Molecule 3), and 4-(2’-methyl-4’(phenylethynyl)phenylethynyl)-1-phenylthiolate (Molecule 5) in the text.

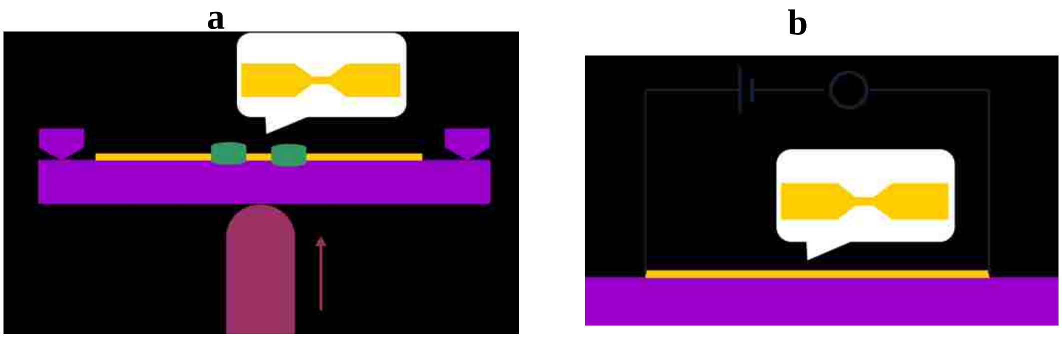

Figure 1.4. Fabrication techniques of single molecular junctions: (a) Mechanical break junction technique and (b) Electromigration break junction technique. Adapted from Ref. [51] and Ref. [53], respectively.

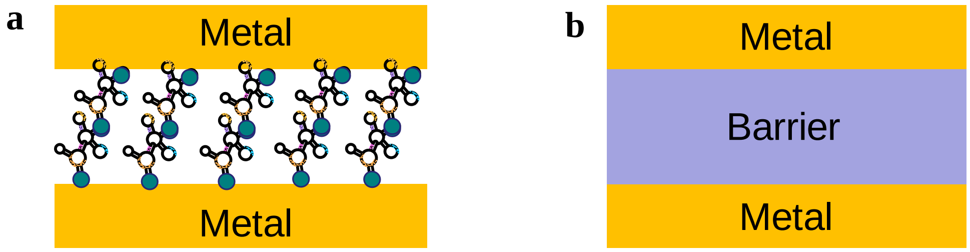

Figure 1.5. Schematic drawing of (a) a metal/molecules/metal structure and (b) a metal/barrier layer/metal tunnel junction.

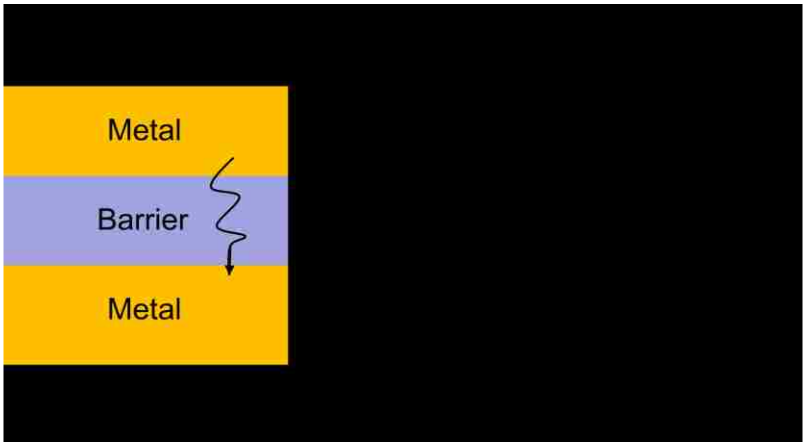

Figure 1.6. Electron with energy *E* incident on a potential barrier.

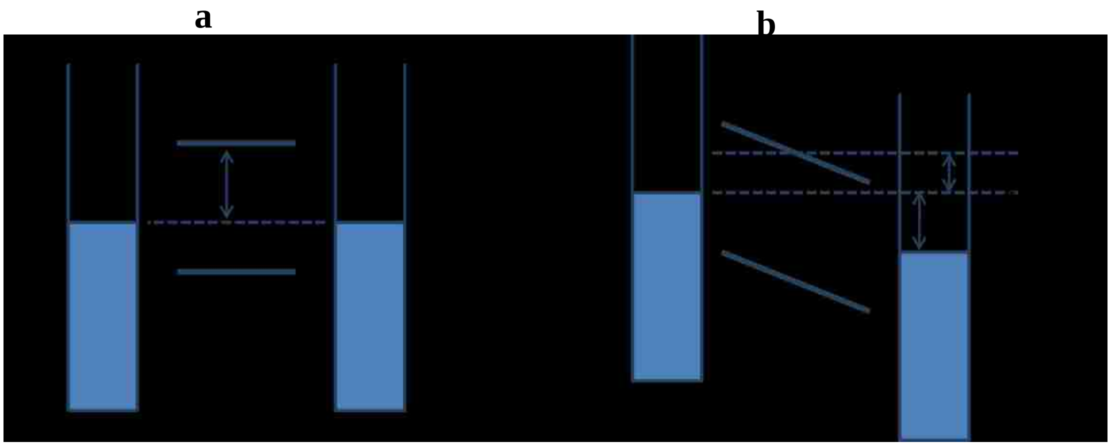

Figure 1.7. Schematic energy diagram of a metal/molecules/metal structure with (a) a zero bias and (b) a bias of *V*.

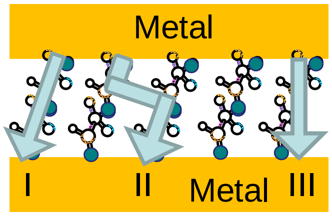

Figure 1.8. Schematic drawing of possible mechanisms for current tunneling across molecules.

Table 1.1. Properties associated with different capacitors.

	A (nm^2)	d (nm)	C (F)	ΔE (eV)
Nanocapacitor	5^2	2	1.1×10^{-19}	0.73
Microcapacitor	$10{,}000^2$	2	4.4×10^{-13}	1.8×10^{-7}

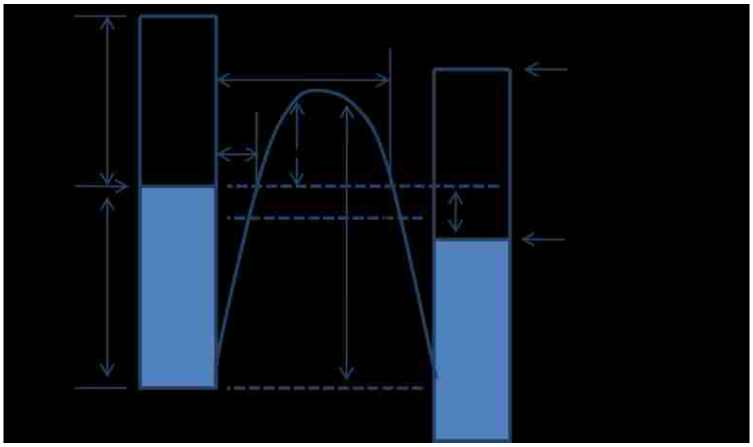

Figure 1.9. Schematic energy diagram of a general barrier in dielectric layer between two metal electrodes. Adapted from Ref.[66].

Figure 1.10. Coulomb blockade effect in a nano-scale capacitor.

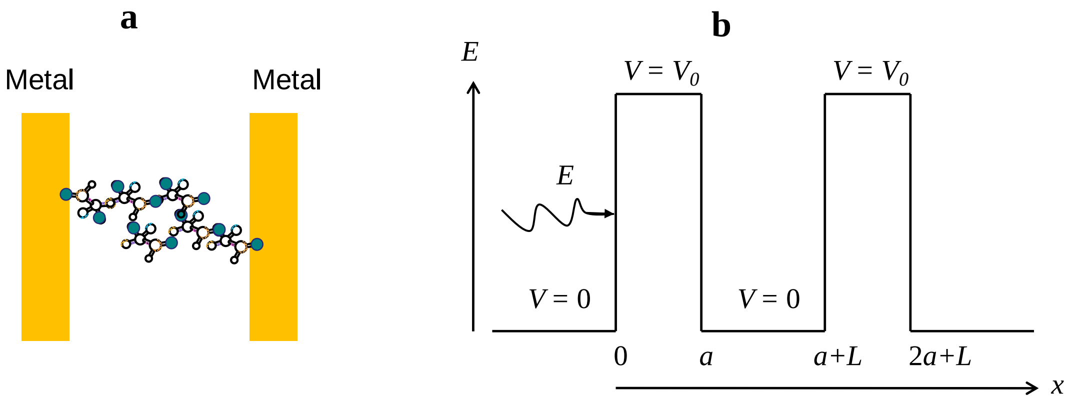

Figure 1.11. Schematic drawing of (a) a metal/single molecule/metal structure and (b) its simulated double barrier system.

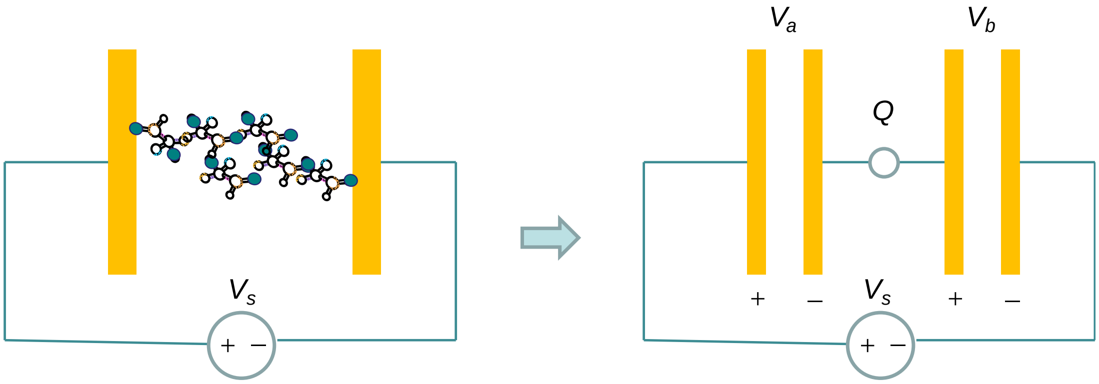

Figure 1.12. Equivalent circuit of metal/single molecule/metal structure connecting to a voltage source.

Figure 1.13. Coulomb blockade effect in a double junction system. $V_1 = e/(2C)$.

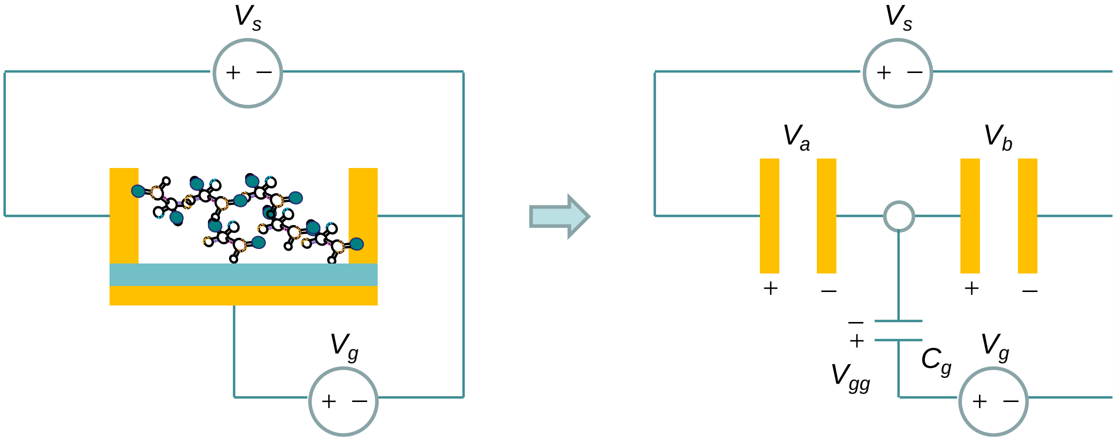

Figure 1.14. Equivalent circuit of a single molecular transistor.

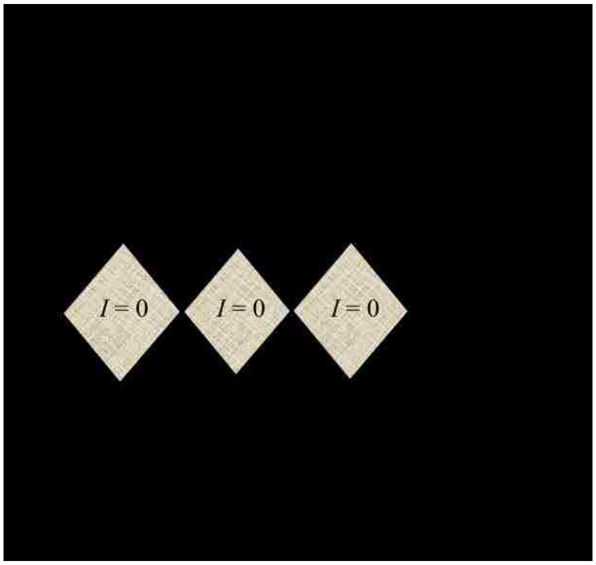

Figure 1.15. Coulomb diamond structures for a single molecular transistor. $V_1 = e / 2C_g$.

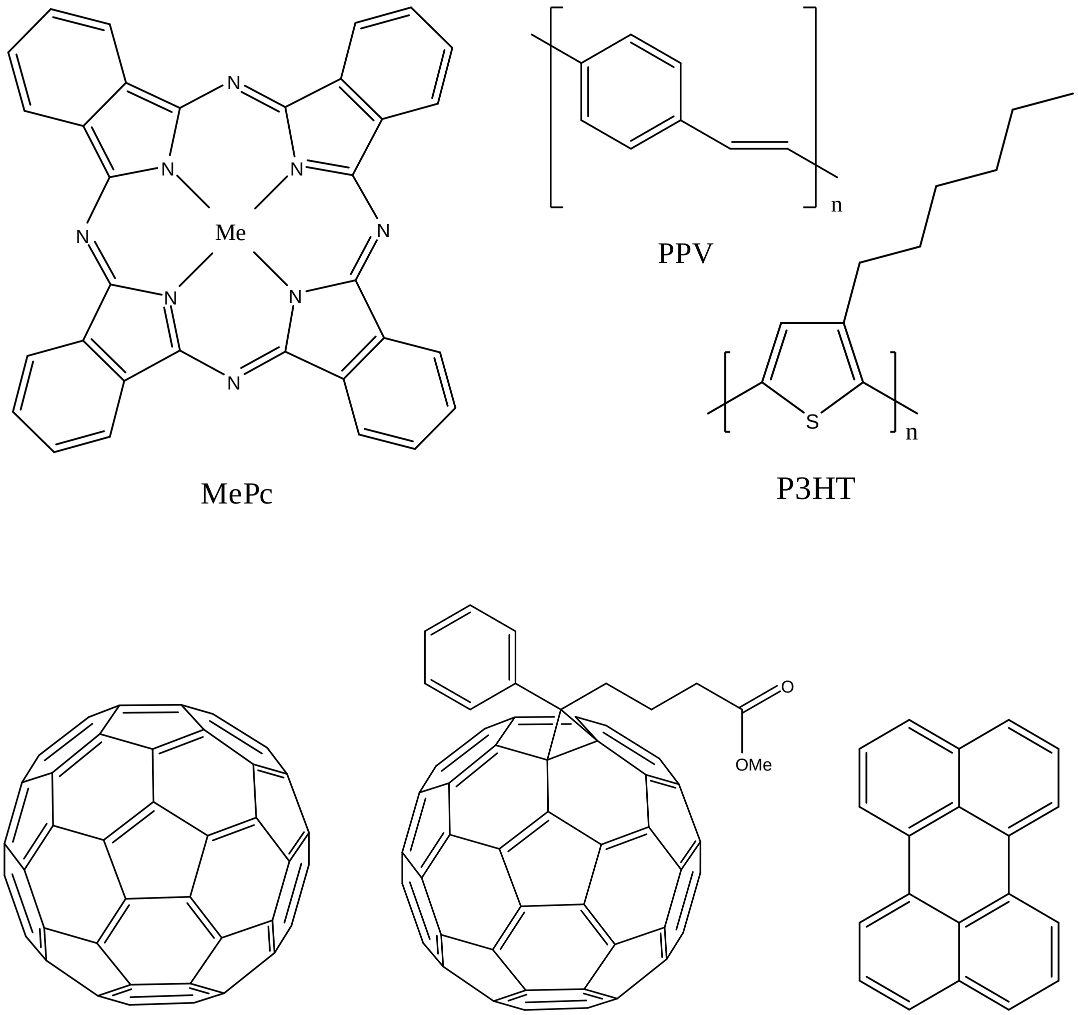

MePc

PPV

P3HT

C_{60}

PCBM

Perylene

Figure 1.16. Donor and acceptor materials used in organic solar cells.

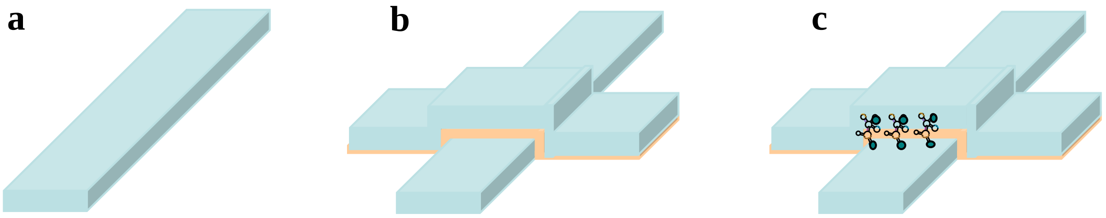

Figure 1.17. Schematic drawing of the fabrication steps: (a) deposition of a bottom electrode, (b) deposition of an alumina insulating layer and a top electrode, and (c) a molecular attachment at the exposed edge of a metal/dielectric/metal junction.

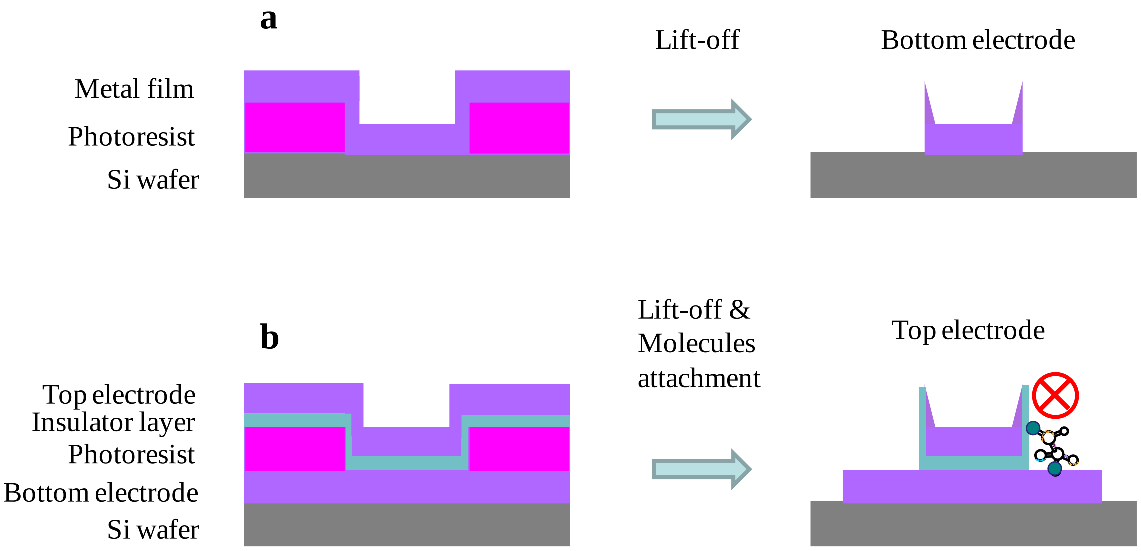

Figure 1.18. Schematic drawing of the formation of notches at the edge of (a) the bottom electrode by a lift-off process and (b) the top electrode and insulator length exceeding molecule length to prevent molecular bridging.

Chapter 2

Fabrication development of nano-gap electrodes at the exposed edge of Metal/Al_2O_3/Metal trilayer structures (Metal = NiFe & Ni)

2.1 Introduction

The photolithography and lift-off processes to fabricate molecular devices (100) will generate notch defects at the edge of thin films. These notches will be short tunnel junctions with top deposited electrode or block molecular attachment because the top layer can be far removed (>100nm) from the bottom. In order to eliminate these notches and obtain reliable metal/dielectric/metal tunnel junctions, a new photolithography technique, wet etching, and dry etching were tried. In this chapter, all technique developments will be introduced step by step following the fabrication flow: (1) a new pattern design for both top and bottom electrodes, (2) wet etching for bottom electrodes, (3) double-photoresist (PR) photolithography, (4) dry etching of the dielectric layer, (5) the sacrificial layer.

2.2 Fabrication development

2.2.1 Pattern design

Figure 2.1a shows the top view of the old pattern design for molecular devices. The horizontal lines are top electrodes and the vertical lines are bottom electrodes. The line width is 5 μm and the square pad area is 1mm × 1mm designed for probe contact. A large amount (36) of tunnel junctions can be fabricated on a piece of Si chip. However, the *I-V* properties of each tunnel junction are easily affected by the surrounding tunnel junctions if shorts or broken lines are present. To solve this problem, a new pattern of separated tunnel junctions was designed, as shown in Figure 2.1b. There are 16 separated tunnel junctions on a piece of Si chip. Figure 2.2b only shows one quarter of the total pattern. This new pattern was applied for device fabrication from Sample No.91.

2.2.2 Bottom electrodes by wet etching

2.2.2.1 Experimental details

Two samples were prepared using different methods in this work. Figure 2.2 shows the whole fabrication process for both samples. Sample A was prepared following procedures in Ref.(100), in which both electrodes were fabricated by photolithography, film deposition, and lift-off processes. First, a Si wafer with a 100 nm SiO_2 layer was ultrasonically cleaned with acetone, isopropanol (IPA), deionized (DI) water, and nitrogen drying. A normal one layer photolithography method was applied to pattern the bottom electrode using Shipley 1813 positive photoresist at a Karl Suss mask aligner. An AJA International Sputtering system was used to deposit Co and NiFe films, respectively. The deposition condition is at 1 mTorr with a gun RF power of 150 W. Then, a lift-off step was executed to define the bottom electrode pattern *via* Shipley 1165 resist remover for 3

h. The top electrode (NiFe) was fabricated across the bottom electrode using a same process mentioned above. Before the top electrode deposition, an Al_2O_3 dielectric layer with a thickness of 2 nm was deposited. This Al_2O_3 dielectric layer was fabricated using a specific process. An Aluminum layer of 1 nm was first sputtered on the bottom electrode at 2 mTorr with a gun DC power of 75 W. A gas mixture of Ar and O_2 (1:1) was flowed into the chamber and ignited at 60 mTorr with a 20 W bias power for 30 s to oxidize the Al layer. Then, a second Aluminum layer of 0.5 nm was sputtered and oxidized to form a final alumina layer of 2 nm. After getting tunnel junctions with a structure of Co 5 nm/NiFe 10 nm/Al_2O_3 2 nm/NiFe 10 nm, the sample was put in a quartz tube. The tube was purged by an Ar flow for 30 min first and heated with a rate of 10 K/min. After the sample was annealed in the Ar flow at 453 K for 60 min, the tube was cooled down with a rate of 10 K/min.

Wet chemical etching was used to replace the lift-off to prepare the bottom electrode in sample B. The Co and NiFe film was first sputtered on the SiO_2 wafer, sequentially. Photoresist was patterned on the NiFe film and the sample was immersed in a 0.2 M HCl solution for 5 min to etch the Co/NiFe film. The bottom electrode formed after removing the remaining photoresist. The patterning of the dielectric layer and top electrode is same as that of sample A.

The *I-V* properties were characterized by an MM Micromanipulator probe station. AFM images and measurements were gathered with a PicoPlus AFM system (Molecular Imaging, Agilent Technologies).

2.2.2.2 Results and discussion

Sample A and B both show good performance as tunnel junctions after annealing (see Figure 2.3). A reduction of defects in the Al_2O_3 layer by the annealing process improves the insulating property of tunnel junctions. There are 16 isolated tunnel junctions in each sample. The current of tunnel junctions of sample A is $(10.0 \pm 1.0) \times 10^{-7}$ A at 0.1 V and that of sample B is $(5.0 \pm 1.0) \times 10^{-7}$ A at the same applied bias. 10 tunnel junctions were measured for each sample. This result shows that the etching process to form the bottom electrode, without jagged tears from liftoff process, results in improved junction quality.

Simmons model and Brinkman model (102) were used to fit the effective barrier thickness and barrier height of the alumina insulating layer. It is very clear from Figure 2.4 that sample B has a smaller deviation of the barrier thickness and barrier height than sample A. The barrier thickness of sample B is about 19 Å, which is consistent with the physical thickness of the alumina layer measured by AFM (~ 20 Å).

The yield of sample B (etched) is 98% for 400 tunnel junctions, that is much higher than the 15% yield of sample A. This high yield of sample B confirms that this wet etching process to pattern the bottom electrodes is an improved method for molecular device fabrication. The break down voltage of tunnel junctions of sample B is 2.7~3.2 V, higher than 1.5~2.0 V of sample A, as shown in Figure 2.5.

AFM is a very good tool to study the morphology of the bottom electrodes for both liftoff and wet etched samples. The 3D AFM images in Figure 2.6 show many notches ~50 nm tall formed at the edge of the bottom electrode in sample A that can electrically short with the top electrode deposited later. There are no notches observed at the edge of the bottom electrode in sample B. These notches in Figure 2.6a leads to a high probability to short tunnel junctions. This is the reason why sample A has a low yield below 15% and a small break down voltage of 1.5~1.8V.

The wet chemical etching process does not produce notches and improves the electrical performance of Co 5 nm/NiFe 10 nm/Al_2O_3 2 nm/NiFe 10 nm tunnel junctions greatly. The high yield of ~ 98% (400 tunnel junctions) and the low cost of this technique indicate this wet etching method as an excellent way to fabricate molecular devices.

2.2.3 Patterning top electrodes by a double-PR photolithography

In order to obtain a uniform edge profile of top electrodes and prevent the situation depicted in Figure 1.18b, several fabrication routes were explored based on equipment available in the Center for Nanoscale Science and Engineering (CeNSE).

Wet etching was tried first to fabricate top electrodes. The insulating layer thickness of 2 nm was found too small to prevent the acid from etching bottom electrodes. Therefore, most of bottom electrodes were observed to be etched after device fabrication.

In the semiconductor industry, reactive ion etching (RIE) is commonly used to pattern thin films. Chlorine-based plasmas (103) are used to etch metal films. Unfortunately, the RIE system (Plasmalab 80) in CeNSE is designed to etch Si & SiO_2 and the chlorine gas is not allowed to use. Thus physical ion ablation with the Ar milling process was executed to etch the Ni film following a PR mask. Results show that the etching efficiency of Ni compared to PR by Ar milling was too small. The PR mask was totally removed before the Ni film was etched. Another problem is the polymer residue of PR after Ar milling. Various PR removers and the O_2 plasma ashing process were tried to remove the polymer residue. All of these procedures did not work well.

Therefore, the only available method is the photolithography + lift-off method. As mentioned above, notches form at the edge of thin film by a common photolithography + lift-off route. Here, a double-PR-layer photolithography is introduced to obtain good metal patterns as depicted in figure 2.7. The overhanging top PR layer prevents side wall deposition during metal evaporation, and hence a ‘clean liftoff’ when PR is removed by stripper. A Si wafer with a 100 nm SiO_2 layer is ultrasonically cleaned by acetone, isopropanol (IPA), deionized (DI) water, and nitrogen drying. A layer of PMGI (MicroChem) polymer was first spin coated on the Si wafer and baked at 170°C for 5 min. A layer of S1813 (MicroChem) was spin coated on the PMGI layer and baked at 115°C for 1min. Then, the Si wafer was exposed in a UV light for 10s at a Karl Suss mask aligner. The double layer PR was developed in a MF-319 (Microposit) solution for 5~10 min. A good undercut structure of the PMGI/S1813 double layer formed, leading to a Ni top line without any edge notches, as shown in Figure 2.7a. Figure 2.7b is the top view of the undercut structure. The open line width of S1813 is 5μm and that of PMGI is ~ 9 μm. Figure 2.7c is the top view of a single developed S1813 layer using the same photomask in Figure 2.7b. The horizontal lines in Figure 2.7b&c are the bottom Au & NiFe electrodes, respectively.

2.2.4 Dry etching of the dielectric layer

The alumina insulating layer and the top electrode layer were deposited together by a single-layer-photolithography in the previous work (100) . To meet the vertical sidewall of the insulating layer and top electrode in Figure 1.17b, Ar milling was used to open the alumina insulating layer after patterning the top electrode.

2.2.5 The sacrificial layer

It was found that the Al_2O_3 insulating layer was etched during the photolithography process for patterning top electrodes. The PR developer (MF-319, Microposit) is a basic solution and would like to react with the Al_2O_3 layer. To solve this problem, a sacrificial Ni layer was deposited on the Al_2O_3 layer to inhibit the etching issue.

2.3 Final fabrication flow

Figure 2.8 shows the whole fabrication process for the nano-gap electrodes at the exposed edge of metal/Al_2O_3/metal trilayer structures (metal = NiFe & Ni). The bottom electrodes were prepared by photolithography and wet etching. This part has been introduced in Section 2.3 in detail. After patterning the bottom electrode, an Al_2O_3 layer of a 2 nm thickness was deposited by Al sputtering and O_2 plasma oxidation. Then, a sacrificial metal layer of a 2 nm thickness was sputtered on the Al_2O_3 layer in the same AJA International Sputtering system to protect the Al_2O_3 layer from the PR developer etchant. After a good undercut profile formed, a metal layer of a 20 nm thickness was e-beam evaporated to pattern the top electrode at a Torr International EB4P series system. A second lift-off process was executed to remove PR. The top electrode left has a vertical sidewall profile and works as an etch mask for the following Ar milling. The structure of the exposed edge of metal/Al_2O_3/metal multilayer structure was obtained after the Ar milling process at Plasmalab 80 stopped on the metal bottom electrode. The gap between the top and bottom electrodes is precisely controlled by the thickness of the Al_2O_3 layer. The gap scale can reach 2 nm. Therefore, molecules larger than 2 nm can bridge these two electrodes to form a molecular device.

Sample No.141 & 146 were prepared using this new fabrication flow and act as representative samples. The sacrificial Ni layer is 10 Å for both samples. The only difference between these two samples is the thickness of the Al_2O_3 insulating layer. Sample No.80 was prepared using the old method (100) for a comparison. All *I-V* measurements were performed at room temperature by a Keithley 2430 1KW Pulse Sourcemeter, a Keithley 6430 Sub-femtoamp Remote Sourcemeter, and an MM Micromanipulator probe station.

2.4 Electrical properties

The tunneling current densities (TCD) of the nanogap electrodes at the exposed edge of NiFe/Al_2O_3/Ni tunnel junctions are shown in Table 2.1. The thickness of the Al_2O_3 layer and the Ni layer was measured by AFM. Sample No.141 has a TCD of ~ 0.0015 A/cm^2. Sample No.146 has a TCD of ~ 15 A/cm^2. They are both far smaller than the TCD of ~ 300 A/cm^2 of Sample No.80 fabricated by the lift off process (100) process.

Figure 2.9a shows the current density-voltage characteristics of Sample No.141 and Sample No.146. Both charts show a typical tunneling character. The current density-voltage curve of sample No.141 was fitted by Simmons model. A barrier height of 1.0 eV and a barrier thickness of 28.4 Å were obtained. The simulated Al_2O_3 layer thickness is larger than the AFM measurements of 20 Å. One possible explanation is the sacrificial Ni layer partially or fully oxidized. Ni has a large work function (5.01eV) approaching that of Au (5.1 eV)and XPS studies have shown that an oxide free surface can exist (104). However, under the handling conditions required for chemical modification, it is possible that an oxide surface layer forms making direct molecular attachment to metal electrode difficult. To test this hypothesis, a reference sample of a 10 nm Ni film was exposed in the air for 10 min. Then it was scanned at a Spectroscopic Ellipsometers (M-2000V, J.A.Woollam Co. Inc.) and a thin NiO layer of a 7 Å thickness was detected. Therefore, the total oxide layer thickness should be 20 Å + 7 Å = 27 Å. This is consistent with the simulated barrier thickness of 28.4 Å by Simmons model. Another control experiment was done by changing the Al_2O_3 thickness from 20 Å (sample No. 141) to 10 Å (sample No.146). The total oxide layer thickness should be 17 Å. And this is also consistent with the simulated barrier thickness of 18.1 Å derived from Figure 2.9b. These results confirm the sacrificial Ni layer partially oxidized. The dielectric thickness of 17~18 Å in Sample No.146 is smaller than that of 20 Å in Sample No.80. However, the tunneling current density of 15 A/cm^2 in Sample No.146 is 20 times smaller than that of 300 A/cm^2 in Sample No.80 (lift off process). These comparisons shows tunnel junctions fabricated by the etching process to define top and bottome electrode lines have much better insulating properties than those fabricated by the process of liftoff with torn edges.

2.5 Molecular attachment

A ~ 30Å long organometallic cluster (OMC) with thioacetate terminated tethers was first synthesized (105) by D.F. Li *et al.* to bridge the nanogap electrodes. The chemical formula of the OMC is $[(pzTp)Fe^{III}(CN)_3]_4[Ni^{II}(L)]_4[O_3SCF_3]_4$ [(pzTp) = tetra(pyrazol-1-yl)borate; L = 1-S(acetyl)tris(pyrazolyl)decane] (Molecule I). Figure 2.10 shows its X-ray structure. This molecule essentially comprises a cube of 12 edges of cyanide bridged Ni and Fe atoms (-Ni-N≡C-Fe-). There are four 10 carbon alkane tethers connecting 4 Ni atoms at the alternating corners of the molecular cube (105). The thioacetate group is a protecting group to preclude thiol reactions during the formation of an octametalic core. This thiolacetate group is readily removed during an electrochemical molecule attachment (106) process on the device to form thiol-metal (metal = Ni or NiFe) surface bonds.

Another similar OMC (Molecule II) was also synthesized for molecular attachment. The only difference between Molecule I and Molecule II is the L part in the chemical formula. The acetyl group is replaced by the hydrogen atom (thiol) in Molecule II for easy attachment on the metal surface without electrochemical activation.

To attach Molecule I with thioacetate ligand to the Ni electrodes, a 2mM solution of OMC in a dichloromethane (CH_2Cl_2) solvent was subjected to an alternating ±100mV biasing between two metal electrodes. The time interval was 0.02s and lasted for 2 min. After the molecular attachment process completed, the sample was sequentially cleaned with IPA, DI water, and nitrogen drying. To attach Molecule II to metal electrodes, the nano-gap electrode was immersed in a same 2mM solution of OMC in a CH_2Cl_2 solvent for 2 min. Then the sample was sequentially cleaned with IPA, DI water, and nitrogen drying. Electrical properties of tunnel junctions before and after molecule attachment were performed by the Keithley 2430 1KW Pulse Sourcemeter, the Keithley 6430 Sub-femtoamp Remote Sourcemeter, and the MM Micromanipulator probe station.

Unfortunately *I-V* studies show no difference before and after molecule attachment. This indicates the current is not passing through molecules. Over 1,000 working tunnel junctions with NiFe/Ni electrodes had been tested before and after Molecule I/II attachment. Figure 2.11 shows the current-voltage characteristics of a representative sample (No.146) before and after molecular attachment. There is no current increase due to molecular attachment, considering the *I*-V measurement variation. 150 junctions done with conditions the same as No.146 did not show molecular current increases. The electrode gap of ~ 17 Å in Sample No.146 is smaller than the OMC length allowing molecules to bridge the top and bottom electrodes but no molecular current was detected.

Since a nickel oxide layer of 7~8 Å has been measured by the ellipsometer measurement and by Simmons tunnel current simulation in Section 2.4, it is likely that oxide layers on the surface of both Ni electrodes blocks the bonding between the thiol group of molecule and metal atom. In the prior report from this group (100), dichloromethane was used as a solvent for the electrochemical addition of the thioacetate functionalized molecule. Exposure to air produces HCl in the dichloromethane and it was postulated that this acid helped etch NiO to give a clean surface. However over etching would result in shorts between electrode layers or complete etching of metal lines. The dichloromethane would evaporate during the functionalization process thereby concentrating acid. This would make etching conditions extremely difficult to reproduce. After over 3000 tunnel junctions were made and tested, working directly and independently of Tyagi, I found no conclusive molecular current was seen that could not be explained as an electrode short.

Therefore, a noble metal should be used to replace Ni/NiFe as the electrode material to test the nanogap electrode structure and study molecular current through the metal complex. Much of the molecular electronics literature to date has utilized Au-thiol chemistry to ensure clean inert surfaces for controlled molecular contacts. Therefore, fabrication of gold tunnel junctions is required. It needs to be pointed out that because insulators do not form stable films on Au, this requires an innovative fabrication approach that will be introduced in the following chapter.

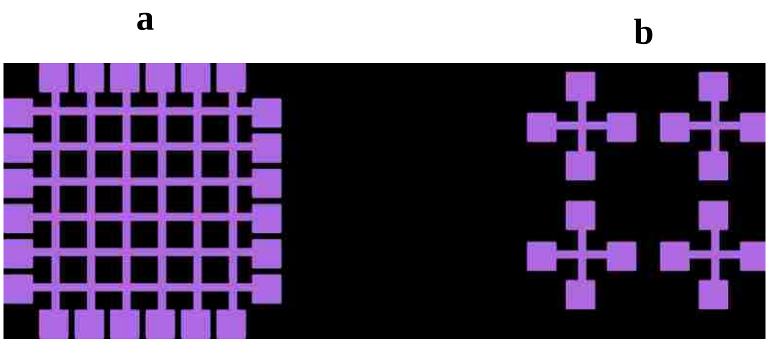

Figure 2.1. Schematic drawing of the top view of the (a) old and (b) new pattern design for both electrodes. The sizes of the square pads and lines in (a) & (b) are 1mm×1mm, 2µm×2mm, and 5µm×1.5mm, respectively.

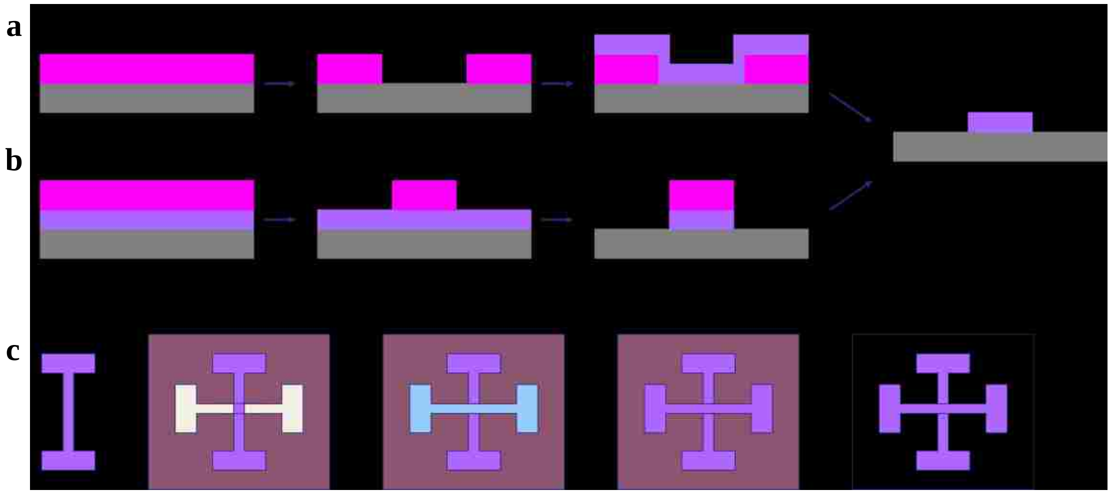

Figure 2.2. Schematic drawing of the fabrication process of (a) the bottom electrode by a lift-off process, (b) the bottom electrode by a wet etching process, and (c) the top electrode by a lift-off process. The bottom electrodes of Sample A and B was fabricated following (a) and (b) route, respectively. The top electrode of both samples was fabricated following route (c).

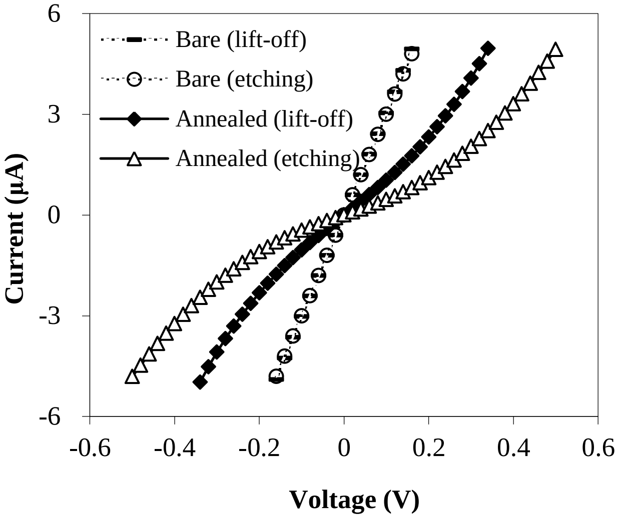

Figure 2.3. Current versus voltage behavior of the Co/NiFe/Al_2O_3/NiFe electrode fabricated by the lift-off (sample A) and wet chemical etching (sample B) before and after annealing.

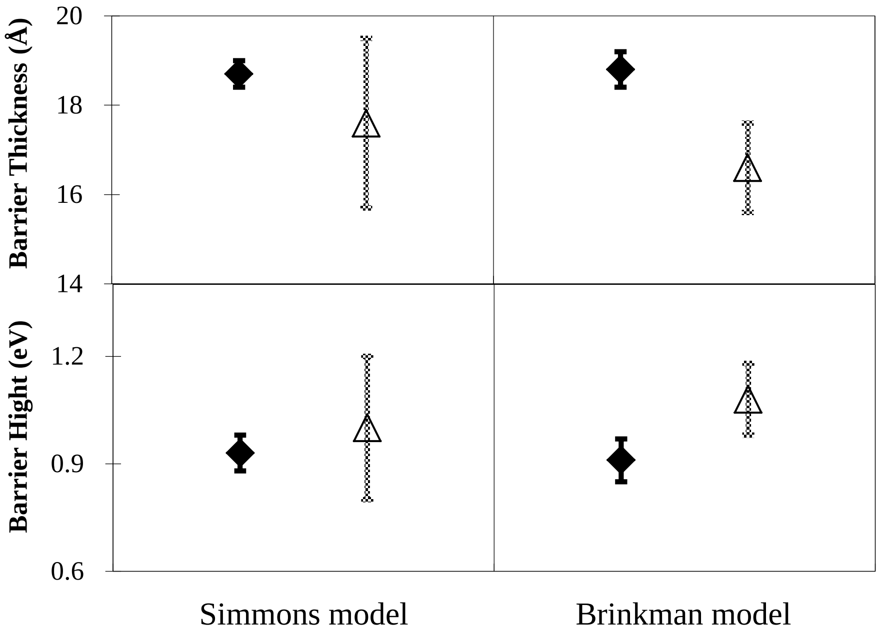

Figure 2.4. Barrier thickness and barrier height of tunnel junctions fabricated by the lift-off (Δ, sample A) and the chemical wet etching (♦, sample B) with Simmons & Brinkman models (10 tunnel junctions measured for each sample).

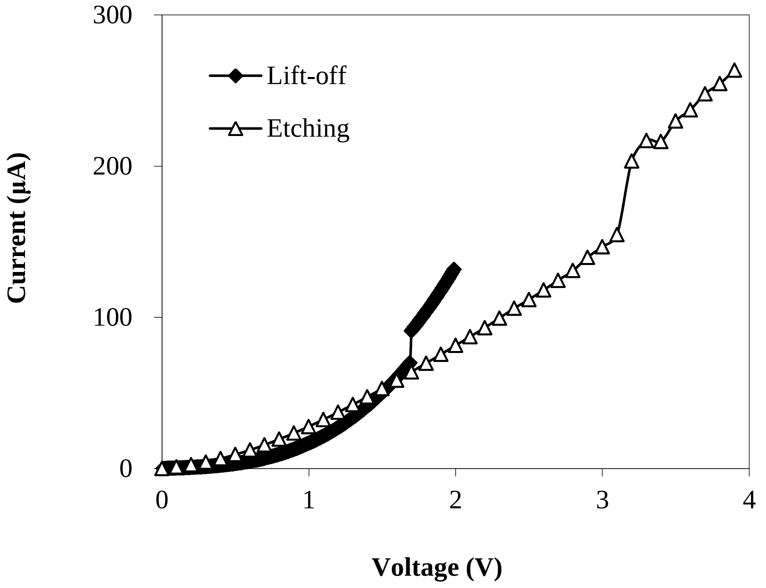

Figure 2.5. Break down voltage of tunnel junctions fabricated by a lift-off process (sample A) and a chemical wet etching process (sample B).

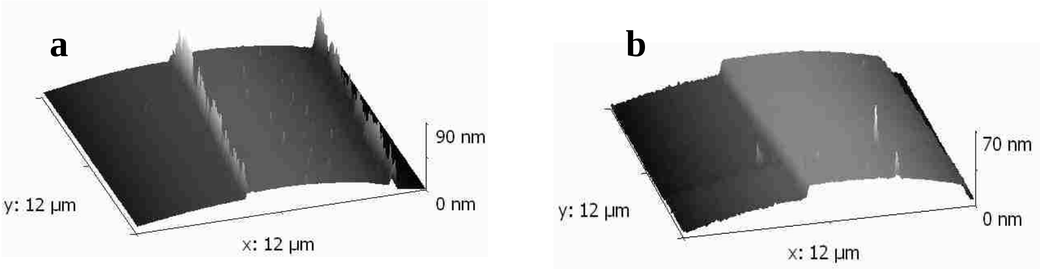

Figure 2.6. 3D AFM images of the bottom electrode in (a) sample A by a lift-off process and (b) sample B by a wet chemical etching process.

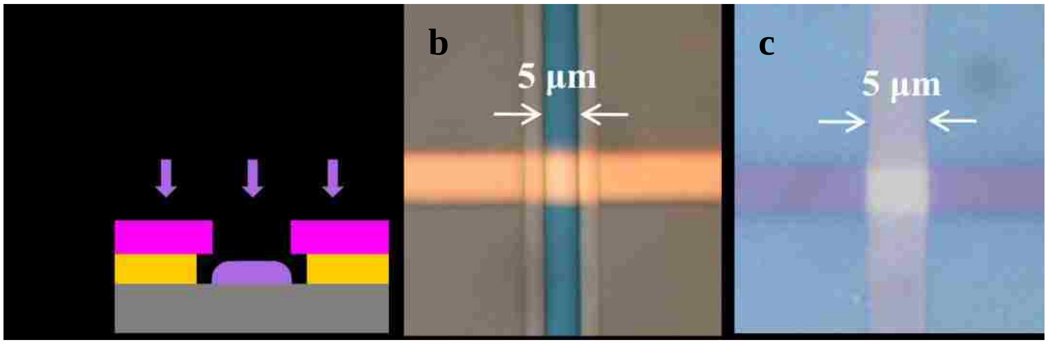

Figure 2.7. (a) Schematic drawing of the Ni top electrode by an S1813/PMGI undercut profile. Microscope top view images of (b) an S1813/PMGI-double-layer undercut profile and (c) an S1813-single-layer profile.

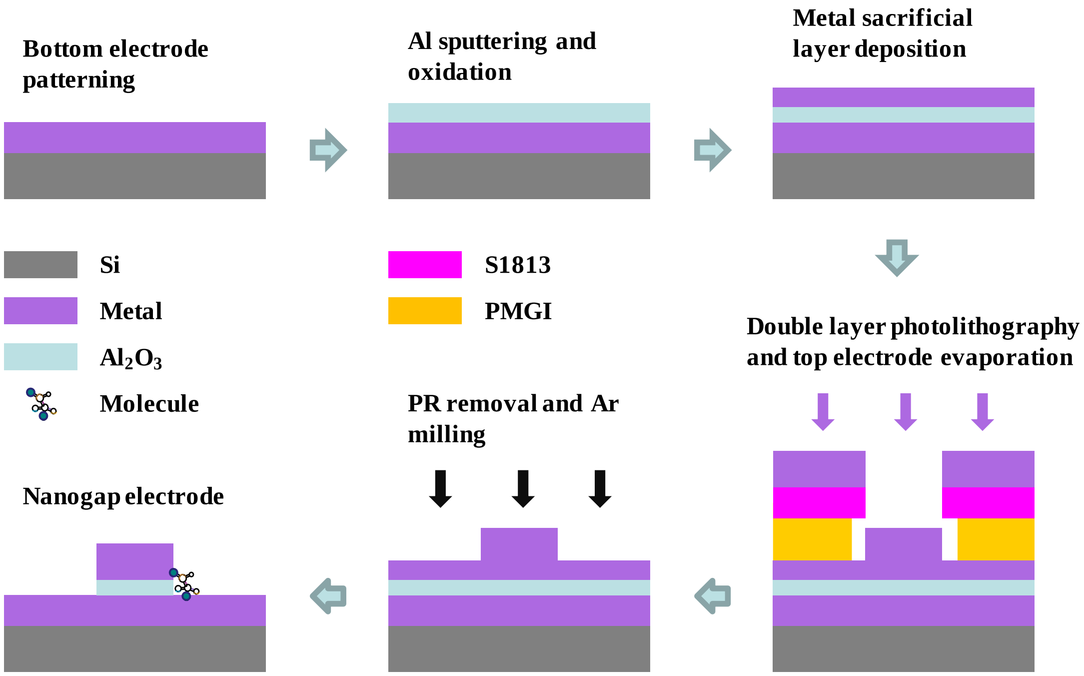

Figure 2.8. Schematic drawing of the nanogap electrode fabrication at the exposed edge of metal/Al_2O_3/metal trilayer structures (metal = NiFe & Ni).

Table 2.1. The barrier thickness and tunneling current density comparison of Metal/Al_2O_3/Metal structures by different fabrication routes (Metal = NiFe & Ni).

Sample	Structure	Tunneling current density (A/cm^2)	Fabrication route
No.80	NiFe/Al_2O_3 20 Å/Ni	~ 300	Ref.[100]
No.141	NiFe/Al_2O_3 20 Å/Ni 10 Å/Ni	~ 0.0015	This work
No.146	NiFe/Al_2O_3 10 Å/Ni 10 Å/Ni	~ 15	This work

Note: The tunneling current densities of all samples were measured at 0.5 V.

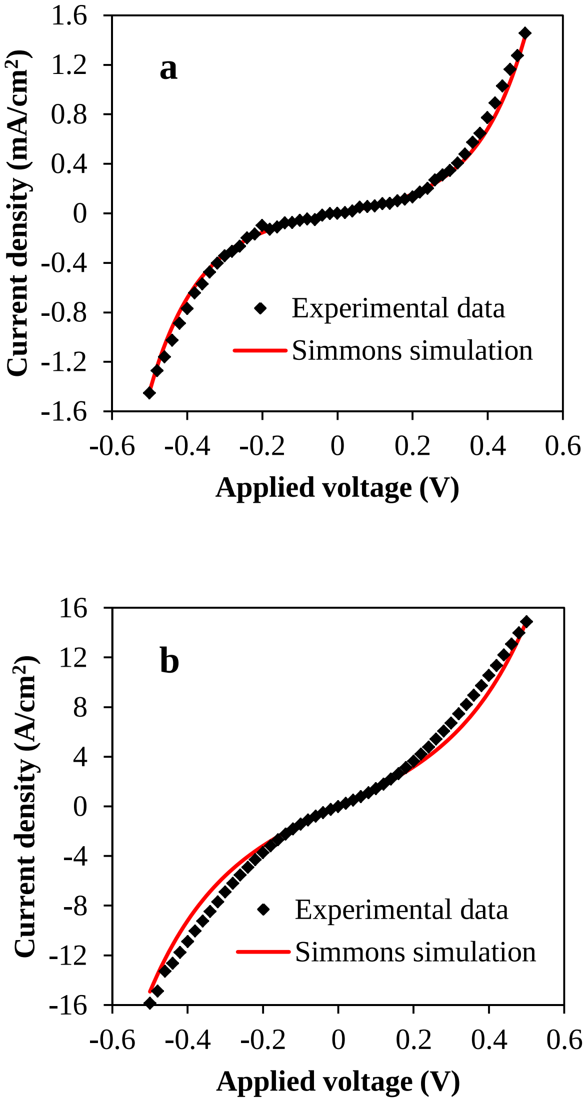

Figure 2.9 Current density-Voltage characteristics of NiFe/Al_2O_3/Ni tunnel junctions with exposed side edges (■) and Simmons simulation (—). The thickness of Al_2O_3 is 20 Å (a) and 10 Å (b). The barrier thickness of the simulation curves of (a) and (b) are 28.4 Å and 18.1 Å, respectively. A barrier height of 1.0 eV is used for both simulations.

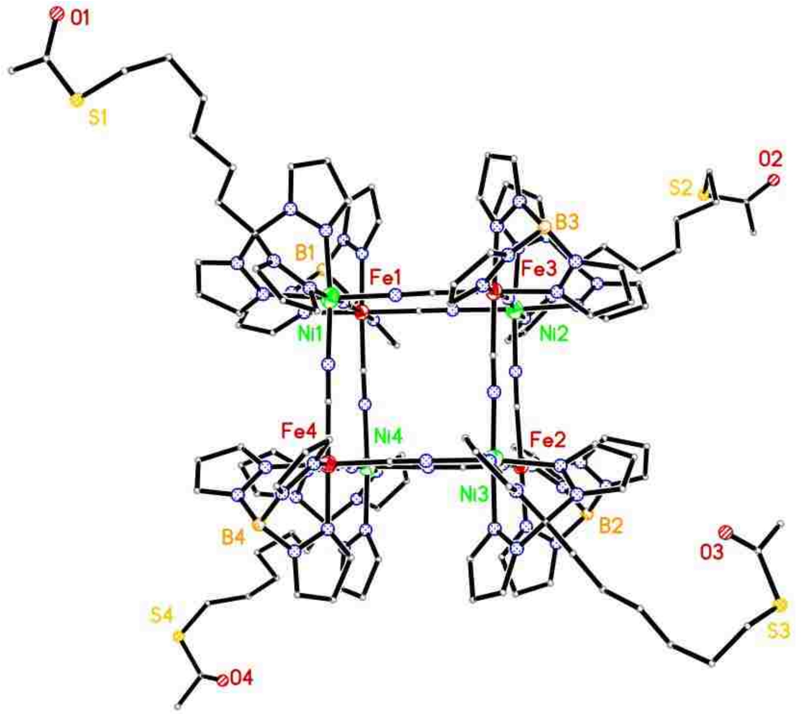

Figure 2.10. X-ray structure of the organometallic cluster [(pzTp)Fe^{III} (CN)$_3$]$_4$ [Ni^{II}(L)]$_4$[O$_3$SCF$_3$]$_4$ [(pzTp) = tetra(pyrazol-1-yl)borate; L = 1-S(acetyl)tris(pyrazolyl)decane]. All anions, hydrogen atoms, pendant pyrazoles, and disordered S(acetyl)hexyl- chains are removed for clarity [105] .

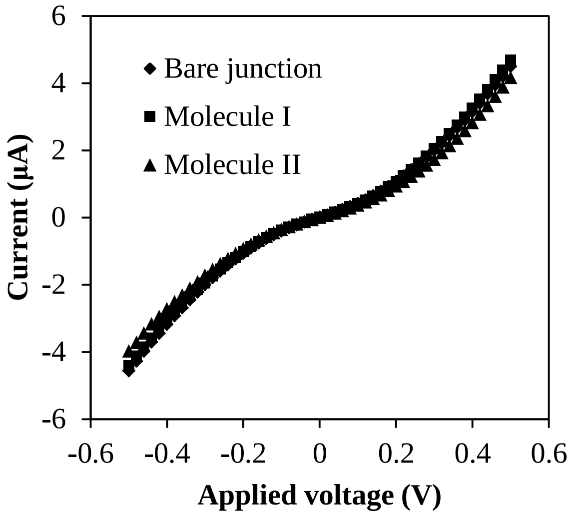

Figure 2.11. Current-Voltage characteristics of bare NiFe/Al_2O_3/Ni tunnel junctions before and after Molecule I & II attachment.

Chapter 3

Nano-gap electrodes formed at the exposed edge of Au/SAM/Al_2O_3/Au tunnel structures grown by atomic layer deposition

3.1 Introduction

Fabrication of nanometer-scale electrode gaps is a critical step for numerous devices based on molecular conduction and to probe the fundamental transport properties of molecular materials such as organic conductors. Many techniques have been developed to generate nano-gaps between electrodes in which molecules are bridging. They can be divided into the line-gap (51-54, 58-60, 107), cantilever-tip-gap (9, 43, 50, 108, 109) and plane-gap techniques (40, 41, 45, 47, 65, 100, 110, 111). Nano-gaps fabricated by the line-gap technique are formed in the middle of a metal line, which is composed of pure Au only. Several techniques such as mechanical break junction (51, 52), electromigration junction (53, 54, 58, 107), tip-end junction (59) and shadow lithography junction (60) have been well developed to realize nano-gap electrodes for studying molecules, even for single molecules but suffer from scaling and yield issues. Scanning probe microscopy (SPM) is a tool used normally to measure the morphology of the self-assembled monolayer (SAM) of molecules on the metal surface (30, 43, 50, 108, 109) and produce a nm-scale cantilever-tip-gap. This technique simplifies the fabrication process and eliminates the problem of shorting however the single probe limits its application in devices.

The plane-gap techniques use a metal/insulator/metal structure to create nano-scale gaps relying on the thickness of the insulator to set the critical electrode gap between metal electrodes. Several techniques including Langmuir-Blodgett (LB) film (40, 41), nanopore (47), crossing metal wires (65), and hanging Hg drop electrode (45) have been developed to attach molecules between plane electrodes while those devices typically suffer from electrode shorting problems. Recently, several groups concurrently developed a simple technique to fabricate the exposed edge of metal/oxide/metal structure for molecular electrodes (100, 110, 111). This technique uses highly controllable film thickness (i.e. Al_2O_3) to set the critical spacing between electrodes. After lift-off or etching process, molecule clusters can bridge across the nm-thick insulator connecting top and bottom metal contacts (100). The critical challenge of this device design is to have a high quality insulator film since background tunnel current can dominate device current instead of the conduction through molecules bridging between electrodes at the edge. The system, with NiFe or Ta metal contacts, also possessed long term stability issues due to surface oxidation and hillock formation from stress release (112, 113) and eventual surface oxidation of metal surface. Much of the molecular electronics literature to date has utilized Au-thiol chemistry to ensure clean inert surfaces for molecular contacts. However it is difficult to form stable Au-oxide tunnel junctions due to a high surface energy mismatch, subsequent island growth of oxide and the formation of shorts. It has previously been observed that SAMs can aid in uniform Au deposition on SiO_2 substrate that usually require a reactive metal wetting layer (i.e. Ti) (114). Although Au-oxide tunnel junction can be fabricated when the oxide layer is thick enough to coalesce from islands to a continuous film, it is extremely difficult to fabricate high quality Au tunnel junctions when the thickness of the oxide insulating layer is below 5 nm. Until now, Au tunnel junctions with an oxide insulating layer have rarely been reported. J.S. Moodera *et al.* (115) cryogenically deposited Al_2O_3 between Au layers and the *dI/dV vs* voltage curve demonstrates typical tunneling characters but Al_2O_3 thickness was not mentioned. G.J. Ashwell *et al.* (111) realized Si_3N_4 deposition on Au with a SiO_2 mushroom-shaped dome to form Au/ Si_3N_4/SiO_2/Au structure with a nano-gap over 3.5 nm which can only be applied to study very large molecules.

In this work, we employed atomic layer deposition (ALD) to grow Al_2O_3 layer on Au electrodes that were modified with a SAM of alcohol groups. The alcohol provides a hydrogen source for the monolayer reaction with trimethyl aluminum thereby giving uniform coverage. Ar milling was then used to expose the edge of the Au/insulator/Au structure which has a much lower leakage current density than those Au tunnel junctions previously reported. The gap between two Au electrodes below 2 nm was realized and is thus suitable for the study of small molecule conduction.

3.2 Experimental details

The structure of the nanogap on the exposed edge of Al/Au/SAM/Al_2O_3/Au multilayer is schematically shown in Fig.3.1a. The whole fabrication flow was schematically drawn in Fig.3.2. The device fabrication started with a 1000 Å thick SiO_2 layer grown thermally on Si substrate sequentially cleaned with acetone, deionized (DI) water and nitrogen drying. The bottom electrode was lithographically patterned (Karl Suss MJB3, S1813/PMGI-SF11 resist) into microwires connecting to large area pads (~ 1 × 1 mm^2) for electrical probing in a microprobe station. Onto this 50 Å of Al and 500 Å of Au were sputter coated (AJA systems) and the bottom electrode pattern realized by liftoff. Then the bottom electrode was dipped into 10 mM β-mercaptoethanol ($HSCH_2CH_2OH$, Sigma-Aldrich, ≥ 99%) solution for 30 min to form a self-assembled monolayer on Au surface to provide –OH groups for the following atomic layer deposition of Al_2O_3 (Cambridge Nanotech Savannah 100 system). 14, 18 and 23 deposition cycles (H_2O/trimethyl aluminum) were applied for sample No.333, No.328 & No.374, respectively. In order to protect Al_2O_3 material from being etched by the alkaline photoresist developer, 200 Å of Au was sputtered on the Al_2O_3 ALD layer. The top Au electrode (~800 Å) was formed by thermal deposition into lithographically patterned top electrodes followed by liftoff and works as the top etch mask for the following Ar milling. The structure of the exposed edge of Au/SAM/Al_2O_3/Au multilayer (Figure 3.1) was obtained after the Ar milling process (Plasmalab 80) stopped on the Au bottom electrodes.

I-V curves of Al/Au/SAM/Al_2O_3/Au structure with exposed side edges of different Al_2O_3 layer thickness were performed at room temperature by the Keithley 2430 1KW Pulse Sourcemeter or 6430 Sub-femtoamp Remote Sourcemeter and MM Micromanipulator probe station. Atomic force microscope (AFM) measurements were made by the PicoPlus AFM system (Molecular Imaging, Agilent Technologies) and Scanning electron microscope (SEM) images were recorded using a Hitachi S4300 system. The Al_2O_3 film thickness was confirmed by Spectroscopic Ellipsometers (M-2000V, J.A.Woollam Co. Inc.).

3.3 Results and discussions

SEM images of a cross junction of Al 5 nm/ Au 50 nm/SAM/Al_2O_3 2 nm/Au 50 nm multilayer structure (sample No.328) are shown in Figure 3.1b and 3.1c. Two perpendicular metallic microwires are separated at the junction site by the SAM/Al_2O_3 insulating layer with a combined thickness of 2-3 nanometer. The bottom electrode, deposited by sputtering, has a width ~10 μm and the top electrode, deposited by thermal evaporation, has a width ~7.5 μm with a sharp edge produced by Ar ion milling. The uniformity of the edge profile is significantly improved compared to metal/insulator/metal structures using lift-off process (100, 110). The top Au electrode is composed of two layers which can be seen in Figure 3.1c. The upper layer is the Au etch mask that was defined by photolithography and liftoff. The top layer of the electrode acts as an Ar milling etch mask with its thickness reduced 800 Å to ~ 300 Å, as confirmed by AFM measurement. The lower layer of the top Au electrode is deposited over the entire Al_2O_3 sample area to protect the Al_2O_3 insulating layer from being etched away by the alkaline photoresist developer (used to define the upper layer of the top electrode pattern) and has a thickness of 200 Å. Outside of the top Au layer etch mask, the Ar milling step etches through the lower layer Au, Al_2O_3 and SAM layers to form the electrode structure diagrammed in Figure 3.1a. In our system the etching of Al_2O_3 was significantly slower than Au, requiring the relatively thick Au etch mask and end points were calculated from etch rate calibrations immediately prior to etch runs.

Figure 3.3 shows the typical tunneling characters of Al/Au/SAM/Al_2O_3/Au structure with exposed side edges of different Al_2O_3 layer thickness, indicating good insulating property of SAM/Al_2O_3 layer between Au electrodes. The Al_2O_3 layer thicknesses of sample No.333 and No.328 are 15.4 Å and 19.9 Å, respectively, which were confirmed by the Spectroscopic Ellipsometer. This measurement is consistent with alumina ALD deposition cycles of sample No.333 and No.328 (14 and 18, respectively). The *I-V* curves in Figure 3.3 are fitted by Simmons model (66) to obtain their barrier thickness *s* (nm) and height φ (eV). *I-V* characteristics of sample No.328 were fit by Simmons model to obtain the barrier thickness (23.7 ± 0.4 Å) and barrier height (~ 1.2 eV), which is significantly less than the commonly observed barrier height of ~ 3 eV for Al_2O_3 layers (116, 117) using similar alumina ALD deposition method. This is possibly due to the imperfect bonding of Al_2O_3 with $HSCH_2CH_2OH$, rough morphology of the sputtered Au substrate and the additional β-mercaptoethanol layer decreasing the net barrier height of SAM/Al_2O_3 structure. The same procedures were carried out for sample No.333 & No.374 to acquire the barrier thickness of 19.8 ± 0.6 Å and 29.0 ± 0.2 Å, respectively, using the same barrier height. The thickness of β-mercaptoethanol layer can be estimated by subtracting Al_2O_3 layer thickness (ellipsometer) from the total barrier thickness. Results in Table 1 show 4.4 ± 0.6 Å for sample A and 3.8 ± 0.4 Å for sample B, which are consistent with the typical thickness (3.5-5.0 Å) of β-mercaptoethanol monolayer on Au (111) surface (109, 118). When the Al_2O_3 layer becomes thicker as in sample C, it becomes difficult to estimate the SAM thickness (by subtraction) with the oxide dominating overall tunnel current.

Comparison of the junction tunneling properties of this work to other metal tunnel junctions, having similar exposed edge structures, is listed in Table 3.2. Sample No.333 has a tunneling current density (0.20 ~ 0.75) A/cm^2 at 0.5 V, which is over 1 order of magnitude smaller than 10 ~ 20 A/cm^2 of NiFe/Al_2O_3/NiFe structure at the same thickness and applied voltage (100). Sample No.328 has a tunneling current density (3.4 ~

8.6)×10^{-3} A/cm^2 at 0.5 V with a gap of 23.7 ± 0.4 Å and sample No.374 has a tunneling current density (1.4 ~ 2.3)×10^{-5} A/cm^2 at 0.5 V with a gap ~ 30 Å, which is over 2 orders of magnitude smaller than the literature precedence of ~ 6×10^{-3} A/cm^2 for the Pt/Al/AlO_x(> 30 Å)/Pt structure at 0.5 V (110) and Au/Si_3N_4(35 Å)/SiO_2/Au structure at 0.3 V (111) . This illustrates that ALD of an Al_2O_3 layer on Au/SAM substrate results in a marked improvement in Au-insulator quality.

AFM images of Au film and Al_2O_3 layer on different substrates are shown in Figure 3.4. In general, the surface roughness of noble metal substrate plays a critical role in determining the quality of the insulating layer and device properties (110). The root mean square (rms) roughness of about 0.5 nm for a 20 nm thick Au film on Si/SiO_2/Al (5 nm) substrate is achieved by careful sequential deposition of aluminum and gold film without any break from vacuum (base pressure ~5×10^{-8} torr). The sample topography remains similar and its rms roughness varies between 0.5 and 0.6 nm during the fabrication process of Al/Au/SAM/Al_2O_3/Au structure, which can be observed from Figure 3.4a-c. This confirms that a uniform coating of both β-mercaptoethanol and aluminum oxide layers are on the Au substrate. The conformal nature of the SAM and ALD process also allows good tunnel barrier properties even on top of a rough Au films (rms ~ 2 nm) deposited by a fast thermal evaporation process. As a control experiment, an Al_2O_3 film was grown directly on Au bottom electrode (rms ~ 0.5 nm) without SAM treatment (Si/SiO_2 /Al 5 nm/Au 50 nm/ Al_2O_3 2 nm/Au 50 nm). The surface topography for the untreated Au becomes markedly worse with the rms roughness increasing to 0.9 nm, as shown in Figure 3.4d. The morphology results in a very high current density ~ 10^3 A/cm^2 consistent with electrical shorting.

The topography of different layers in Figure 3.4 also proves the critical role of the β-mercaptoethanol SAM structure in working Au tunnel junctions. The original Au substrate has a grain size of 30 ~ 50 nm and an average grain height smaller than 3 nm in Figure 3.4a. A uniform monolayer of $HSCH_2CH_2OH$ covered the Au substrate and the following Al_2O_3 ALD growth keeps a similar topography as the Au substrate. Figure 3.4b & 3.4c shows the same window of grain size (30 ~ 50 nm). This process is schematically drawn in Figure 3.5a. However, Al_2O_3 growth changes from a layer growth on $HSCH_2CH_2OH$ SAM structure to an island growth when Al_2O_3 is deposited on the Au film directly. The Al_2O_3 thickness (~2 nm) is comparable to the grain height (0.5 ~ 3 nm) of the Au substrate. Therefore, some 'low' grains disappear and some 'high' grains grow after a random distribution of Al_2O_3 islands (see Figure 3.5b). A large distribution of grain sizes (30 ~ 100 nm) and a high rms roughness (0.9 nm) was observed for the Al 5 nm/Au 20 nm/Al_2O_3 2 nm structure in Figure 3.4d.

3.4 Conclusions

Au tunnel junctions of Al/Au/SAM/Al_2O_3/Au structure were achieved by atomic layer deposition of Al_2O_3 onto $HSCH_2CH_2OH$ SAM on an Au bottom electrode. The alcohol terminated SAM acts to grow a conformal monolayer of Al_2O_3 from trimethyl aluminum. The nano-gaps formed at the exposed edge of Au/SAM/Al_2O_3/Au structure can be as thin as 20 Å with a barrier height of ~ 1.2 eV, which makes them excellent candidates for molecular conduction studies. In particular, the conduction mechanisms of ferromagnetic cluster compounds with thiol terminated linkages can be studied with inert Au electrode contacts. One to three orders of magnitude reduction in background tunnel current density are seen compared to related junctions enabling higher performance molecular junctions.

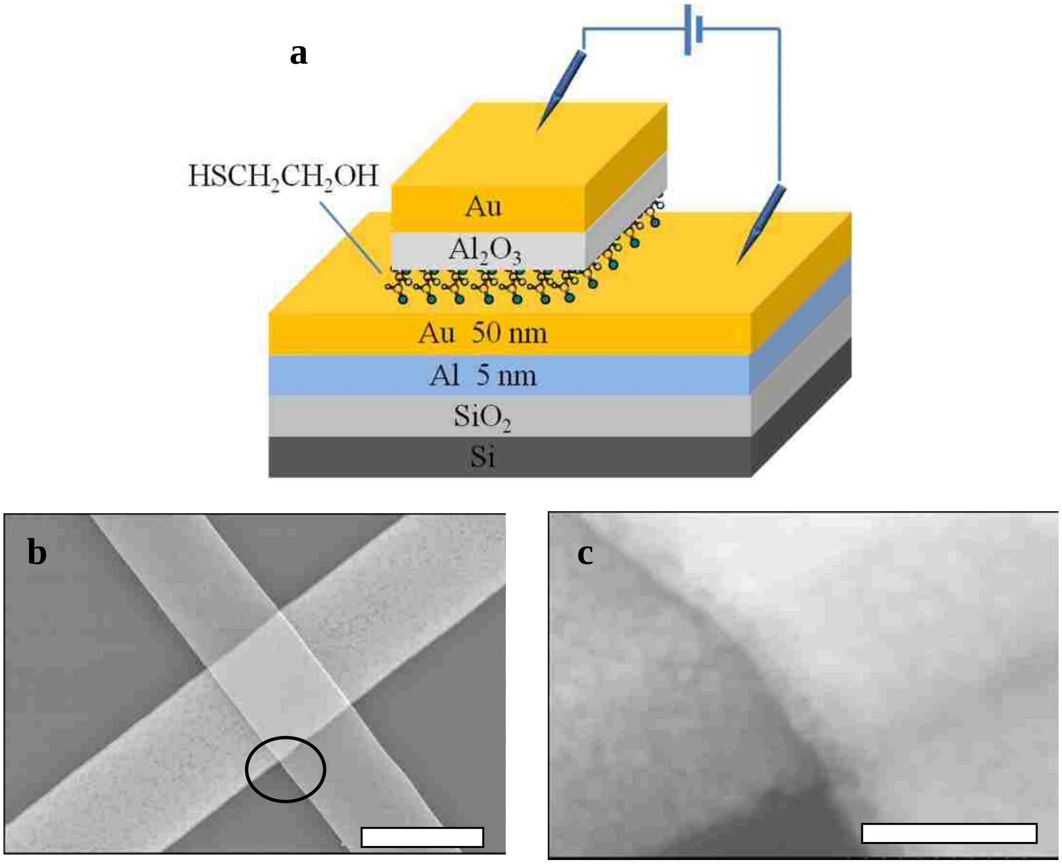

Figure 3.1. (a) Schematic 3D view and (b, c) SEM images of Al 5 nm/Au 50 nm/SAM/Al_2O_3 2 nm/Au 50 nm (sample B) used in this study (scale bar 10um). (c) expanded magnification the circle area in (b), scale bar 250 nm.

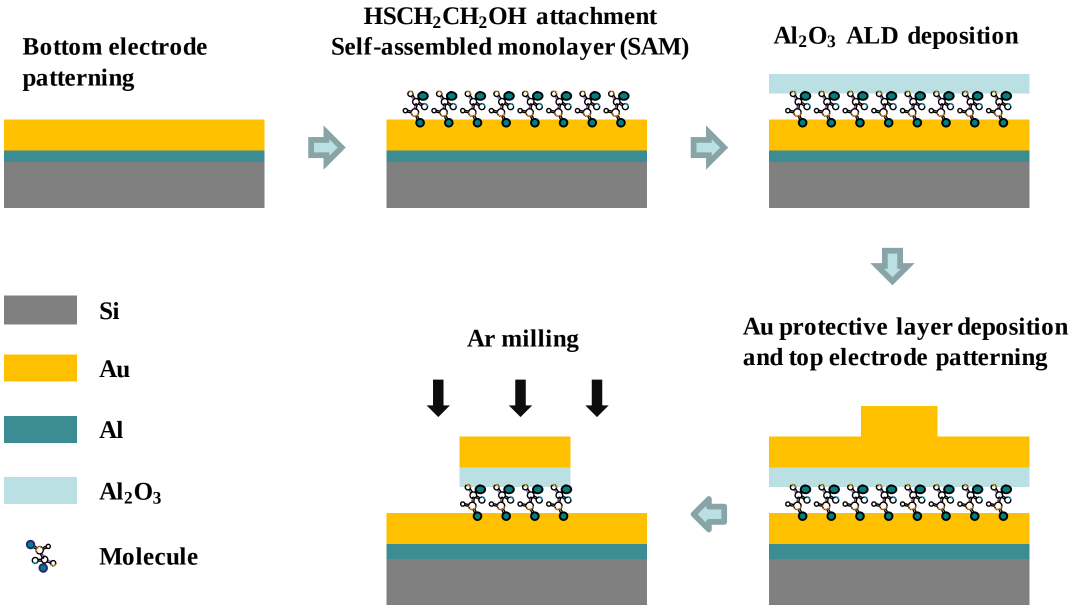

Figure 3.2. Schematic drawing of the nanogap electrode by the exposed edge of $Al/Au/SAM/Al_2O_3/Au$ multilayer.

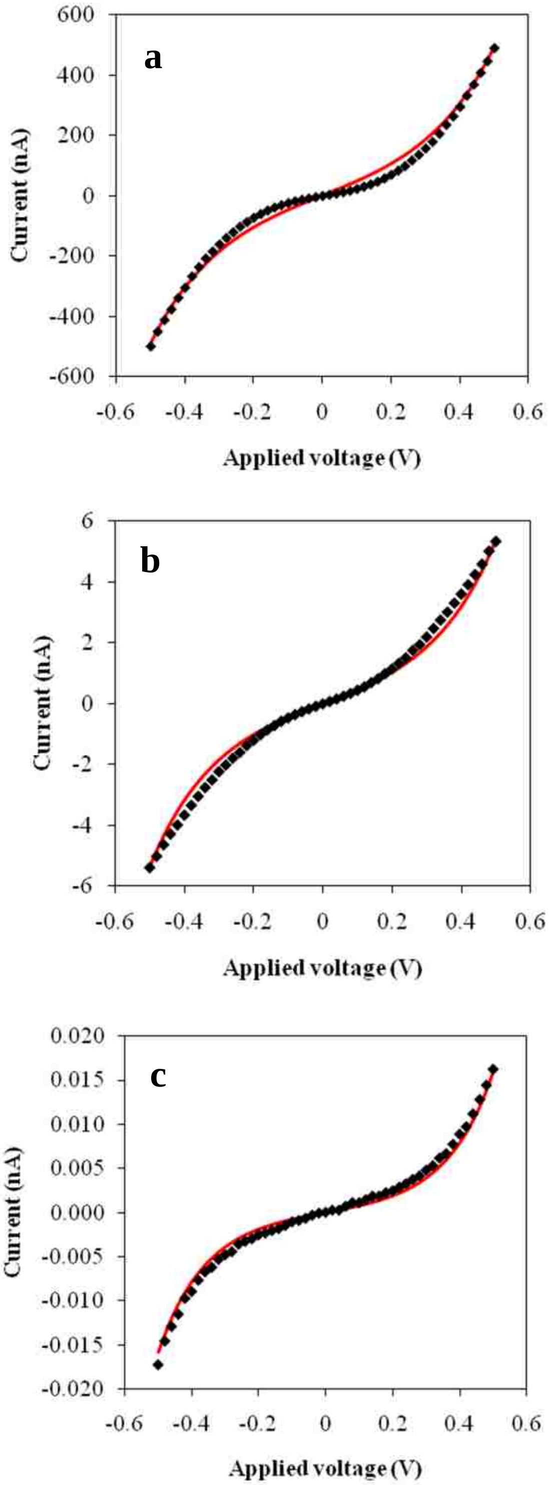

Figure 3.3. *I*-*V* characteristics of Au/SAM/Al_2O_3/Au tunnel junctions with exposed side edges (■) and Simmons simulation (—). The thickness of Al_2O_3 is 15.4 Å (a), 19.9 Å (b) and 27.3 Å (c). The barrier thickness of the simulation curves of (a), (b) and (c) are 19.4 Å, 23.4 Å and 29.0 Å, respectively. A barrier height of 1.2 eV is used for all simulations.

Table 3.1. ALD grown cycles, measured Al_2O_3 layer thickness by ellipsometer, calculated barrier thickness by Simmons simulation and calculated $HSCH_2CH_2OH$ layer thickness of $Au/SAM/Al_2O_3/Au$ structure. Barrier heights of all samples were 1.2 eV by Simmons fit.

Sample No.	ALD grown cycles	Al_2O_3 layer thickness by ellipsometer	Barrier thickness by Simmons simulation	$HSCH_2CH_2OH$ layer thickness
333	14	15.4 ± 0.1 Å	19.8 ± 0.6 Å	4.4 ± 0.6 Å
328	18	19.9 ± 0.1 Å	23.7 ± 0.4 Å	3.8 ± 0.4 Å
374	23	27.3 ± 0.1 Å	29.0 ± 0.2 Å	1.7 ± 0.2 Å

Table 3.2. The barrier thickness, tunneling current density and applied voltage comparison of Au/SAM/Al_2O_3/Au structure with similar noble metal tunnel structures.

Sample	Structure	Barrier thickness (Å)	Tunneling current density (A/cm^2)	Applied voltage (V)
No.333	Au/SAM/Al_2O_3/Au	19.8 ± 0.6	0.20 ~ 0.75	0.5
Ref. [100]	NiFe/Al/AlO_x/NiFe	20.0	10 ~ 20	0.5
No.328	Au/SAM/Al_2O_3/Au	23.7 ± 0.4	(3.4 ~ 8.6)×10^{-3}	0.5
No.374	Au/SAM/Al_2O_3/Au	29.0 ± 0.2	(1.4 ~ 2.3)×10^{-5}	0.5
Ref. [110]	Pt/Al/AlO_x/Pt	> 30.0	~ 6×10^{-3}	0.5
Ref. [111]	Au/Si_3N_4/SiO_2/Au	35.0	~ 6×10^{-3}	0.3

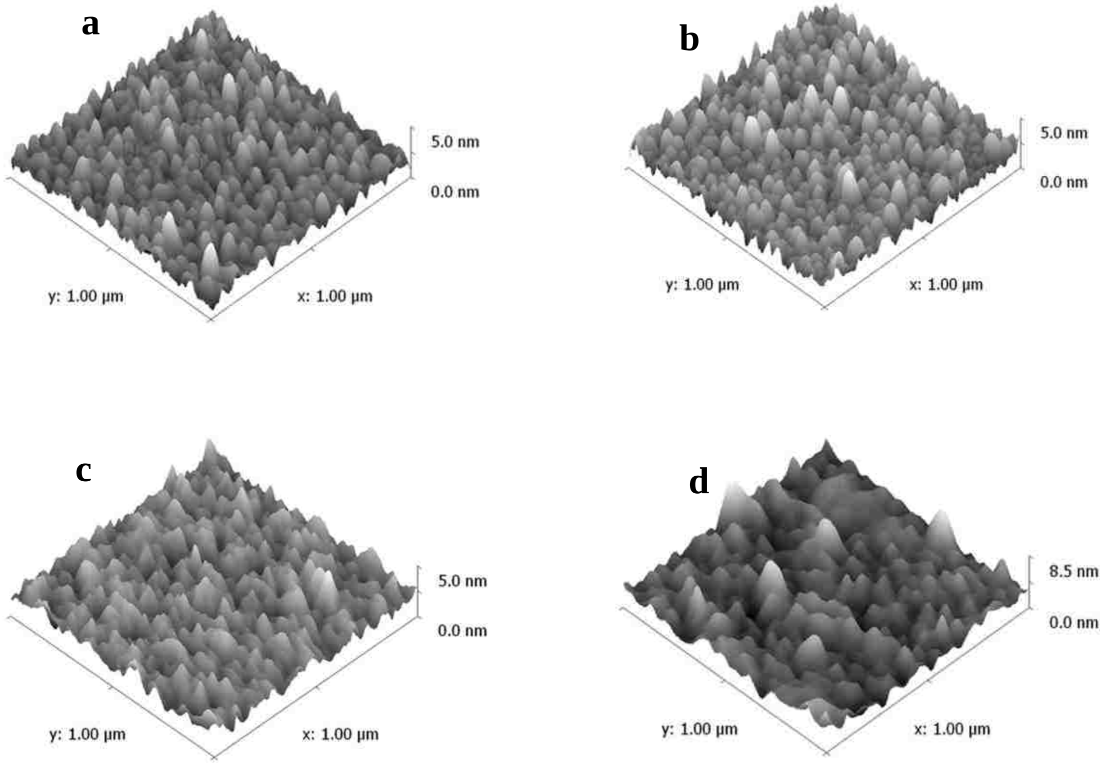

Figure 3.4. AFM images of (a) Al 5 nm/Au 20 nm, (b) Al 5 nm/Au 20 nm/SAM, (c) Al 5 nm/Au 20 nm/SAM/ Al_2O_3 2 nm and (d) Al 5 nm/Au 20 nm/ Al_2O_3 2 nm structures. Rms roughness of (a), (b), (c) and (d) are about 0.5 nm, 0.6 nm, 0.6 nm and 0.9 nm, respectively. All samples use thermally grown SiO_2 on Si wafer as the

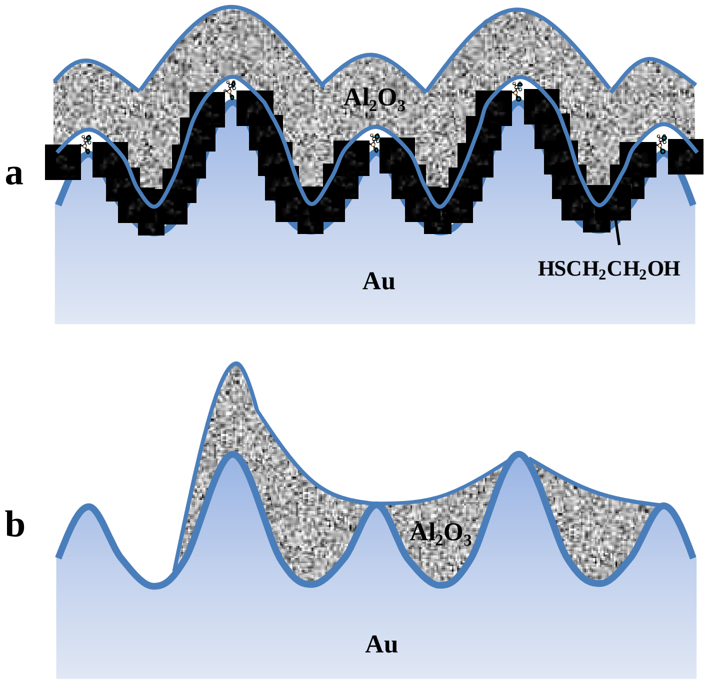

Figure 3.5. Schematic side views of ALD Al_2O_3 layer on Au thin film surface (a) with and (b) without $HSCH_2CH_2OH$ SAM interlayer.

Chapter 4

Molecular attachment on nanogap electrode by Au/Al_2O_3/Au multilayer structure

4.1 Introduction

In Chapter 3, we introduced Au/SAM/Al_2O_3/Au multilayer structures by growing a nano-scale high quality Al_2O_3 insulating layer on monolayer surface chemistry (119). The gap between Au electrodes can be as small as 2 nm and is ideal to study molecular conduction mechanisms with the well controlled Au-thiol surface.

In this chapter, two different molecules were applied to bridge the nano-gap gold electrodes. One molecule is Molecule II already introduced in Section 2.5. Another molecule is a smaller but simpler single metal complex (Molecule III, see Figure 4.1) composed of two 1-Octanethiol, 8-([2,2':6',2"-terpyridin]-4'-ylthio) molecules and a metal core of Fe^{2+}. Control experiments were executed to prove the molecular attachment on both electrodes. A low temperature conductivity study shows the molecular current temperature independent confirming a direct tunneling mechanism.

4.2 Experimental details

4.2.1 Molecular attachment

To attach Molecule II to Au electrodes, the nano-gap electrodes were immersed in a 2mM solution of OMC in a dichloromethane (CH_2Cl_2) solvent for 2 min. Then the sample was sequentially cleaned with isopropyl alcohol (IPA), deionized (DI) water, and nitrogen drying.

Two steps were executed to attach Molecule III to Au electrodes, as show in Figure 4.2. Nano-gap electrodes were first immersed in a 2mM solution of 1-Octanethiol, 8-([2,2':6',2"-terpyridin]-4'-ylthio) in an IPA solvent for 2 hours. After cleaning by IPA, DI water, and nitrogen drying, the nano-gap electrodes were immersed in a 2mM $FeCl_2$ solution for 2 hours to form molecule complexes. Finally, the electrodes were sequentially cleaned with IPA, DI water, and nitrogen drying.

4.2.2 Control experiments

To verify that attached molecules are bridging the top and bottom electrodes, control experiments were executed to reversibly detach and re-attach the molecule across the electrode. This would show that the observed current increase is not due to an artifact of insulator breakdown. After molecular attachment described in last section, the sample was first immersed in a 10 mM solution of β-mercaptoethanol in an IPA solvent for 12 h. After cleaning by IPA, DI water, and nitrogen drying, the sample was immersed in a 2 mM solution of Molecule II/III for another 12h. Then, the sample was sequentially cleaned with IPA), DI water, and nitrogen drying.

I-V curves of the Al/Au/SAM/Al_2O_3/Au structure with/without molecular attachment were performed at room temperature by a Keithley 2430 1KW Pulse Sourcemeter, a

Keithley 6430 Sub-femtoamp Remote Sourcemeter, and an MM Micromanipulator probe station. Low temperature studies were performed at an MMR LTMP-4 cold probe station with a K-20 programmable temperature controller. The temperature cooling rate is ~10 K/min.

4.3 Results and discussions

Transport studies of the Si/SiO_2 100 nm/Al 5 nm/Au 20 nm/SAM 0.4 nm/ Al_2O_3 1.7 nm/Au 20 nm structure (sample No.405) before and after Molecule II attachment are shown in Figure 4.3a. The *I-V* curve of the bare junction shows typical tunnel junction properties. The *I-V* curve of the nano-gap electrode bridged by molecules is close to a linear line. The current at 0.3 V before and after molecule attachment is 1.2×10^{-8} A and 1.7×10^{-7} A, respectively. The current enhancement after molecule II attachment indicates current passing through molecule II dominating the total sample current. If the sample is short from junction failure, the current level will reach 10^{-3} A level at 0.3 V.

Molecular current is defined as the total sample current minus the bare junction current at any bias. The edge length of the top electrode at the junction area is ~10 μm (see Figure 3.1b) and the scale of Molecule II is considered around 2 nm. If all molecules are closely packed with a spacing length of 1 nm, an array of approximately 20,000 molecules covalently attach along the two sides of the top electrode. The average current per molecule was estimated to be 8.0×10^{-12} A at 0.3 V. Therefore, the average molecular resistance is about 3.8×10^{10} Ω, compared to the $HS(CH_2)_{10}SH$ resistance of about 10^9 Ω (62, 120) and the $HS\text{-}(CH_2)_9\text{-}CH_3$ of about 10^{12} Ω (62, 121) by the Probe Scanning Microscopy (PSM) using an applied voltage from -0.3 V to 0.3 V. The Molecule I resistance, measured by a similar NiFe/Al_2O_3/Ni tunnel junction structure, is ~ $4.5\times10^9\ \Omega$ (100). All these comparisons are listed in Table 4.1.

Molecule III has similar *I-V* characteristics as Molecule II, as shown in Figure 4.3. The average current per molecule was estimated to be 8.5 $\times10^{-12}$ A at 0.3 V and the average molecular resistance is about 3.5×10^{10}, close to the calculated data of Molecule II.

The Au-S bond is reversible and it is possible to remove the thiol linkage by mass action/exchange in a thiol-alkane solution. Figure 4.4 shows the control experiment results. The electrode current increased after Molecule II first attachment and returned to the bare junction level after the thiol group exchange of the alkyl tether of Molecule II with the thiol group of β-mercaptoethanol by exposure to a 10 mM solution of β-mercaptoethanol in an IPA solvent for 12 h. The β-mercaptoethanol molecules replaced Molecule II and could not bridge the top and bottom electrodes. This is the reason why the current returned to the original bare electrode current level after the Au-S exchange reaction. The electrode current increased when the sample was immersed in a 2 mM solution of Molecule II for a second time. The observed molecular current was 4.8×10^{-9} A at 0.5 V while the molecular current after the first Molecular attachment was 2.2×10^{-8} A at 0.5 V, indicating a partial exchange of β-mercaptoethanol (~ 22%) by Molecule II. These control experiments confirm that the current enhancement is due to the molecular attachment across the dielectric, not due to an artifact of the breakdown of the dielectric layer within the tunnel junctions.

Figure 4.5a shows the *I-V* characteristics of Molecules (II) attached at the edge of the Au/SAM/Al_2O_3/Au structure at 293 K and 80 K; and Figure 4.5b shows the current passing through the same molecules with an applied voltage of 0.5 V at different temperatures. The constant current over the large temperature range in Figure 4.5 indicates the molecular current is only generated by a tunneling mechanism without any thermal activation. The bare tunnel junction current was also measured at different temperatures and the observed *I-V* curves are temperature independent, consistent with the tunneling process. This result indicates the SAM/Al_2O_3 insulating layer as a high quality film structure without any hopping mechanism defects. The sample was irradiated with light (15mW/cm^2) and no increase current was detected, as shown in Figure 4.6. This result also indicates the molecular current is only through direct tunneling. In particular no photo-exited states at or below the Fermi level within the molecule increase current, indicating that empty electron states are available as conduction channels. Also the photo excitation of carriers does not overcome small defect barriers in the oxide insulator barrier or in contacts. In the case of the prior report(100)and thesis, Molecule I on NiFe leads showed photo current increase and a crude measurement of activation energy of 0.3V, which is likely related to transport through oxide tunnel barrier defects. The work function of Ni is 5.01 eV and is very similar to Au at 5.1eV. Since Au has a higher work function, any barrier to electron transport to the metal center (i.e. occupied states in the molecule at the Fermi energy), would be higher in the Au case compared to Ni (by 0.1eV). However no barrier was experimentally seen in the Au case, therefore no barrier is expected in the Ni case.

Simmons model is used to calculate the barrier thickness (nm) and barrier height (eV) by fitting the observed *I-V* curves (66). The fitting curves are shown in Figure 4.7 a&b. The tunneling area of the bare junction is ~ 75 μm^2. We assume Molecule II as a cubic of *a* =

1 nm. Therefore, the tunneling area of all attached molecules is 1 nm × 10 μm × 2 = 0.02 μm^2. The simulation results show a barrier thickness of 21.7 Å and a barrier height of 1.2 eV for the bare junction without molecule current path. After the attachment of Molecule II, a barrier thickness of 11.6 Å and a barrier height of 1.4 eV is seen for the device. The simulated barrier thickness of Molecule II is consistent with tunneling through the 10-carbon-alkane-tether length in Molecule II, which is around 12 Å to the metal center instead of across the entire 30 Å molecule.

Effective barrier thicknesses for the molecular transport component of electrodes functionalized by Molecule II were calculated for a series of Au/SAM/Al_2O_3/Au samples. The barrier height of bare tunnel junctions and Molecule II are 1.2 eV and 1.4 eV, respectively. All Au tunnel junctions in this chapter were fabricated with 15 Al_2O_3 ALD growth cycles with the resulting thickness of the Al_2O_3 layer of ~ 16.5 Å. The SAM layer thickness is ~ 4 Å, calculated in Chapter 3. Therefore, the total thickness of the SAM/ Al_2O_3 dielectric stack is ~ 20.5 Å, consistent with the barrier thickness of bare tunnel junctions of (21.4 ± 0.8) Å in Figure 4.7. The barrier thickness of Molecule II is (12.3 ± 1.0) Å, consistent with the expected length of the 10-carbon-alkane-tether length of 12 Å.

Figure 4.9 shows the working mechanism of this molecular device. There are two tunneling paths. The first tunneling path is from the top electrode to the bottom electrode directly. This tunneling length is ~ 21.4 Å. The second tunneling path is through Molecule II composed of four 10 carbon alkane tethers and one metal cage. The metal cage can be considered as a metal island between the top and bottom electrodes. Therefore, current can tunnel from the top electrode to the metal cage first and tunnel again from this metal cage to the bottom electrode. Although the barrier height of the 10 carbon alkane tether (1.4 eV) is a little higher than that of the SAM/Al_2O_3 insulating structure (1.2 eV), the length of the 10 carbon alkane tether (~ 12.3 Å) is much smaller than that of the thickness of the SAM/Al_2O_3 insulating structure (~ 21.4 Å) and within the uncertainty of tunnel barrier thickness with the two adjustable parameters. This difference leads to a higher tunneling current density of 8.0×10^{2} A/cm^2 passing through Molecule II compared to that of 1.6×10^{-2} A/cm^2 passing through the SAM/Al_2O_3 insulating stack at 0.3 V.

Since the tunneling current passing through the tether of Molecule II is coherent, the tunneling decay parameter β, introduced in Section 1.6.1.2, can be calculated to describe the 10 carbon alkane tether. The calculated β of Molecule II is 0.96 Å^{-1} by equation (1.24). This result is consistent with the alkane tether β value of 0.6 ~ 1.0 Å^{-1} (62, 63). Table 4.1 shows the comparison of calculated values of barrier thickness, barrier height, β, T_{mol} and resistance of Molecule II & III with similar noble metal contacts. The resistance of Molecule II is larger than the AFM measurement of decanedithiol (120). This is due to a combination of a two-step tunneling of electrons through Molecule II and the additional resistance of the perazylborate ligand. And the resistance of Molecule II is smaller than the AFM measurement of decanethiol in Ref.(121) This is due to the Au-CH_3 contact, not the Au-S contact, between the molecule and the AFM tip. This Au-CH_3 contact increases the total molecular resistance.

Molecule I & II have a similar structure. The only difference is the thiol acetyl group in Molecule I replaced by the hydrogen (thiol) atom in Molecule II. This allows the direct reaction with Au for Molecule II instead of requiring electrochemical activation of Molecule I. With the NiFe electrodes (100), the electrochemical activation process corroded electrodes and was highly irreproducible due to solvent evaporation and HCl formation in the dichloromethane solvent. Thus, we chose to focus on Molecule II. After molecular attachment on metal electrodes, both molecules I & II are identical and should show similar current transport properties through metal-S bonds. The prior study with Molecule I on Ni electrodes with liftoff process showed a barrier height of ~ 0.74 eV (100) that is much smaller than Molecule II on Au electrodes in this study with a barrier height of 1.4 eV. Following the Equation (1.24), the calculated β is 0.74 Å^{-1} for Molecule I on these Au contacts. The prior work on Ni contacts with poor background tunnel current showed the β value of 0.88 Å^{-1}.(100). The resistance of Molecule I is much smaller than that of Molecule II mainly because Molecule I has a much smaller barrier height than Molecule II. A thermal activation energy of ~ 0.30 eV was detected for Molecule I while the I-V characteristics of Molecule II is constant over a larger range at different temperatures. This suggests a defect conduction mechanism through a poorer quality tunnel barrier rather than through molecular conduction. Considering the poor repeatability of experiments in Ref.[100], attempted by myself under the prior student's direct supervision and the observation of oxide layers on Ni electrodes (Ch 2), the data of Molecule I is not comparable in Table 4.1.

Molecule II attachment on the Au with a small barrier height was seen in only a few devices as shown in Figure 4.10. The low current level and curvature are typical for a large tunnel barrier length. The Simmons simulation shows a barrier thickness of 19.9 Å and a barrier height of 0.6 eV for these attached Molecule II arrays. This is very different than the prior work with Molecule I where both low energy (~0.74 eV) and short (13 Å) barrier were inferred from Simmons model. In this case, the barrier thickness is close to the thickness of the insulator layer (22 Å) and difficult to analyze with respect to defects in the electrode structure or decomposition product without metal bridging center.

4.4 Conclusions

Different molecules were attached on the exposed edges of Au/SAM/Al_2O_3/Au tunnel junctions to bridge the top and bottom electrodes. The repeatable Au-S exchange control experiments prove the dominant current passing through molecules. The calculated barrier thickness of ~ 12.3 Å by Simmons model, consistent with the 10-carbon alkane tether length of ~ 12 Å, demonstrates the molecular current tunneling through the metal center of studied molecules. Low temperature and photo current studies show a direct tunneling through the organic tethers to available states at the metal center.

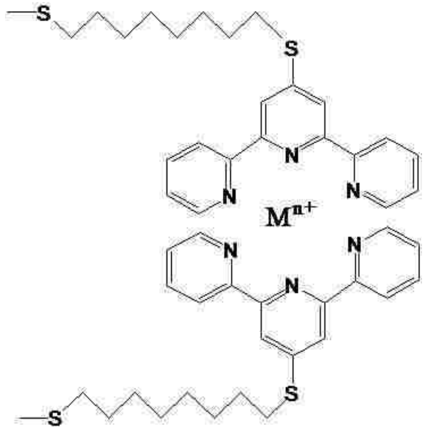

Figure 4.1. Schematic drawing of Molecule III

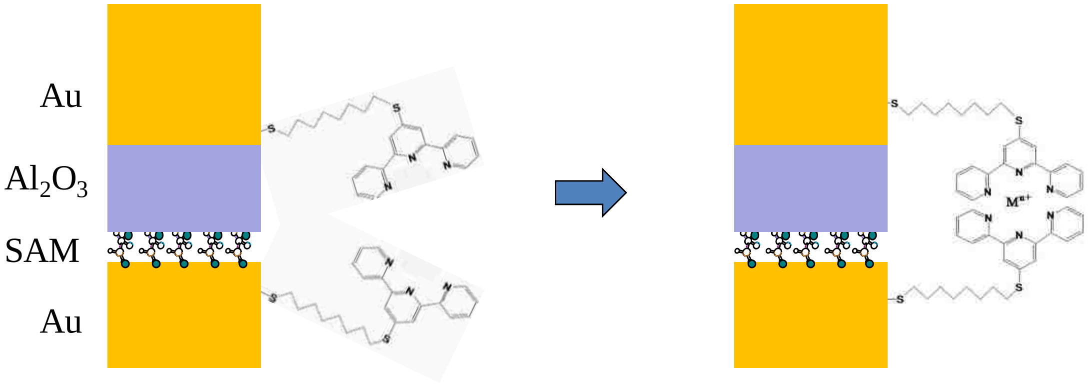

Figure 4.2. Two step attachment of Molecule III to bridge Au electrodes.

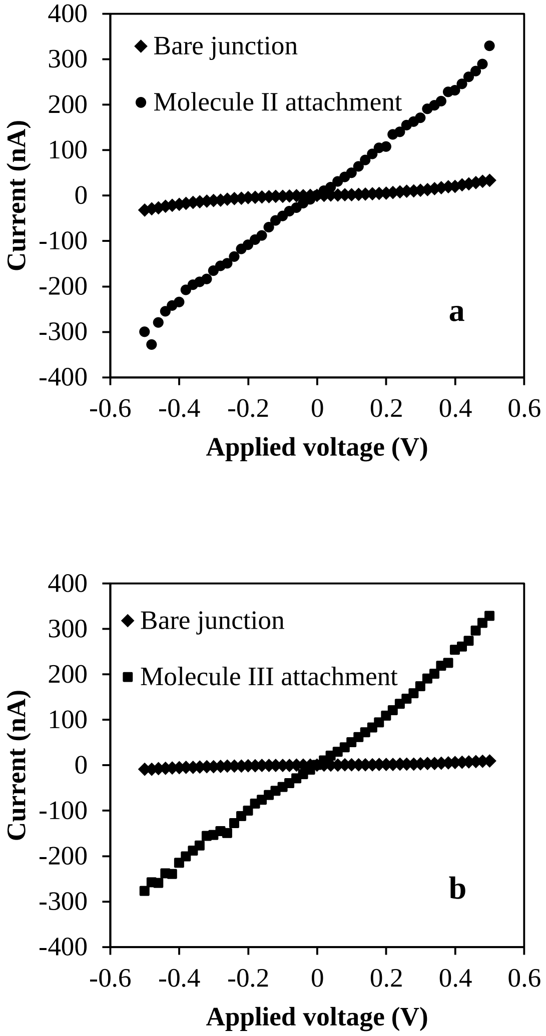

Figure 4.3. *I-V* characteristics of Au/SAM/Al_2O_3/Au tunnel junctions before and after (a) Molecule II and (b) Molecule III attachment.

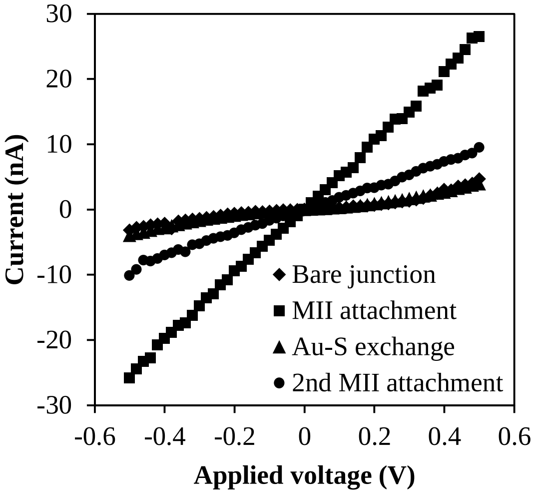

Figure 4.4. *I-V* characteristics of Au/SAM/Al_2O_3/Au tunnel junctions with the Molecule II attachment and the thiol-exchange reaction in a 10 mM β-mercaptoethanol solution.

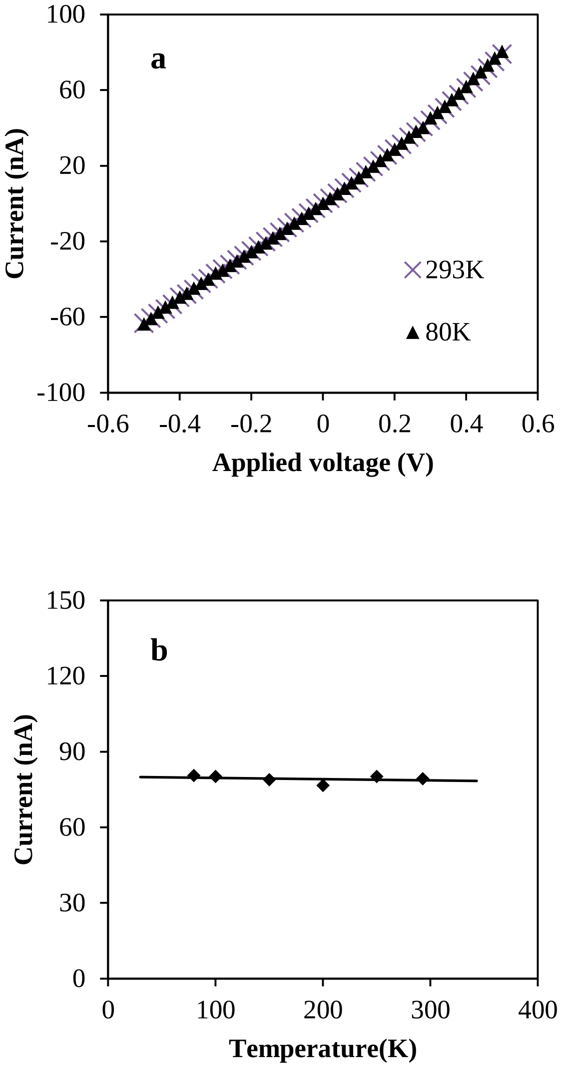

Figure 4.5. (a) *I*-*V* characteristics of Molecules (II) attached at the edge of the Au/SAM/Al_2O_3/Au structure at 293 K and 80 K; (b) Currents passing through Molecule (II) attached along the edge of the Au/SAM/Al_2O_3/Au structure with an applied voltage of 0.5 V at different temperatures.

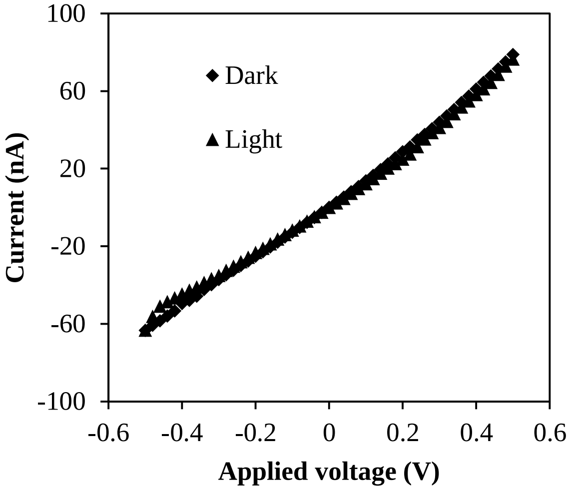

Figure 4.6. *I-V* characteristics of Molecules (II) attached at the edge of the Au/SAM/Al_2O_3/Au structure in dark and light. The incident light density is 15 mW/cm^2.

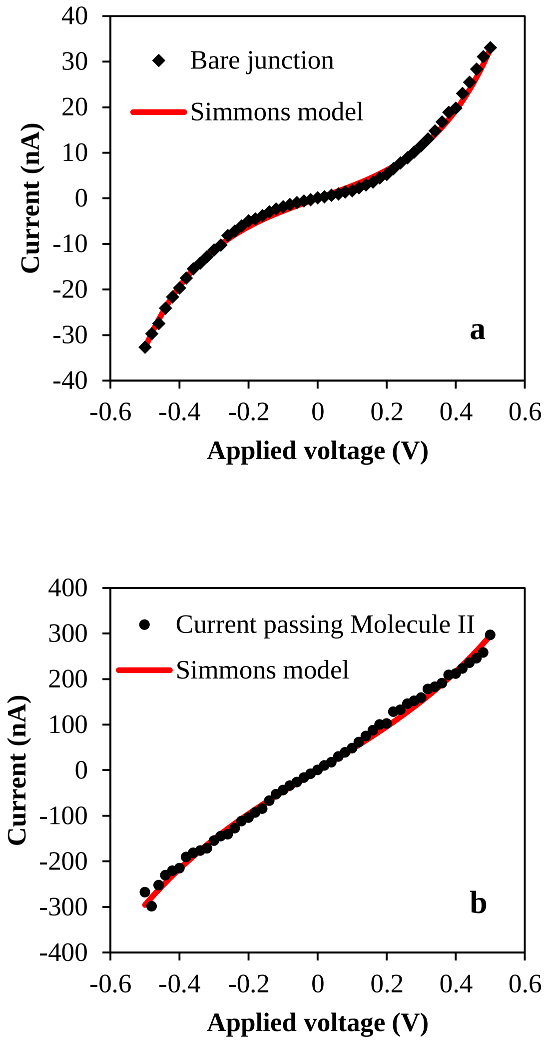

Figure 4.7. *I*-*V* characteristics (■) and Simmons simulation (▬) of (a) a bare Au/SAM/Al$_2$O$_3$/Au tunnel junction and (b) Molecule II current derived from the difference between two curves in Fig. 4.3.

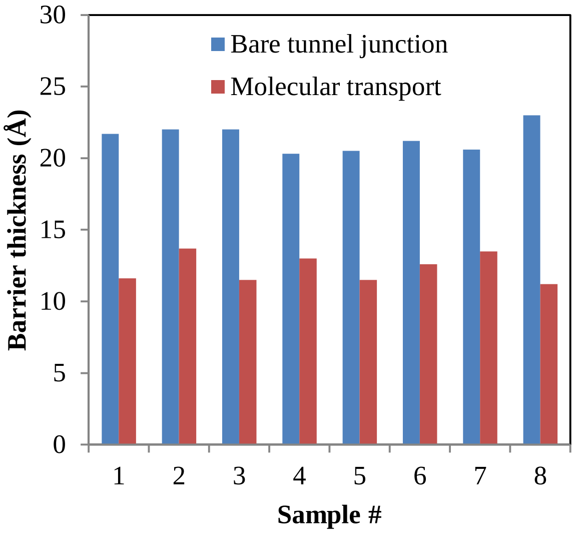

Figure 4.8. Barrier thickness of Au/SAM/Al_2O_3/Au tunnel junctions bridged by Molecule II. The barrier height of bare tunnel junctions and Molecule II are 1.2 eV and 1.4 eV, respectively.

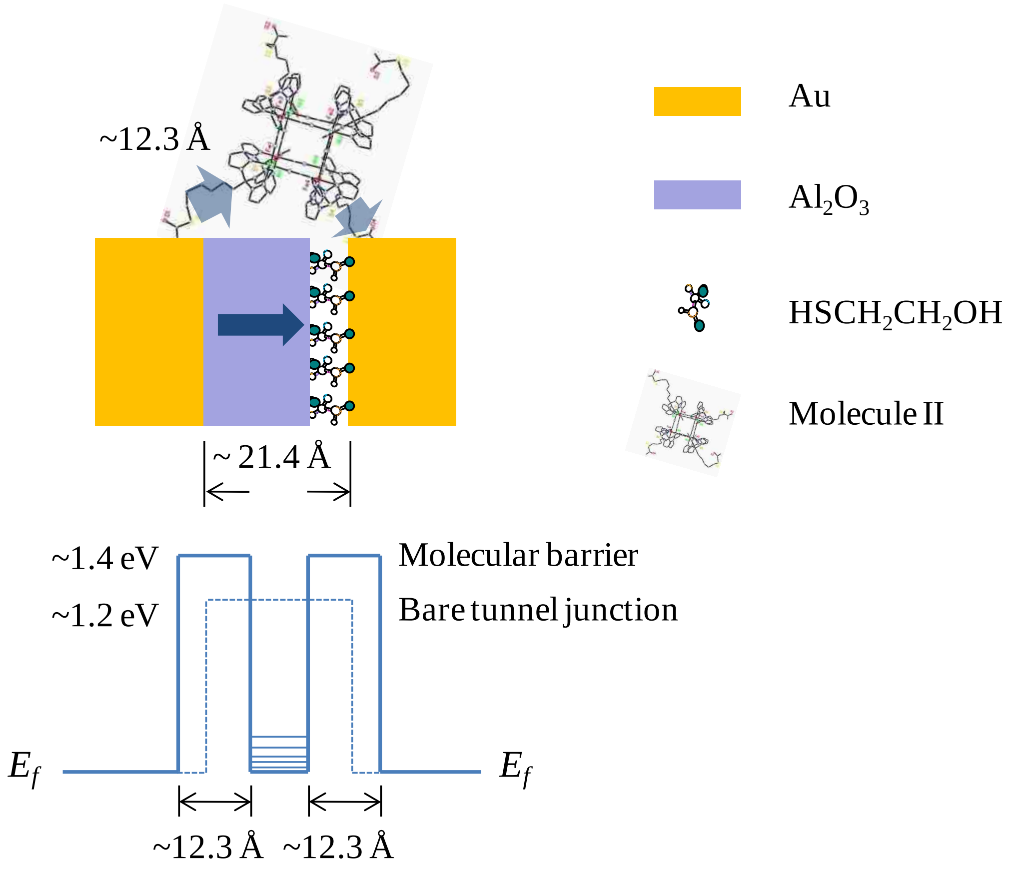

Figure 4.9. Schematic drawing of the current tunneling in a molecular device and the idealized band diagram. E_f is the Fermi energy level of Au electrodes, ~ 1.2 eV and ~ 1.4 ev are the barrier height of the bare tunnel junction and Molecule II, respectively.

Table 4.1. The barrier thickness, tunneling current density and applied voltage comparison of Au/SAM/Al_2O_3/Au structure with similar noble metal contacts.

Molecule	Carbon number	Technique	Barrier thickness (Å)	Barrier height (eV)	β ($Å^{-1}$)	T_{mol}	Resistance per molecule (Ω)
II	10	Au tunnel junction	12.3 ± 1.0	1.4	0.96	$\sim 7.4 \times 10^{-6}$	$\sim 1.0 \times 10^{11}$
I (100)	10	NiFe/Ni tunnel junction	13.0 ± 2.9	~ 0.74	0.74 [1]	$\sim 6.6 \times 10^{-5}$	$1\times10^{8} \sim 3\times10^{10}$
$HS(CH_2)_{10}SH$ (120)	10	AFM [2]	N/A	N/A	0.91	$\sim 1.1 \times 10^{-4}$	$\sim 6.3 \times 10^{8}$
$HS(CH_2)_9CH_3$ (121)	10	AFM [2]	N/A	N/A	0.79	N/A	$\sim 2.0 \times 10^{12}$
III	8	Au tunnel junction	11.2	1.4	0.96	2.1×10^{-5}	$\sim 3.5 \times 10^{10}$
$HS(CH_2)_{10}SH$ (120)	8	AFM [2]	N/A	N/A	0.91	$\sim 2.5 \times 10^{-4}$	$\sim 5.1 \times 10^{7}$
$HS(CH_2)_9CH_3$ (121)	8	AFM [2]	N/A	N/A	0.79	N/A	$\sim 2.0 \times 10^{11}$

Note: 1. The β value of Molecule II in Ref.(100) is 0.88 $Å^{-1}$.

2. All AFM techniques in this table used a gold layer to cover the cantilever tips and a gold substrate to attach molecules.

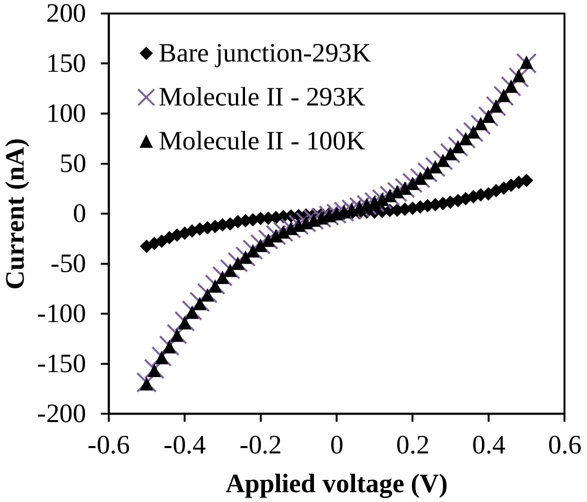

Figure 4.10. *I-V* characteristics of Molecules (II) attached at the edge of the Au/SAM/Al_2O_3/Au structure with a low barrier height of 0.6 eV.

Chapter 5

Fabrication and study of organic photodetectors by Au/Al_2O_3/Au multilayer structures

5.1 Introduction

In Chapter 3, we introduced Au/SAM/Al_2O_3/Au multilayer structures by growing a nano-scale high quality Al_2O_3 insulating layer on monolayer surface chemistry where the gap between Au electrodes can be as small as 2 nm (122). This nano-gap electrode is a good substrate for molecular study. Another application of this nano-gap electrode is the photovoltaic study of organic semiconductors in a nanoscale. This idea can be realized by depositing organic semiconductors between the nano-gap electrodes.

In this chapter, we used sputtering, atomic layer deposition (ALD), and Ar milling to fabricate the exposed edge of Au/Al_2O_3/Au multilayer structure to minimize the contact resistance between organic semiconductor and metal electrodes. The well characterized Copper (II) phthalocyanine (CuPc) was chosen as the organic semiconductor because of its stability and facile deposition by thermal evaporation (88, 123). Large photocurrent enhancement over 50 times that of bulk CuPc film was observed due to the gap between Au electrodes approaching 10 nm. Schottcky barrier contact resistance was found to be the primary limiter of charge injection into the organic film.

5.2 Experimental details

The structure of CuPc film photodiode on the exposed edge of Al/Au/Al_2O_3/Au/Ti multilayer is schematically shown in Fig. 5.1. Figure 5.2 shows the fabrication flow. Prior to sample preparation, the SiO_2 wafer (Silicon Quest International, Inc.) with a 1000 Å thick SiO_2 layer grown thermally on Si substrate was sequentially cleaned with acetone, isopropyl alcohol (IPA), deionized (DI) water and dried in a nitrogen stream. The bottom electrode was lithographically patterned to a size of 2 mm × 10 mm and 50 Å of Al and 500 Å of Au were thermally evaporated using a Cressington 308R Coating System. The Al_2O_3 insulating layer was fabricated in three steps. First, 10 Å of Al was sputtered in an AJA International high vacuum sputtering system with a base pressure of 8.0×10^{-8} torr and oxidized in an O_2 flow at 60 mTorr for 2 min to form an Al_2O_3 seed layer with a thickness of ~ 12 Å. Then atomic layer deposition of Al_2O_3 (38, 88, 188, 488, and 988 Å for sample A (No.347), B (No.311), C (No.339), D (No.359), and E (No.357), respectively) was carried out in a Cambridge Nanotech Savannah 100 system. In order to protect Al_2O_3 film from being etched by the alkaline photoresist developer, 200 Å of Au was sputtered on the Al_2O_3 insulating layer. The top Ti layer (500 Å for sample A, B & C and 2000 Å for sample D & E) was lithographically patterned into microwires (8 μm × 1000 μm) by e-beam evaporation in a Torr International EB4P series system. Ar ion milling at the Plasmalab 80plus system was carried out to expose the edge of Au/Al_2O_3/Au structure by etching 200 Å Au protection layer and the whole Al_2O_3 insulating layer. The top Ti pattern was also partially etched and the remaining Ti layer was then plasma oxidized with 60 mTorr of 1:1 Ar/O_2 gas mixture to form an insulating TiO_2 thin film on the surface. Ti/TiO_2 on probe station contact pad areas was removed by

0.05 M HCl solution to expose Au surface for probe attachment. Finally, CuPc (Aldrich Chemical, 99% purity) was thermally deposited on the exposed Au/Al_2O_3/Au/Ti/TiO_2 structure area using a shadow mask.

All *I-V* characters were performed at room temperature by Keithley 2430 1KW Pulse Sourcemeter or 6430 Sub-femtoamp Remote Sourcemeter at the MM Micromanipulator probe station. AFM measurements were made by a tapping mode AFM (Digital Instruments Multimode) and SEM images were recorded using a Hitachi S4300 system. The Al_2O_3 film thickness was confirmed by Spectroscopic Ellipsometers (M-2000V, J.A.Woollam Co. Inc.). The light source for the photoconductivity experiment was manufactured by Micro-Lite FL3000D. The maximum irradiated power reaching samples was 15.8 mW/cm^2.

5.3 Results and discussion

Figure 5.3(a) shows the optical microscope image of sample A (5 nm Al/50 nm Au/5nm Al_2O_3/20 nm Au/Ti/TiO_2) bare tunnel junction structure without CuPc deposition. Each top electrode has a length of 1000 μm and a width of 8 μm. The SEM image of the circled area in Figure 5.3(a) is shown in Figure 5.3(b). The grains of the bottom Au electrode are clearly observed and the top electrode is covered with a TiO_2 layer. A step height of 60 nm for the top electrode is obtained from the 3D AFM image in Figure 5.3(c). Thus the thickness of Ti/TiO_2 structure is about 30 nm after over etching the Al_2O_3 insulating layer that is over the bottom electrode. The purpose of the top Ti/TiO_2 layer is to block current flow from the relatively large upper surface of the top Au electrode to the bottom Au electrode. Thus, the current path between Au electrodes *via* CuPc film can be controlled at the nano-scale film thickness at the pattern edge, as the arrow shown in Figure 5.1. The leakage current of these tunnel junctions through the Al2O3 layer in the planar area between top and bottom electrodes is very low (~ 10^{-12} A at 0.5 V) for sample A and even lower for other samples having larger Al_2O_3 thicknesses.

Figure 5.4(a) shows both dark and photo current versus applied voltage of sample A deposited with a 70 nm CuPc film. The dark current, 3.0×10^{-9} A at 0.5 V, is 3 orders of magnitude larger than the leakage current of bare tunnel junctions, confirming that most of the current flows through the CuPc film. The net photocurrent-voltage characteristics of sample A (5nm gap width), calculated by subtracting the dark current from photocurrent in Figure 5.4(a), is illustrated in Figure 5.4(b). The net photocurrent increases with an increasing incident light intensity. A linear plot (linear regression of ~1.2) of the logarithm of the photocurrent (measured at 0.5 V) versus the logarithm of light intensity is shown in Figure 5.4(c). It is very clear that there is a power law dependence of the photocurrent on the incident light intensity. The corresponding exponent value is about 0.53, which is consistent with reports (0.5 ~ 1.0) in the literature (124).

The relationship between net photocurrent and the electrode's gap distance (also the thickness of Al_2O_3 layer) is demonstrated in Figure 5.5. All samples were measured with an incident light intensity of 15.8 mW/cm^2 and an applied voltage of 0.5 V. Photocurrent increases when the gap distance decreases from 100 nm to 20 nm. A large photocurrent enhancement is observed when the gap scale is approaching 10 nm. The average photocurrent of 6.2×10^{-9} A with a 10 nm gap is almost over 10 times larger than the

5.2×10^{-10} A of a 20 nm gap, and over 50 times larger than the 1.1×10^{-10} A of a 100 nm gap. This enhancement shows the important role of the gap distance to the generated photocurrent.

The CuPc carrier recombination length can be calculated from observed photocurrents using a simple model, in which the top and bottom Au electrodes are considered as parallel plates, drawn schematically in Figure 5.6(a). The width of plates is equal to the thickness of the top Au electrode (*W*). The gap between parallel plates (*D*) is a combination of Al_2O_3 layer and half of the top Au layer (10 nm). The current flux is from the top to bottom through CuPc film (the dark region in Figure 5.6(a)) when a higher electric potential is applied to the top Au electrode. For a semiconductor film, the steady-state photoconductivity is given by (1)

$$\Delta\sigma = \frac{e\eta I\lambda\tau\mu}{hcD} \tag{5.1}$$

where e is the electron charge 1.6×10^{-19} C, η is the efficiency of photons converting to free electron-hole pairs and as assumed to be 0.5 in this work, I is the light intensity 15.8 mW/cm^2, λ is wavelength of the incident light (600 nm is used here), τ is the recombination lifetime of the photogenerated carriers, μ is carrier mobility, h is Planck's constant, c is velocity of light, D is the thickness of the semiconductor film, $\Delta\sigma$ is the steady-state photoconductivity which can be calculated from the observed photocurrents in Figure 4.4. When a voltage U (0.5 V) is applied on the parallel plate model in Figure 5.6(a), the carrier recombination length is given by

$$L_D = \mu E \tau = \frac{U\mu\tau}{D} \tag{5.2}$$

where E is the electric field intensity of the dark region in Figure 5.6(a) . So

$$L_D = \Delta\sigma \cdot \frac{Uhc}{e\eta I\lambda} \tag{5.3}$$

Table 5.1 shows the calculated carrier recombination length with different gap distances and applied voltages. The calculated carrier recombination lengths with a gap distance of 20 nm, 50 nm and 100 nm, respectively, are smaller than the corresponding electrode gap distance. Often the electrons recombine with the holes rather than reach the Au electrodes.. The calculated effective recombination length of 5nm gap and 10 nm gap are much larger than the physical length because equation (5.1) is for semiconductor bulk films, whose thickness is larger than the carrier recombination length of this semiconductor material. In sample A & B, the carrier travel distance is within 10 nm so that the majority electrons and holes can reach electrodes to generate photocurrent resulting in longer effective recombination lengths. Sample B has a longer path length and subsequently larger volume for electron/hole pair generation from the light, which leads to a larger photocurrent of sample B than that of sample A. In equation (5.3), the applied voltage U is directly proportional to L_D. When the applied voltage between two electrodes is increased, a larger effective carrier diffusion length is generated.

Four-point probe and two-point probe methods were used to measure the contact resistance between Au electrodes and CuPc film and bulk conductivity. The top electrodes in Figure 5.3(a) were used as probes with a distance of 150 μm between adjacent electrodes. A contact resistance of 3×10^7 Ω and a bulk CuPc resistance of 3×10^9 Ω are obtained. Our observed CuPc conductivity is 6×10^{-9} Ω^{-1}cm^{-1}, that is within the experimentally observed range of 10^{-10} ~10^{-8} Ω^{-1}cm^{-1} from literature (124-126). When the gap scale between electrodes approaches 5 nm, the CuPc resistance should decrease to 3×10^9 Ω × (5 nm/150 μm) = 1×10^5 Ω while the contact resistance still keeps a level of 10^7 Ω. This illustrates that the contact resistance is dominant in all *I-V* measurements.

It is interesting that both dark and light *I-V* curves of all samples show diode characteristics. In Figure 5.7(a), with sample A in the dark, a large current of 3 nA was detected when the top electrode was applied with + 0.5 V while a small current of 0.3 nA was detected when the bottom electrode was applied with the same potential. However, sample A should have a symmetrical *I-V* curve because of the symmetric contacts of Au/CuPc/Au. The only explanation is that Schottky junctions are formed between Au and CuPc for samples in this work while Ohmic contacts are generally assumed for the bulk measurements since with longer path lengths the bulk organic resistance dominates the measurement. The energy level diagram, for all samples, is drawn in Figure 5.8 to explain the observed diode behavior and contact resistance. We assume that the Schottky barrier height is *a eV* and the band gap between CuPc HOMO and Fermi level is *(a-b) eV* without any applied bias (V_{DS} = 0 *V*), as illustrated in Figure 5.8(a). When -0.5 V is applied on the bottom electrode, a potential drop between the top electrode and CuPc film (V_1) and a potential drop between the bottom electrode and CuPc film (V_2) are generated. V_1 has a larger value than V_2 because the contact area of the top electrode with CuPc film is smaller than that of the bottom electrode, which leads to a larger contact resistance of the top electrode than that of the bottom electrode (see Figure 5.1). As mentioned above, the contact resistance between Au electrodes and CuPc film is far larger than the CuPc film resistance. So $V_1 + V_2 \approx 0.5$ V and a horizontal energy level of the CuPc film is drawn in Figure 5.8(b) & (c). It is obvious that holes need to overcome one large barrier a eV and one small barrier $(b - V_2)$ eV in Figure 5.8(b) and only need to overcome one barrier a eV in Figure 5.8(c).

5.4 Conclusions

CuPc thin films were successfully deposited between electrodes with a gap distance smaller than the CuPc carrier recombination length. The 10 nm-gap photocurrent of CuPc film is over 10 times larger than 20 nm-gap photocurrent and over 50 times larger than 100 nm-gap photocurrent. This large photocurrent enhancement is the result of the nano-gap's size being shorter than the CuPc carrier recombination length thereby minimizing the recombination of electron-hole pairs. The large Schottky barrier contact resistance between the small area top Au electrode and the CuPc film is responsible for the diode *I-V* characteristics of devices in this work and is the primary limiter of efficiency.

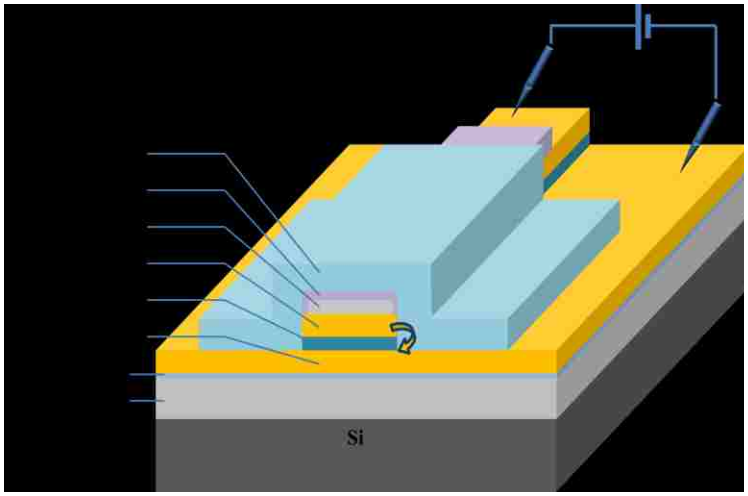

Figure 5.1. Schematic side view of the Al/Au/5 nm Al_2O_3/Au/Ti/TiO_2/CuPc device used in this study.

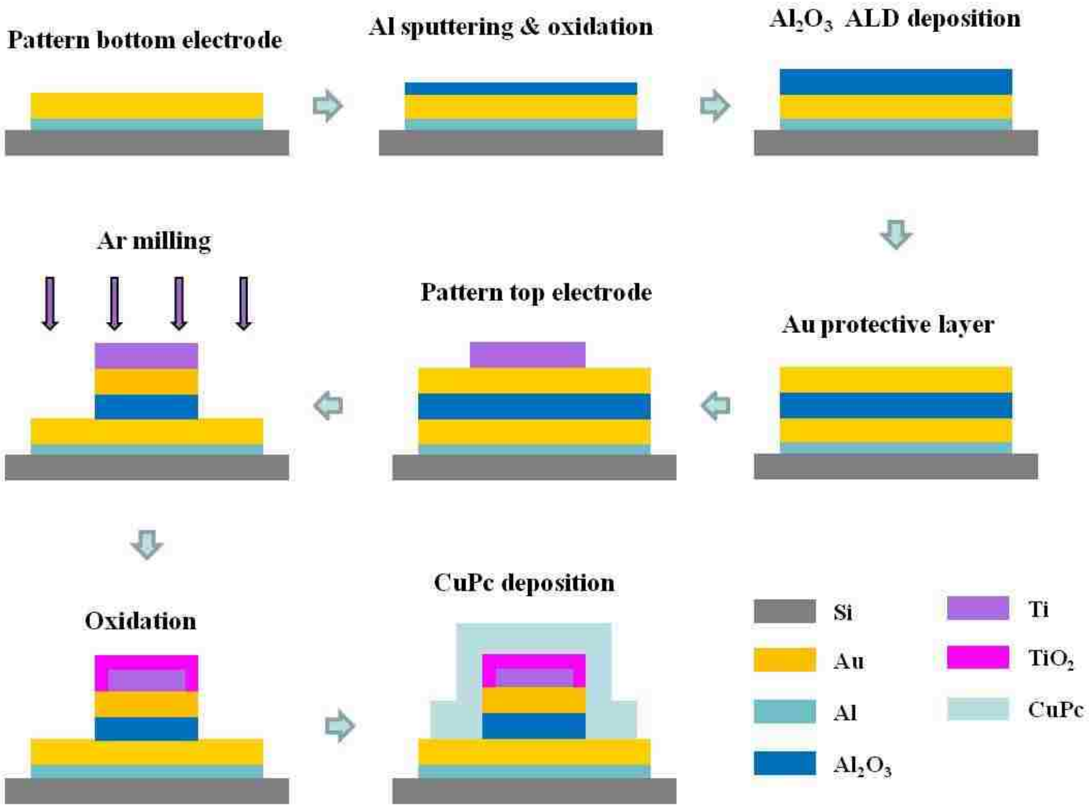

Figure 5.2. Schematic drawing of a photodetector with an $Al/Au/Al_2O_3/Au/Ti/TiO_2/CuPc$ structure.

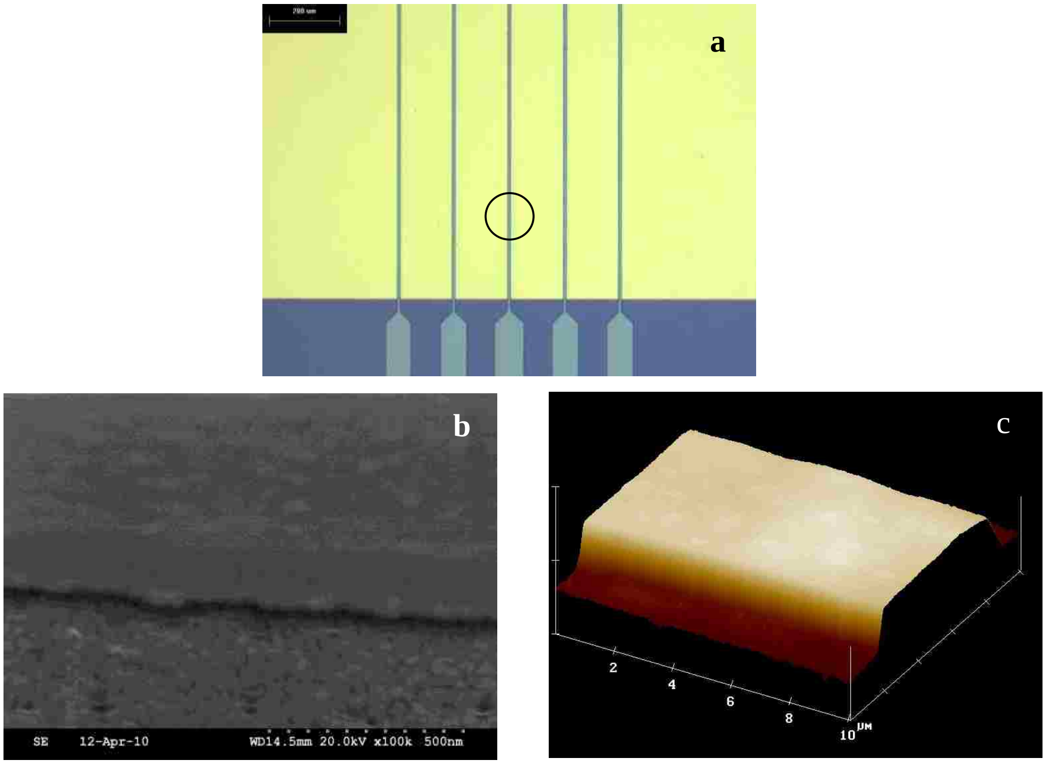

Figure 5.3. (a) optical microscope image of the bare tunnel junction with Al/Au/5 nm Al_2O_3/Au/Ti/TiO_2 structure and (b) SEM and (c) AFM images of the circle area in (a). The scale bar in (a) is 200 μm and *z* scale bar in (c) is 100 nm in the vertical direction. The insert image in (c) is the profile analysis of the top electrode.

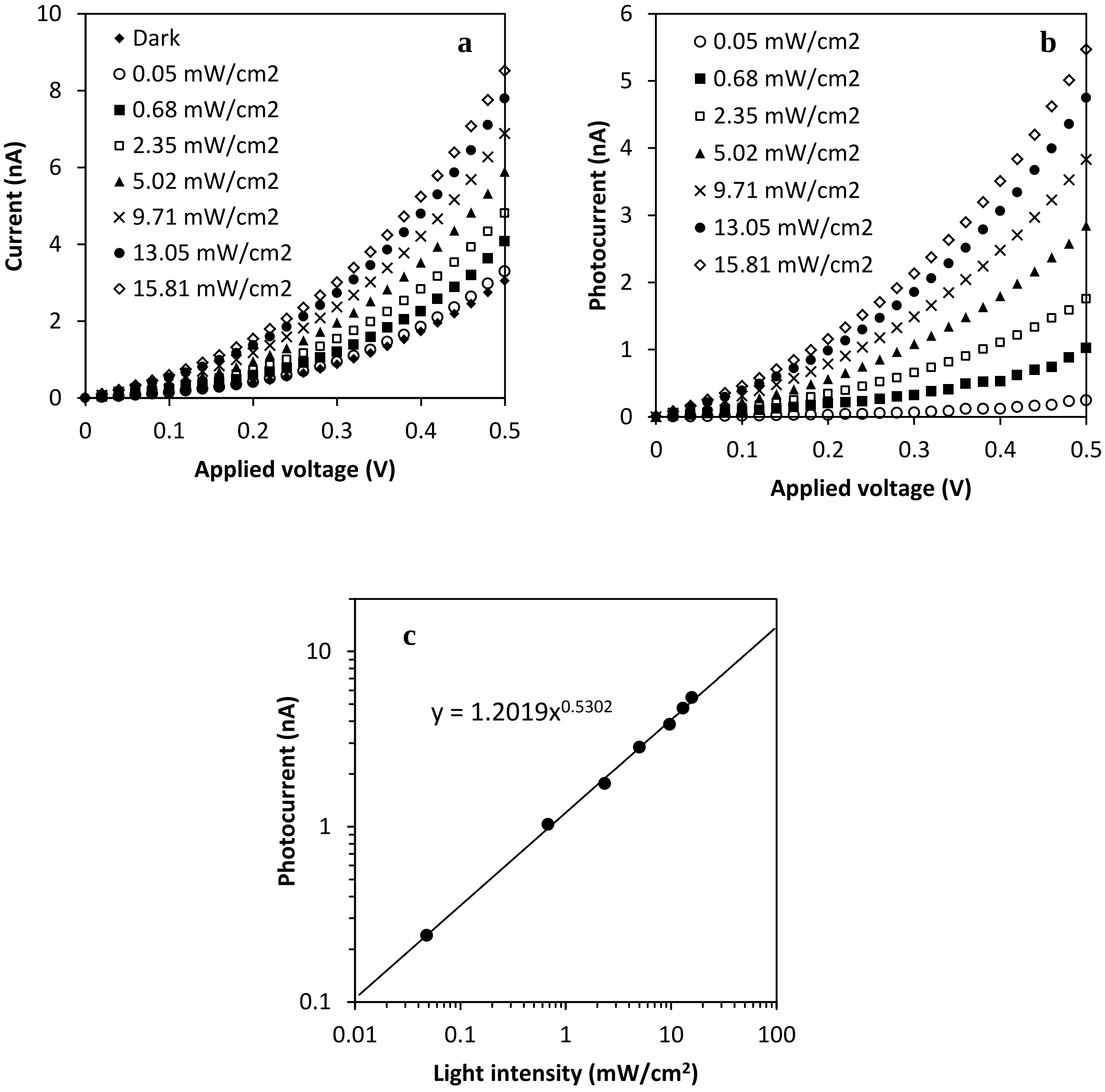

Figure 5.4. (a) Total photocurrent-voltage and (b) net photocurrent-voltage characteristics of Al/Au/5 nm Al_2O_3/Au/Ti/TiO_2/CuPc devices measured at room temperature with different light intensity and (c) variation of photocurrent with light intensity (applied voltage 0.5 V).

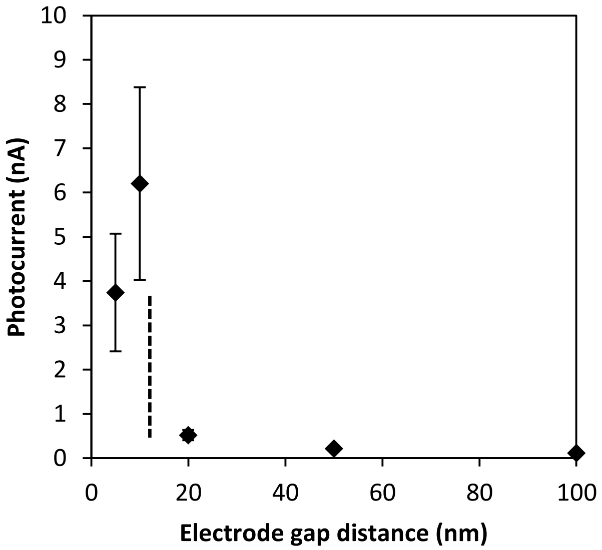

Figure 5.5. Net photocurrent *versus* the gap distance between Au electrodes. The incident light intensity is 15.8 mW/cm^2 and applied voltage is 0.5 V.

Table 5.1. The carrier recombination length (nm) with different gap distances derived from the real photocurrent in Fig. 5.4.

Applied voltage (v)	Electrode gap distance (nm)				
	5	10	20	50	100
0.2	11 ± 4	25 ± 9	2.3 ± 0.4	2.5 ± 0.4	2.9 ± 0.8
0.4	32 ± 11	71 ± 25	7.4 ± 1.6	7.9 ± 1.4	7.5 ± 2.2
0.5	49 ± 17	94 ± 38	13 ± 3	11 ± 2	11 ± 3

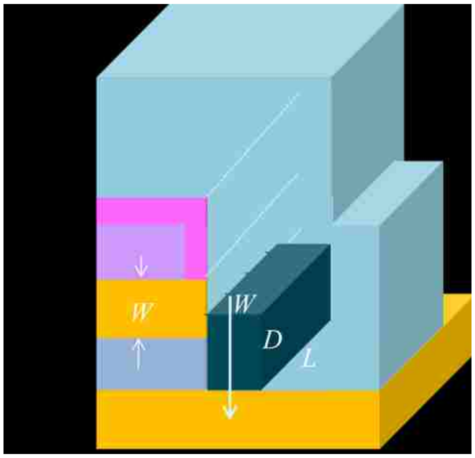

Figure 5.6. Schematic drawing of the model used to calculate CuPc carrier recombination length.

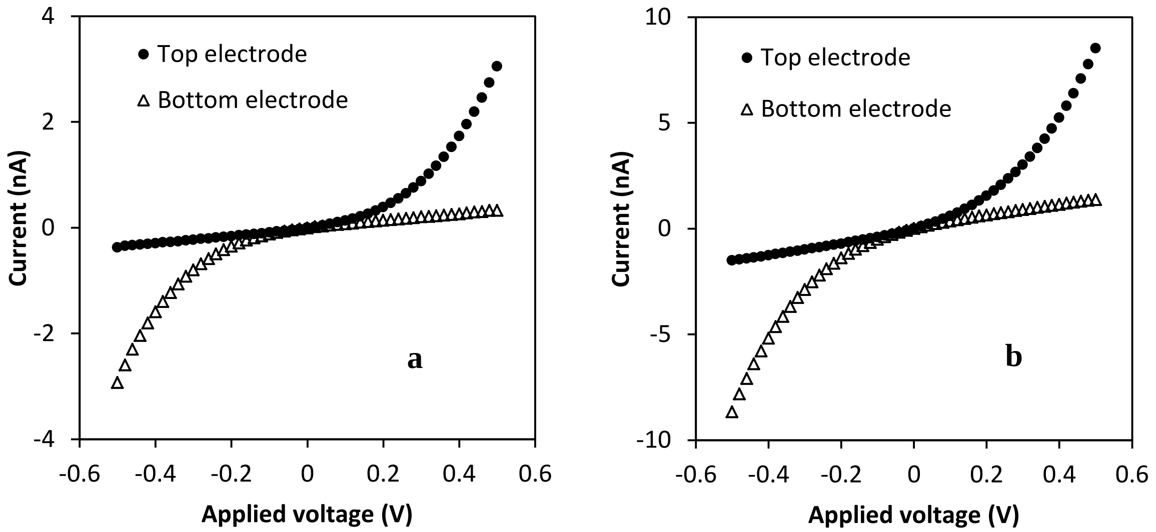

Figure 5.7. (a) Dark and (b) light current-voltage characteristics of Al/Au/5 nm Al_2O_3/Au/Ti/TiO_2/70 nm CuPc device measured by (•) top electrode and (Δ) bottom electrode connecting to the power source. The incident light intensity is 15.8 mW/cm^2.

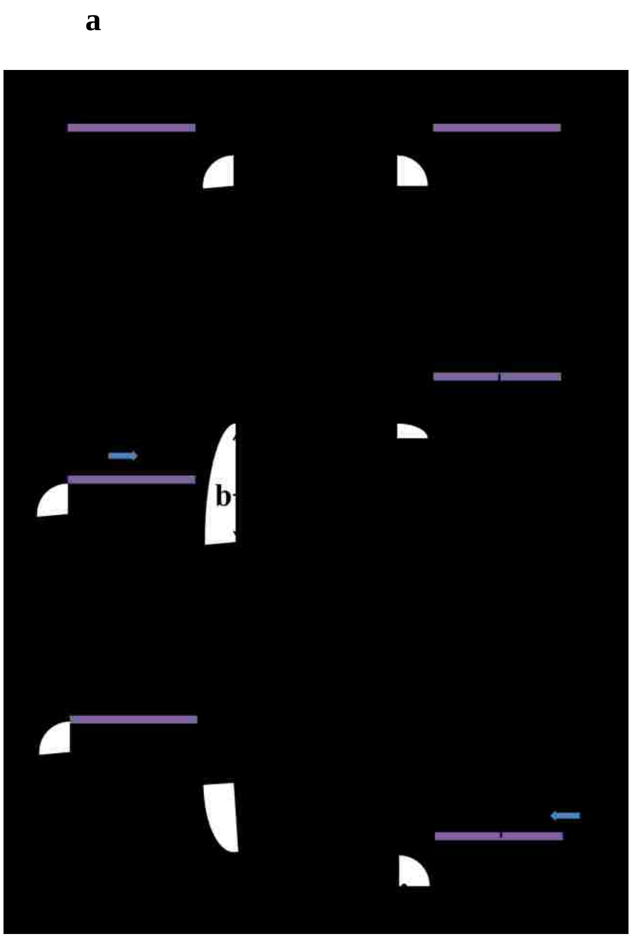

Figure 5.8. Energy level diagram for the Al/Au/5 nm Al_2O_3/Au/Ti/TiO_2/70 nm CuPc device: (a) zero bias; (b) V_{DS} = -0.5 V and (c) V_{DS} = 0.5 V with power source connecting to the bottom electrode. V_1 & V_2 are the voltage drops between top & bottom electrodes, respectively; $V_1 + V_2 \approx 0.5$ V and $V_1 > V_2$.

Chapter 6

Growth study of lateral ZnO nanowire growth from the exposed edge of Si/Al_2O_3/Si trilayer structures

6.1 Introduction

The previously discussed multilayer electrodes have approximately 10,000 molecules spanning nm-scale gaps over the 10 linear microns of junction length. If we can couple an orthogonal pattern of nm-scale dimension it would be possible to develop electrodes that isolate single molecules. A promising approach is to have nanowires projecting over the edge of multilayer electrodes to cast nm-scale shadows in a line of site deposition of an insulator which would leave only a few nm^2 area for molecular attachment on the electrode, isolating single molecules. ZnO nanowires are promising due to their ease of growth and controlled nucleation sites that can be incorporated into the electrode geometries. Our group has generated nm-scale gaps in line-of-site depositions successfully by carbon nanotubes (CNTs) that showed reduction in critical dimension by line incident angle and nanowire height (101, 127, 128). However, this approach requires controlled lateral growth from defined locations and control of nanotube/wire diameter. To control the diameter of CNTs, one can take advantage of the angstrom scale precision of film thickness at a thin-film multilayer pattern edge to control the width of a catalyst line. This thickness was used to determine the diameter of CNTs growing from pattern edge. However, these CNTs were not rigid or straight enough to be used as shadow masks. ZnO NWs are rigid and straight and are well suited for shadow lithography applications.

Among 1-D nanostructures, ZnO nanowires (NWs) have become an actively researched area because of their beneficial semi-conductive properties (a wide bandgap of 3.37 eV and large exciton binding energy of 60 mV), easy synthesis (129, 130), photo catalytic activity (131, 132) and potential for integration into the sensor platform (133, 134). Grown with the vapor-liquid-solid (VLS) mechanism, the position and diameter of ZnO NWs are well controlled by the location and size of metal catalysts (especially Au) (131, 135-140). Recently, catalyst-free ZnO NWs have been developed (141-146) to simplify the fabrication process and eliminate potential contamination in semiconductor devices. ZnO islands or films formed first by physical deposition or chemical synthesis provide the nucleation area for the growth of 1-D nanostructures.

The control of location, diameter and length of NWs are critical for nanodevice fabrication. Several reports demonstrated the vertical growth of ZnO NWs on patterns of catalyst (131, 135-138) and the spatial location of patterned catalyst determines the position of ZnO NWs, which is critical for applications such as light-emitting diodes (LEDs) and field emitters (131, 147, 148). Lateral growth of ZnO NWs along a thin film pattern edge offers another approach to realize controlled lateral growth. Trench Au/Si electrodes were fabricated and NWs grew from the sidewall of Au layer to bridge trenched electrodes (149). ZnO patterns (150, 151) or nanoparticles (152) have been deposited to realize the horizontal growth of those catalyst-free ZnO NWs on Si substrate.

This chapter focuses on the lateral growth of ZnO nanowires from the edge of $Si/Al_2O_3/Si$ multi-layer structure, which has potential to bridge patterned devices or for nm-scale shadow lithography. Deposition conditions of controlled temperature and O_2 pressure were found for catalyst free ZnO growth on Al_2O_3 layer only (not on Si layer), which is critical for device integration. The 2-stage growth of small nanowires (~ 10 nm in diameter) starting from pattern edge first followed by a secondary growth of base on the existing wire is observed. This mechanism differs from previous reports (153, 154) of NWs having a similar structure of the tip and base segments. Kinetics study demonstrates that the growth of the NWs was controlled by surface diffusion of Zn/ZnO precursor on the thin alumina face at optimal O_2 pressure and growth temperature.

6.2 Experimental details

Patterned multilayer structures were deposited by sputtering and ZnO nanowires were grown by the chemical vapor deposition (CVD) in a 2-zone tube furnace with Zn metal source. The fabrication process is shown schematically in Figure 6.1. Prior to sample preparation, the Si wafer (Silicon Quest International, Inc.) was sequentially cleaned with acetone, isopropyl alcohol (IPA), deionized (DI) water and nitrogen drying. Into a photoresist window (10 μm × 10 μm or 60 μm × 60 μm), a multilayer of 20 nm of Si, 10 nm of Al_2O_3 and 20 nm of Si were sputtered, respectively, using an AJA International ATC 2000 sputtering system with a base pressure of 2×10^{-7} torr. Lift-off process was carried out to result in square patterns of Si 20 nm/$Al_2O_3$10 nm/Si 20 nm multilayer structures on Si wafer. The resulting 10nm thick alumina line at the pattern edge acts as the ZnO NW growth site as diagrammed in Figure 1 and is used to minimize the resulting ZnO NW diameter.

The growth of ZnO nanowires was performed in a quartz tube furnace (2.5cm i.d.) by exposing patterned wafers to Zn vapor and O_2 flow at 700˚C with a similar procedure as Ref.(130) (see Figure 6.2). Zn vapor pressure of ~ 5 torr, as measured by weight loss and carrier gas volume (the detailed calculation in section 6.3), was generated by heating Zinc powder (Purified, Mallinckrodt Baker LLC) to 600˚C. Patterned wafers were placed 8-10 cm downstream from the Zn source. At ambient pressure, a flow of 130±2 sccm of Ar (99.9%, Scott-Gross Co., INC) was used as the carrier gas when the heater was turned on. A separate O_2 inlet (6 mm o.d.) was placed 2cm upstream from sample to prevent oxidation of Zn source. When the temperature of Si wafer reached 700˚C, a flow of 1.0±0.03 sccm O_2 (99.98%, Linde Gas LLC) was introduced to form ZnO NW. Both gas flows were controlled by the MKS Instruments 1179A flow controllers and great care was taken to purge the chamber with an Ar flow to keep the metallic Zn source from being oxidized during heating.

Scanning electron microscopy (SEM) images were characterized by Hitachi S900 with field emission tip for nm-resolution and Hitachi S3200 equipped with high energy dispersive spectroscopy (EDS). High resolution transmission electron microscopy (HRTEM) images were recorded by JEOL F2010 operated at 200 keV. Preparation of TEM samples for ZnO NWs at the pattern edge required two steps as shown in Figure 6.1(c) & (d). First, Si/Al_2O_3/Si patterns were deposited on the Si/Si_3N_4 50 nm wafer and ZnO NWs were growing using the same condition described above. Then, the backside of Si wafer was dimpled mechanically by the Gatan 656 dimple grinder and the residual Si was removed by a mixed acid ($3HNO_3$:1HF:1HAc, volume ratio) to realize an electron transparent Si_3N_4 window under the patterned area.

6.3 Results and discussion

The optical image of Si/Al_2O_3/Si multilayer patterns is shown in Figure 6.3(a). SEM shows that many ZnO NWs grow laterally from the pattern edge in Figure 6.3(b), which is promising for shadow lithography (101) or integration between electrodes. Each NW is composed of a tip segment with a diameter ~ 10 nm and a base segment with a diameter ~ 22 nm in Figure 6.3(c). Previously, similar microstructures with larger diameter were reported in vertical growth processes (145, 153, 154). To prove that ZnO NWs were formed at pattern edges, a TEM study was employed. Sample preparation required making an electron transparent Si_3N_4 window underneath the patterned multilayer areas as diagrammed in Figure 6.1. Figure 6.4(a) shows a TEM image of a ZnO NW and the selected area electron diffraction pattern (SAED) inserted indicates a single crystalline phase. The high-resolution TEM image in Figure 6.4(b) shows a spacing of 2.55±0.07 Å between adjacent lattice planes corresponding to the distance between two (0002) crystal planes, confirming [0001] as the preferred growth direction (*c*- axis) for ZnO NWs.

It is important to note that ZnO growth under these conditions was seen to come only from the pattern edge where the exposed Al_2O_3 layer resided and not on the Si layer, differing from reported horizontal growth of ZnO NWs from Si substrates under different growth conditions (149-152). Control experiments were applied to confirm that the selective growth was on Al_2O_3 and not defects at the Si pattern edge. Samples of sputtered Si patterns on Si wafer were fabricated and no wires were found growing along the edge of Si patterns (with native SiO_2 coating) in Figure 6.3(d). EDS analysis of those samples shows no Zn, indicating that no Zinc particles or Zinc silicide/silicate compounds form at the edge of Si patterns. The feed Zn source is at 600^{o}C and growth is at 700^{o}C, so it is not expected for elemental Zn to condense on the sample surface, but will need to react with oxygen to form a non-volatile surface species. The Al_2O_3 appears to act as a surface for this reaction while it does not occur on Si/SiO_2 or on the growing ZnO wires under these conditions. To test this hypothesis the exposed area of Al_2O_3 was doubled by producing a thicker Si/Al_2O_3 20 nm/Si multilayer structure followed by 30 min growth ZnO at the same conditions. The ZnO volume density, calculated from NWs along the pattern edge with a scale of 1 μm, is ~2.2×10^{-20} m^3, which nearly doubles the ZnO volume density ~ 1.0×10^{-20} m^3 of Si/$Al_2O_3$10 nm/Si samples in Figure 6.3(b). It is important to note that the initial/tip diameter of ZnO NWs remained 10nm and was not set by the thickness of the catalytic layer (20nm) as had been seen in CNT growth (127).

The CVD growth conditions are critical for the morphology control of ZnO NWs. Zn vapor pressure of ~ 5 torr is calculated by weight loss of Zn powder and carrier gas volume. In Figure 6.2, Zn source was first heated to 600 ˚C very quickly by heater 1. The sample was heated to 700˚C by heater 2. Pure Ar gas was filled in the chamber to prevent the chemical reaction of Zn source with O_2. Then, an O_2 flow was introduced to the chamber for ZnO NWs growth. The time gap from the start of heart 1 to the O_2 flow is about 16 min. The experiment of 5 min reaction is used as an example for Zn vapor pressure calculation.

The total weight loss of Zn powder is 16.4 mg. The weight loss of Zn powder per second: 16.4 mg / ((16 min + 5min) × 60 s/min) = 1.3 × 10^{-5} g/s. Therefore, the Zn amount loss rate: n = (1.3 × 10^{-5} g/s) / (65 g/mol) = 2.0 × 10^{-7} mol/s. The carrier gas volume: V = 130 sccm = 2.17 × 10^{-6} m^3/s. The temperature of ZnO source is 873 K. Therefore,

$$P = \frac{nRT}{V} = \frac{2.0\times10^{-7} g\cdot s^{-1} \times 8.31\ J\cdot mol^{-1}\cdot K^{-1}\times 873\ K}{2.17\times10^{-6}\ m^3\cdot s^{-1}} = 668\ Pa\ \approx 5\ Torr \qquad (6.1)$$

The O_2 partial pressure with a flow rate of 1 sccm is (1 sccm/ 130 sccm) × 760 Torr ≈ 5.8 Torr.

Experiment results show that the tip and base segments dominate NWs' structure when a sufficient O_2 is supplied (~ 5.8 torr partial pressure at a flow rate ~ 1 sccm). No growth of ZnO NWs was found when the O_2 flow was zero. A few conical-shaped NWs were found at the pattern edge with a low O_2 pressure of ~ 0.5 torr, as shown in Figure 6.3(e). When an excessive O_2 is provided, e.g., O_2 pressure ~50 torr, there is uncontrolled growth of ZnO and tetrapod-shaped NWs grow both on alumina and silicon as shown in Figure 6.3(f). Similar structures had been reported in O_2 rich concentration (130, 155-158) during ZnO growth. Reaction temperature is another parameter affecting the growth of ZnO NWs. At growth temperatures of 675°C, 700°C, 725°C and 800°C and reaction time of 10 min, NWs with a length of 469 ± 54 nm, 1118 ± 86 nm, 778 ± 135 nm and 244 ± 41 nm, respectively were obtained. Large ZnO particles appeared when samples were heated over 725°C consuming Zn/ZnO source and resulting in short ZnO NWs at 800°C.

To study the growth mechanism, a kinetic study with samples of different reaction times (0, 0.5, 1.25, 2.5, 5, 10 and 30 min) were prepared. All of the diameter and length data is calculated statistically by 30 NWs selected randomly in each sample. Figure 6.5(a) shows the diameter variation of the tip and base segments grown in 30 min. With constant diameters of tip and base at ~ 10 nm and 22 nm, respectively, Figure 6.5(b) shows a constant linear density of ZnO NWs on Al_2O_3 surface along the pattern edge with 8~10 per μm. The summary of diameter and length distributions of ZnO NWs at 30 min is shown in Figure 6.6. The diameters of tip and base are 10±1 nm and 22±2 nm, respectively, which are consistent with the data in Figure 6.5(a). The length of base (1244±175 nm) is one order longer than that of tip (120±20 nm) and dominates the total length of NWs. The small deviation of the diameter, length and density data in Figures 6.5 and 6.6 reveals a uniform growth of ZnO NWs along the exposed Al_2O_3 line between two Si layers, including a simultaneous nucleation and a similar growth rates for most ZnO NWs, allowing for a kinetic study at periodically interrupted times.

The length of ZnO NWs as a function of time is shown in Figure 6.7(a). Growth rate *vs* reaction time, Figure 6.7(b), is derived from the slope at each time in Figure 5.7(a). 10nm diameter ZnO NW growth is initially fast but increases slowly after a 5 min reaction of Zn and O_2. The NWs growth rate at 1.25 min, also being the growth rate of tip segments at that time, reaches maximum at 543 nm/min, which is close to that of those ZnO NWs having a surface-diffusion induced growth at 700°C (159, 160). After this moment, base segments start to grow and stop the fast growth of tip segments since the base segments consume most of the ZnO source material before it diffuses to the tip segments. The lack of tip growth also shows that negligible Zn/ZnO intermediate surface species is formed on the ZnO NW surface in these growth conditions but requires the

Al_2O_3 surface. If small, 10nm diameter, ZnO nanowires are required, then growth time should be limited to less than 5 minutes.

Growth of ZnO NWs has been typically explained by the vapor-liquid-solid (VLS) (161) and vapor-solid (VS) mechanisms (162). The ideal VLS growth rate can be calculated by equation (6.2) & (6.3)

$$J_N = \frac{P}{\sqrt{2\pi mkT}} \tag{6.2}$$

$$v = \frac{J_N * m}{\rho} \tag{6.3}$$

where J_N is the condensation rate (atoms/m^2s), v is the growth rate (m/s), $m = 1.38\times10^{-25}$ kg is the mass of ZnO molecule, $\rho = 5.606\times10^3$ kg/m^3 is the density of ZnO, $P = 700$ Pa (~ 5 torr) is the pressure of Zn vapor derived from the mass loss of Zn powder and carrier gas volume, $T = 973$ K is the reaction temperature and k = is Boltzmann constant. The ideal VLS growth rate is about 4.3×10^6 nm/min, which is almost four orders of magnitude larger than the maxim experimental growth rate of 543 nm/min in Figure 6.7(b). The small experimental growth rate and no indication of catalyst tips in the catalyst-free ZnO NWs illustrate a VS growth mechanism that is limited by formation of a surface ZnO intermediate and surface diffusion on Al_2O_3 surface to the ZnO NW growth site at the NW tip or front of basal regrowth.

Under these experimental conditions, the amount of Zn/ZnO material provided by Al_2O_3 layer should be constant for each NW. At the beginning of tip growth,

$$-D_{Al2O3}\cdot\frac{\partial C}{\partial x}\cdot d\cdot\delta=\frac{dl_{t1}}{dt}\cdot\frac{\left(\pi\cdot r_t^2\right)\rho}{M} \tag{6.4}$$

and at the beginning of base growth,

$$-D_{Al2O3}\cdot\frac{\partial C}{\partial x}\cdot d\cdot\delta=\frac{dl_b}{dt}\cdot\frac{\left(\pi\cdot r_b^2-\pi\cdot r_t^2\right)\rho}{M}+\frac{dl_{t2}}{dt}\cdot\frac{\left(\pi\cdot r_t^2\right)\cdot\rho}{M} \tag{6.5}$$

So the ratio of eqn (6.5)/(6.4) results in

$$\frac{dl_{t1}}{dt}=\frac{dl_b}{dt}\cdot\frac{r_b^2-r_t^2}{r_t^2}+\frac{dl_{t2}}{dt} \tag{6.6}$$

where C is the concentration of Zn/ZnO on Al_2O_3 surface, x is the direction along the Al_2O_3 surface pointing to the ZnO NW root (as shown by the arrow in the left schematic drawing of Figure 6.8a), d is the thickness of Al_2O_3 film, δ is the thickness of Zn/ZnO molecular layer, r_t and r_b are the diameter of tip and base segments and l_t and l_b are the length of tip and base segments, respectively. The diffusion constant of Zn/ZnO on Al_2O_3 surface is considered constant and defined as D_{Al2O3}. As illustrated in Figure 6.7(b), dl_{t1}/dt, the growth rate of tip segments before base growth, is 543 nm/min at 1.25 min; dl_{t2}/dt, the growth rate of tip segments after base growth, is 233 nm/min at 2.5 min; dl_b/dt, the growth rate of base segments, is 86 nm/min at 2.5 min. r_t and r_b are 10 nm and 22 nm, respectively. So the ratio of growth area of base segments to that of tip segments is $(22^2-10^2)/10^2 = 3.8$, and

$$\frac{dl_b}{dt}\cdot\frac{r_b^2-r_t^2}{r_t^2}+\frac{dl_{t2}}{dt}=86nm/\min\times3.8+233nm/\min\ =560nm/\min$$

which is close to the experimentally observed dl_{t1}/dt =543 nm/min. This observation confirms equation (6.6) and our hypothesis that Zn/ZnO material is provided by surface Zn/ZnO intermediates on the Al_2O_3 layer for both tip and base growth.

The proposed growth mechanism of ZnO NWs and corresponding SEM images are shown in Figure 6.8. At the beginning of the reaction, Zn/ZnO precursor is formed only on the thin Al_2O_3 layer nucleating 10nm diameter ZnO NW growth. The Zn/ZnO intermediate formed on Al2O3 diffuses along the ZnO NW to the growth plane at the tip of NWs to support a continuous growth, as shown in Figure 6.8(b) at 0.5 min. At the start of the base segment growth, Zn/ZnO source is consumed at the base surface (Figure 6.8(e)), which stops a further growth of tip segments (5 min in Figure 6.8(c)). Since the ultimate length of the narrow nanowires is quite uniform, it is likely that at this critical length, the concentration at the base region reaches a nucleation point to do longer diffusion path along the wire length. Then, base segments continue to grow and cover the tip section, reducing the observed tip length as seen in Figure 6.8(d). Large crystals appear at root of NWs and consume most of the Zn/ZnO surface intermediate and cover the reactive Al_2O_3 area thus reducing ZnO NW growth rate. By 30 minutes, negligible nanowire growth is seen and the system appears to be self-limiting.

6.4 Conclusions

Lateral ZnO NWs have been successfully grown from the edge of Si/Al_2O_3/Si multi-layer structure. Small, 10 nm diameter, tip segments grow first followed by the growth of base segments (>20nm) which stops the narrow tip growth. Kinetic studies show that this two-step growth is diffusion limited and a constant Zn/ZnO flux originates from the thin exposed Al_2O_3 layer. This leads to a faster growth rate of the tip segment compared to base segment rate that is reciprocal to the ratio of their growth area. The selective growth of NWs on alumina, without any growth on silicon, is an important step in the integration of ZnO nanowires in patterned devices. These ZnO nanowires will be used as a shadow mask to form nm-scale gaps for the single molecular device fabrication in the future.

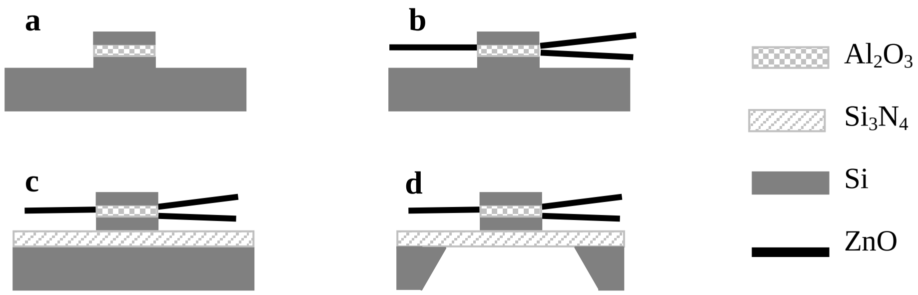

Figure 6.1. Schematic diagrams of ZnO nanowires grown from the edge of Si/Al$_2$O$_3$/Si multi-structure. (a) sputtered Si/Al$_2$O$_3$/Si multi-layer structure patterned by photolithography and liftoff, (b) ZnO nanowires growing selectively from the pattern edge, (c) growth of ZnO nanowires on Si/Si$_3$N$_4$ 50 nm substrate and (d) dimpling and etching of Si substrate to obtain the Si$_3$N$_4$ window TEM sample.

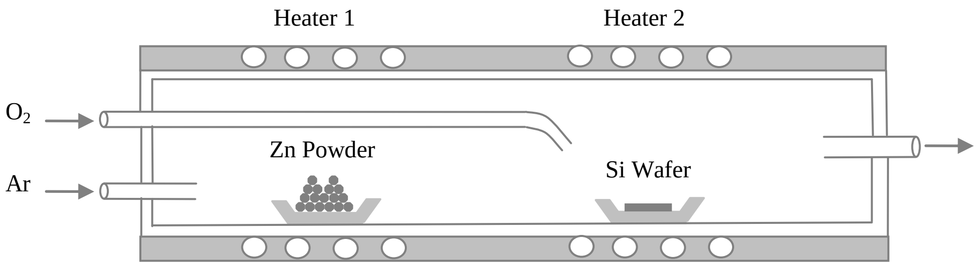

Figure 6.2. Schematic illustration of the CVD system used to grow ZnO nanowires.

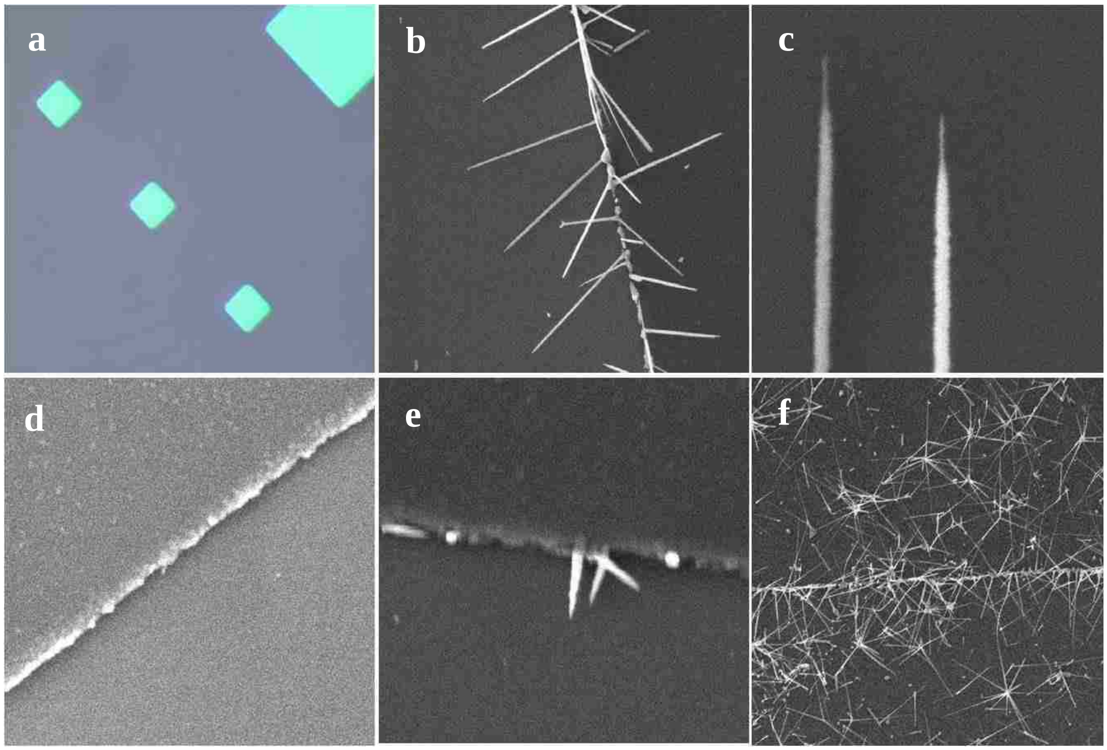

Figure 6.3. (a) The optical image for patterns of Si/Al_2O_3/Si multilayer structure and SEM images for (b) selective growth of ZnO nanowires along the edge of patterns with a reaction time of 30 min, (c) the tip segment and base segment, (d) Si patterns without Al2O3 layer after the same experimental process of (b), (e) low O_2 flow (0.1 sccm) and (f) high O_2 flow (> 10 sccm).

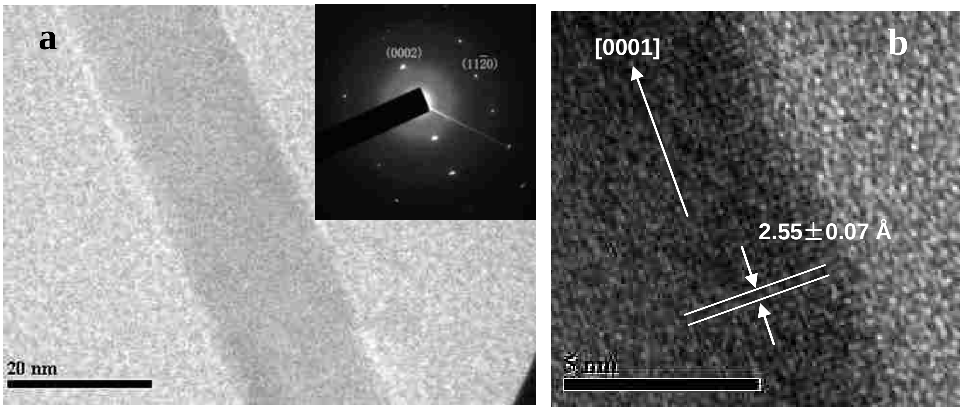

Figure 6.4. (a) TEM image and SAED pattern of a ZnO nanowire and (b) HRTEM image of single crystalline ZnO nanowire with lattice fringes.

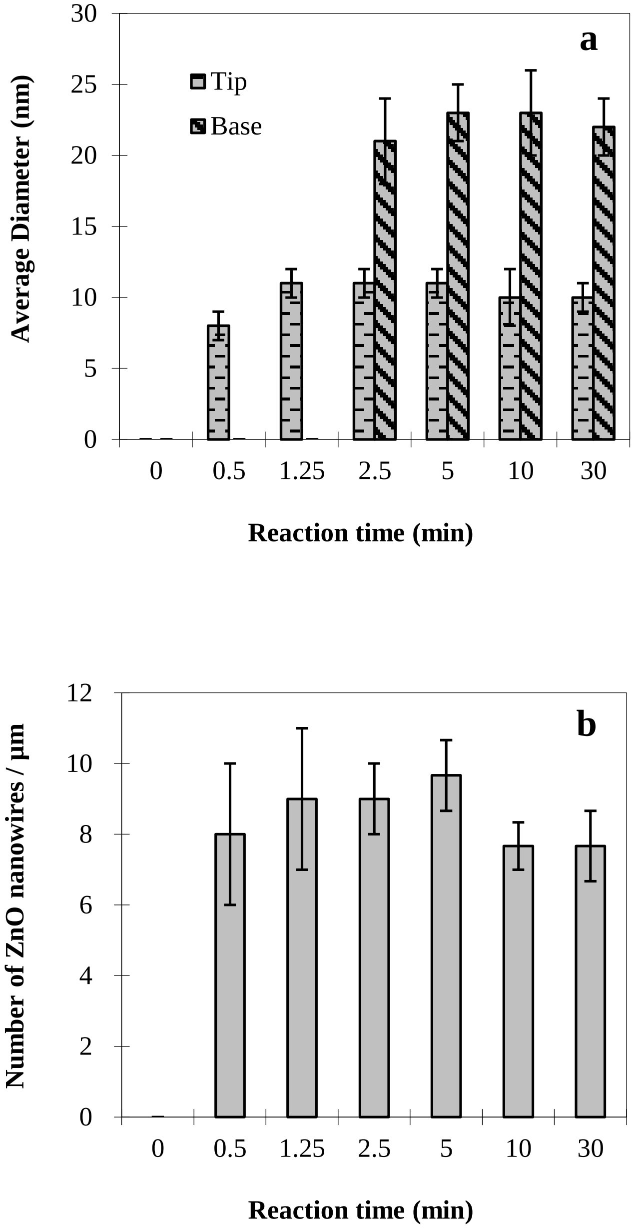

Figure 6.5. (a) diameter of tip and base segments (30 samples observed) and (b) nanowires density as a function of CVD growth time.

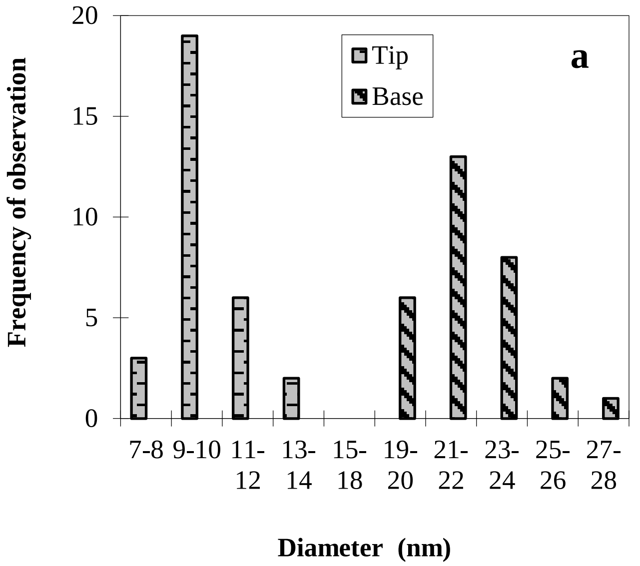

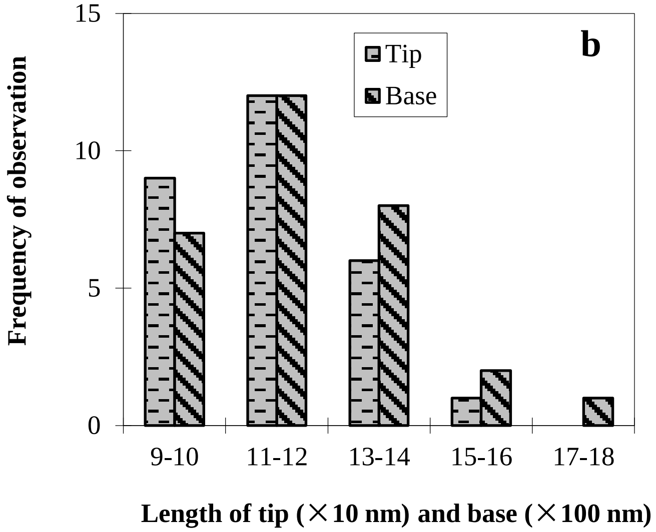

Figure 6.6. (a) diameter and (b) length distribution of tip and base segments with a reaction time of 30 min (30 samples observed for both charts).

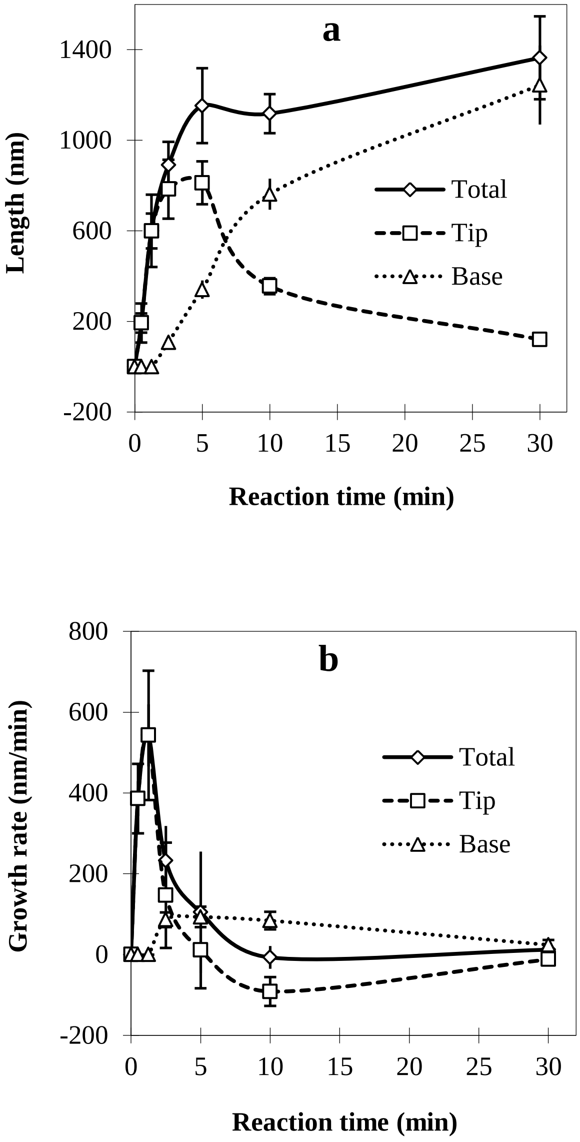

Figure 6.7. (a) length and (b) growth rate of ZnO nanowires during the growth process. The total length is a combination of the tip and base lengths.

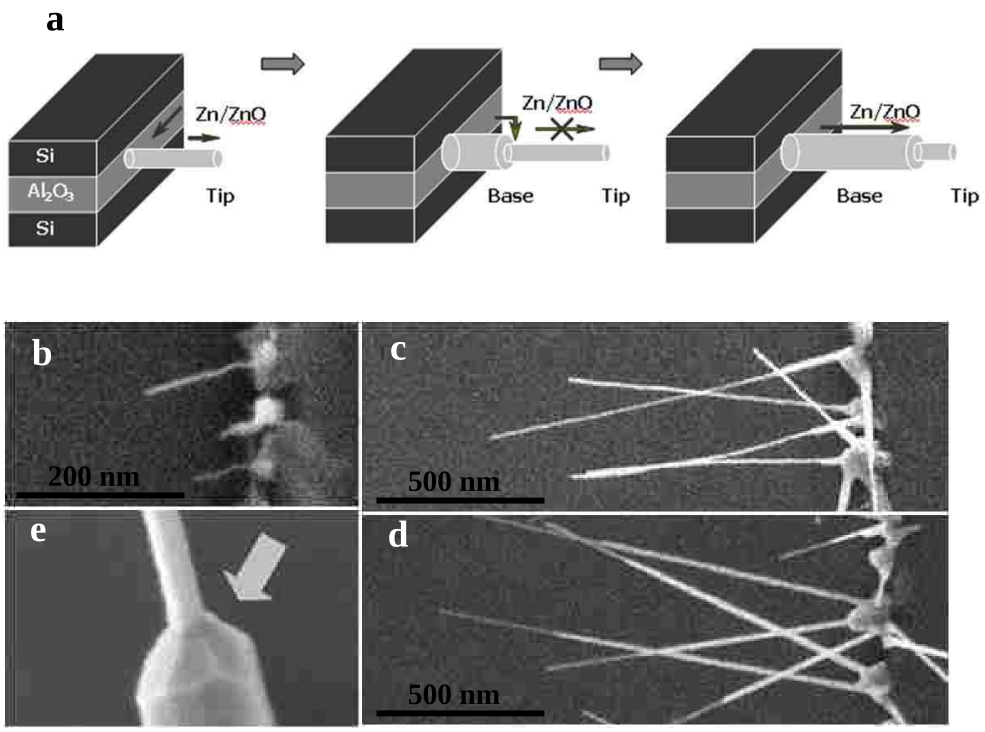

Figure 6.8. (a) Proposed growth mechanism of ZnO nanowires and SEM images of ZnO nanowires with a reaction time of (b) 0.5 min, (c) 5 min and (d) 10 min; (e) SEM image of the base surface.

Chapter 7

Conclusions and future work

7.1 Conclusions

7.1.1 Molecular devices based on Au/SAM/Al_2O_3/Au structures

Au tunnel junctions of Al/Au/SAM/Al_2O_3/Au structures were fabricated successfully by atomic layer deposition (ALD) of Al_2O_3 onto $HSCH_2CH_2OH$ self-assembled monolayer (SAM) on an Au bottom electrode. The ALD technique and $HSCH_2CH_2OH$ bonding layer were both first used to fabricate Au tunnel junctions. The -OH terminated SAM acts to grow a conformal monolayer of Al_2O_3 from trimethyl aluminum. The nano-gaps formed at the exposed edge of Au/SAM/Al_2O_3/Au structure can be as thin as 20 Å with a barrier height of ~ 1.2 eV, which makes them excellent candidates for molecular conduction studies. One to three orders of magnitude reduction in background tunnel current density were observed compared to related junctions enabling higher performance molecular junctions. Two different molecules were applied to bridge the nano-gap electrodes formed at the edge of Au/SAM/Al_2O_3/Au structures. Control experiments confirm the current passing through attached molecules. Low temperature study shows the molecular current generated by a tunneling mechanism.

7.1.2 Photovoltaic detector based on Au/Al_2O_3/Au structures

CuPc thin films were successfully deposited between Au electrodes with a gap distance smaller than the CuPc exciton diffusion length. The 10 nm-gap photocurrent of CuPc film is over 10 times larger than 20 nm-gap photocurrent and over 50 times larger than 100 nm-gap photocurrent. This large photocurrent enhancement is the result of the nano-gap's size being shorter than the CuPc exciton diffusion length thereby minimizing the recombination of electron-hole pairs. The large Schottky barrier contact resistance between the small area top Au electrode and the CuPc film is responsible for the diode *I-V* characteristics of devices in this work and is the primary limiter of efficiency.

7.1.3 Selective ZnO nanowire growth on Si/Al_2O_3/Si structures

Lateral ZnO NWs were successfully grown from the edge of Si/Al_2O_3/Si multi-layer structures. Small, 10 nm diameter, tip segments grow first followed by the growth of base segments (>20nm) which stops the narrow tip growth. Kinetic studies show that this two-step growth is diffusion limited and a constant Zn/ZnO flux originates from the thin exposed Al_2O_3 layer. This leads to a faster growth rate of the tip segment compared to base segment rate that is reciprocal to the ratio of their growth area. The selective growth of NWs on alumina, without any growth on silicon, is an important step in the integration of ZnO nanowires in patterned devices. These ZnO nanowires will be used as a shadow mask to form nm-scale gaps for the single molecular device fabrication in future.

7.2 Future work

7.2.1 Single molecular device

ZnO nanowire diameters are as small as 10 nm and are thus a very good candidate as the shadow mask to cast a nanoscale gap. Our group has generated nm-scale gaps in line-of-site depositions successfully by carbon nanotubes (CNTs) (101, 127, 128). Using the same technique, a 2 nm wide pattern can be casted on the edge of the Au/SAM/Al_2O_3/Au structure. Then, a single molecule can be electrically isolated in this shadow to bridge both Au electrodes, as shown in Figure 7.1.

7.2.2 Solar cells based on Metal I/Al_2O_3/Metal II multilayer structures

The Au/Al_2O_3/Au/Ti/TiO_2/CuPc device discussed in Chapter 5 is a photodetector. If the top Au electrode is replaced by an Aluminum electrode, this device becomes a solar cell, as seen in Figure 7.2. The Ti/TiO_2 cap layers are removed to increase the efficiency of the new Au 50 nm/Al_2O_3 10 nm/Al 20 nm/CuPc 70 nm photovoltaic device. The work function between Au (5.1~5.4 eV) and Al (4.1~4.3 eV) is about 1 eV. Therefore, the internal electric field generated by Au and Al electrodes is similar as the electric field generated by an applied voltage of 1 V. The photocurrent is ~ 13 nA at 1 V for Au 50 nm/Al_2O_3 10 nm/Al 20 nm/CuPc 70 nm sample in a incident light intensity of 15.8 mW/cm^2. Therefore, the generated photopower is 1.3×10^{-8} W. In Figure 5.2a, the distance between two top electrodes is 150 μm and the light power is 150 μm × 1000 μm × 15.8 mW/cm^2 = 2.4×10^{-5} W. Therefore, the photovoltaic efficiency of the solar cell should be only ~ 0.05%. But if the distance between two top electrodes decreases to 100 nm and the width of each top electrodes decrease to 50 nm, as shown in Figure 7.2, the photovoltaic efficiency of the new solar cells could reach 75%, which is much higher than the highest organic solar cell efficiency of ~ 7%. Although the calculation above is only a rough evaluation, it is still very promising to fabricate Au 50 nm/Al_2O_3 10 nm/Al 20 nm/CuPc 70 nm solar cells with a high power efficiency. The most challenges are protecting the top Al layer from oxidation before CuPc deposition and keeping all tunnel junctions working.

The small amount of active material between nano-gap electrodes will limit the absorption capacity. Several multilayers of Au/Al_2O_3/Al are built in Figure 7.3 to increase the absorption capacity. The large work function difference of ~ 1 eV between Au and Al can set up a high internal electric field reaching 10^8 V/m to separate electrons and holes effectively. And no ITO material is required. Considering these benefits, solar cells made of this new designed unit in Figure 8 is very promising.

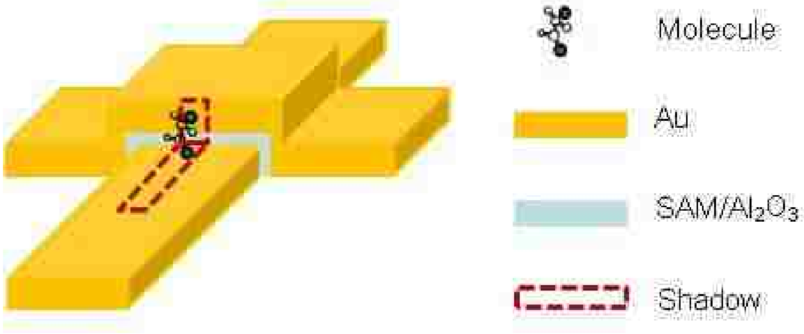

Figure 7.1. Schematic drawing of a single molecular device by a Au/SAM/Al_2O_3/Au structure.

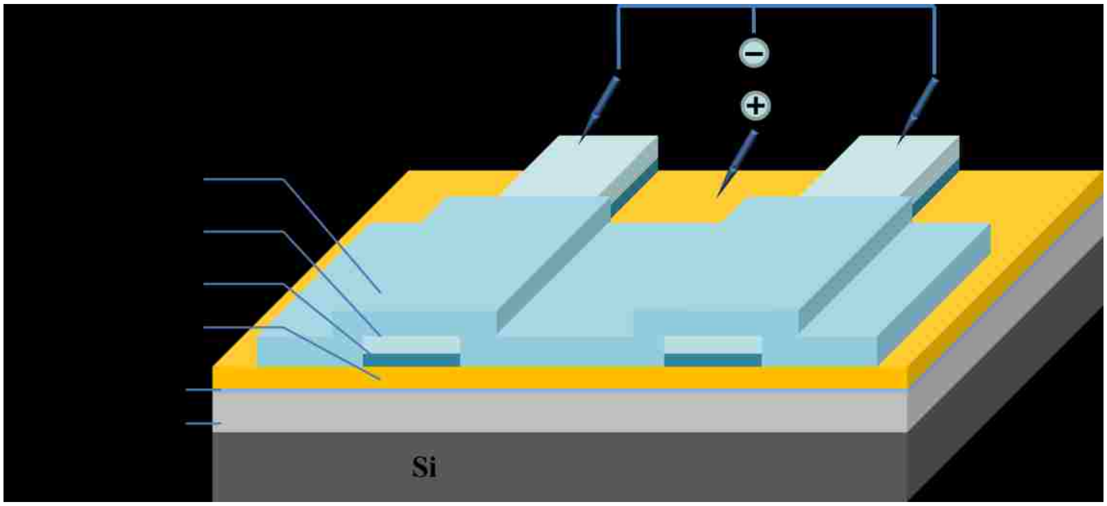

Figure 7.2. Schematic drawing of a solar cell of Au/Al_2O_3/Al/CuPc structures.

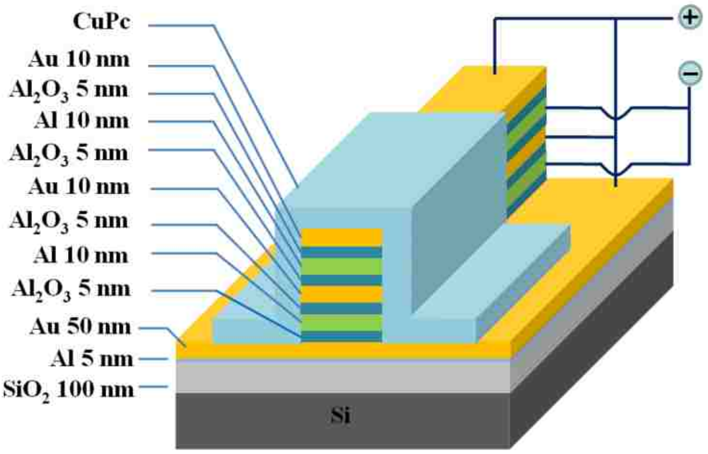

Figure 7.3. Schematic side view of the designed solar cell unit based on Au/Al_2O_3/Al multi-stacks.

References

1. S. O. Kasap, Principles of electronic materials and devices, McGraw-Hill, New York (2006).

2. T. R. Reid, The Chip: How Two Americans Invented the Microchip and Launched a Revolution, Simon and Schuster, New York (1984).

3. "From Intel official website http://www.intel.com/technology/mooreslaw/."

4. G.E.Moore, "Cramming More Components onto Integrated Circuits," Electronics 38(114-117 (1965)

5. D. A. Muller, T. Sorsch, S. Moccio, F. H. Baumann, K. Evans-Lutterodt and G. Timp, "The electronic structure at the atomic scale of ultrathin gate oxides," Nature 399(6738), 758-761 (1999)

6. S. Chiras and D. R. Clarke, "Dielectric cracking produced by electromigration in microelectronic interconnects," J Appl Phys 88(11), 6302-6312 (2000)

7. A. Aviram and M. A. Ratner, "Molecular Rectifiers," Chem Phys Lett 29(2), 277-283 (1974)

8. R. M. Metzger, B. Chen, U. Hopfner, M. V. Lakshmikantham, D. Vuillaume, T. Kawai, X. L. Wu, H. Tachibana, T. V. Hughes, H. Sakurai, J. W. Baldwin, C. Hosch, M. P. Cava, L. Brehmer and G. J. Ashwell, "Unimolecular electrical rectification in hexadecylquinolinium tricyanoquinodimethanide," J Am Chem Soc 119(43), 10455-10466 (1997)

9. C. Joachim and J. K. Gimzewski, "An electromechanical amplifier using a single molecule," Chem Phys Lett 265(3-5), 353-357 (1997)

10. S. Acharya, H. Song, J. Lee, P. S. Kwon, J. Lee, G. Yogendranath, Y. H. Kim, Y. H. Jang, T. Lee, S. Samal and J. Lee, "An amphiphilic C60 penta-addition derivative as a new U-type molecular rectifier," Organic Electronics 10(1), 85-94 (2009)

11. Y. Wada, "A prospect for single molecule information processing devices," Pure Appl Chem 71(11), 2055-2066 (1999)

12. Y. Wada, "Proposal of atom/molecule switching devices," J Vac Sci Technol A 17(4), 1399-1405 (1999)

13. F. Moresco, G. Meyer, K. H. Rieder, H. Tang, A. Gourdon and C. Joachim, "Conformational changes of single molecules induced by scanning tunneling microscopy manipulation: A route to molecular switching," Phys Rev Lett 86(4), 672-675 (2001)

14. Y. Wada, T. Uda, M. Lutwyche, S. Kondo and S. Heike, "A Proposal of Nanoscale Devices Based on Atom Molecule Switching," J Appl Phys 74(12), 7321-7328 (1993)

15. S. J. Tans, A. R. M. Verschueren and C. Dekker, "Room-temperature transistor based on a single carbon nanotube," Nature 393(6680), 49-52 (1998)

16. T. Sato, H. Ahmed, D. Brown and B. F. G. Johnson, "Single electron transistor using a molecularly linked gold colloidal particle chain," J Appl Phys 82(2), 696-701 (1997)

17. R. P. Andres, T. Bein, M. Dorogi, S. Feng, J. I. Henderson, C. P. Kubiak, W. Mahoney, R. G. Osifchin and R. Reifenberger, ""Coulomb staircase" at room temperature in a self-assembled molecular nanostructure," Science 272(5266), 1323-1325 (1996)

18. R. P. Andres, S. Datta, M. Dorogi, J. Gomez, J. I. Henderson, D. B. Janes, V. R. Kolagunta, C. P. Kubiak, W. Mahoney, R. F. Osifchin, R. Reifenberger, M. P. Samanta and W. Tian, "Room temperature Coulomb blockade and Coulomb staircase from self-assembled nanostructures," Journal of Vacuum Science & Technology a-Vacuum Surfaces and Films 14(3), 1178-1183 (1996)
19. C. Zhang, M. H. Du, H. P. Cheng, X. G. Zhang, A. E. Roitberg and J. L. Krause, "Coherent electron transport through an azobenzene molecule: A light-driven molecular switch," Phys Rev Lett 92(15), - (2004)
20. J. L. Palma, C. Cao, X. G. Zhang, P. S. Krstic, J. L. Krause and H. P. Cheng, "Manipulating I-V Characteristics of a Molecular Switch with Chemical Modifications," J Phys Chem C 114(3), 1655-1662 (2010)
21. C. Dohno, S. N. Uno and K. Nakatani, "Photoswitchable molecular glue for DNA," J Am Chem Soc 129(39), 11898-+ (2007)
22. P. Gorostiza, M. Volgraf, R. Numano, S. Szobota, D. Trauner and E. Y. Isacoff, "Mechanisms of photoswitch conjugation and light activation of an ionotropic glutamate receptor," P Natl Acad Sci USA 104(26), 10865-10870 (2007)
23. A. Aviram, "Molecules for Memory, Logic, and Amplification," J Am Chem Soc 110(17), 5687-5692 (1988)
24. M. S. Doescher, J. M. Tour, A. M. Rawlett and M. L. Myrick, "Stripping voltammetry of Cu overlayers deposited on self-assembled monolayers: Field emission of electrons through a phenylene ethynylene oligomer," J Phys Chem B 105(1), 105-110 (2001)
25. M. T. Cygan, T. D. Dunbar, J. J. Arnold, L. A. Bumm, N. F. Shedlock, T. P. Burgin, L. Jones, D. L. Allara, J. M. Tour and P. S. Weiss, "Insertion, conductivity, and structures of conjugated organic oligomers in self-assembled alkanethiol monolayers on Au{111}," J Am Chem Soc 120(12), 2721-2732 (1998)
26. L. A. Bumm, J. J. Arnold, M. T. Cygan, T. D. Dunbar, T. P. Burgin, L. Jones, D. L. Allara, J. M. Tour and P. S. Weiss, "Are single molecular wires conducting?," Science 271(5256), 1705-1707 (1996)
27. R. Dembinski, T. Bartik, B. Bartik, M. Jaeger and J. A. Gladysz, "Toward metal-capped one-dimensional carbon allotropes: Wirelike C-6-C-20 polyynediyl chains that span two redox-active (eta(5)-C5Me5)Re(NO)(PPh3) endgroups," J Am Chem Soc 122(5), 810-822 (2000)
28. M. J. Crossley and P. L. Burn, "An Approach to Porphyrin-Based Molecular Wires - Synthesis of a Bis(Porphyrin)Tetraone and Its Conversion to a Linearly Conjugated Tetrakisporphyrin System," J Chem Soc Chem Comm 21), 1569-1571 (1991)
29. D. L. Pearson and J. M. Tour, "Rapid syntheses of oligo(2,5-thiophene ethynylene)s with thioester termini: Potential molecular scale wires with alligator clips," J Org Chem 62(5), 1376-1387 (1997)
30. L. Jones, J. S. Schumm and J. M. Tour, "Rapid solution and solid phase syntheses of oligo(1,4-phenylene ethynylene)s with thioester termini: Molecular scale wires with alligator clips. Derivation of iterative reaction efficiencies on a polymer support," J Org Chem 62(5), 1388-1410 (1997)
31. J. R. Reimers, L. E. Hall, M. J. Crossley and N. S. Hush, "Rigid fused oligoporphyrins as potential versatile molecular wires. 2. B3LYP and SCF calculated

geometric and electronic properties of 98 oligoporphyrin and related molecules," J Phys Chem A 103(22), 4385-4397 (1999)

32. J. W. G. Wildoer, L. C. Venema, A. G. Rinzler, R. E. Smalley and C. Dekker, "Electronic structure of atomically resolved carbon nanotubes," Nature 391(6662), 59-62 (1998)

33. T. W. Odom, J. L. Huang, P. Kim and C. M. Lieber, "Atomic structure and electronic properties of single-walled carbon nanotubes," Nature 391(6662), 62-64 (1998)

34. P. J. de Pablo, C. Gomez-Navarro, A. Gil, J. Colchero, M. T. Martinez, A. M. Benito, W. K. Maser, J. Gomez-Herrero and A. M. Baro, "Visualization of single-walled carbon nanotubes electrical networks by scanning force microspy," Appl Phys Lett 79(18), 2979-2981 (2001)

35. T. Rueckes, K. Kim, E. Joselevich, G. Y. Tseng, C. L. Cheung and C. M. Lieber, "Carbon nanotube-based nonvolatile random access memory for molecular computing," Science 289(5476), 94-97 (2000)

36. B. J. Hinds, N. Chopra, T. Rantell, R. Andrews, V. Gavalas and L. G. Bachas, "Aligned multiwalled carbon nanotube membranes," Science 303(5654), 62-65 (2004)

37. M. Majumder, N. Chopra, R. Andrews and B. J. Hinds, "Nanoscale hydrodynamics: Enhanced flow in carbon nanotubes (vol 438, pg 44, 2005)," Nature 438(7070), 930-930 (2005)

38. M. Majumder, N. Chopra and B. J. Hinds, "Effect of tip functionalization on transport through vertically oriented carbon nanotube membranes," J Am Chem Soc 127(25), 9062-9070 (2005)

39. J. Wu, K. S. Paudel, C. Strasinger, D. Hammell, A. L. Stinchcomb and B. J. Hinds, "Programmable transdermal drug delivery of nicotine using carbon nanotube membranes," P Natl Acad Sci USA 107(26), 11698-11702 (2010)

40. N. J. Geddes, J. R. Sambles, D. J. Jarvis, W. G. Parker and D. J. Sandman, "Fabrication and Investigation of Asymmetric Current-Voltage Characteristics of a Metal Langmuir-Blodgett Monolayer Metal Structure," Appl Phys Lett 56(19), 1916-1918 (1990)

41. C. M. Fischer, M. Burghard, S. Roth and K. Vonklitzing, "Microstructured Gold Langmuir-Blodgett-Film Gold Tunneling Junctions," Appl Phys Lett 66(24), 3331-3333 (1995)

42. C. P. Collier, E. W. Wong, M. Belohradsky, F. M. Raymo, J. F. Stoddart, P. J. Kuekes, R. S. Williams and J. R. Heath, "Electronically configurable molecular-based logic gates," Science 285(5426), 391-394 (1999)

43. X. D. Cui, A. Primak, X. Zarate, J. Tomfohr, O. F. Sankey, A. L. Moore, T. A. Moore, D. Gust, G. Harris and S. M. Lindsay, "Reproducible measurement of single-molecule conductivity," Science 294(5542), 571-574 (2001)

44. X. D. Cui, A. Primak, X. Zarate, J. Tomfohr, O. F. Sankey, A. L. Moore, T. A. Moore, D. Gust, L. A. Nagahara and S. M. Lindsay, "Changes in the electronic properties of a molecule when it is wired into a circuit," J Phys Chem B 106(34), 8609-8614 (2002)

45. M. A. Rampi and G. M. Whitesides, "A versatile experimental approach for understanding electron transport through organic materials," Chem Phys 281(2-3), 373-391 (2002)

46. J. G. Kushmerick, D. B. Holt, J. C. Yang, J. Naciri, M. H. Moore and R. Shashidhar, "Metal-molecule contacts and charge transport across monomolecular layers: Measurement and theory," Phys Rev Lett 89(8), - (2002)
47. C. Zhou, M. R. Deshpande, M. A. Reed, L. Jonesll and J. M. Tour, "Nanoscale metal self-assembled monolayer metal heterostructures (vol 71, pg 611, 1997)," Appl Phys Lett 71(19), 2857-2857 (1997)
48. H. B. Akkerman, P. W. M. Blom, D. M. de Leeuw and B. de Boer, "Towards molecular electronics with large-area molecular junctions," Nature 441(7089), 69-72 (2006)
49. E. Delamarche, B. Michel, H. A. Biebuyck and C. Gerber, "Golden interfaces: The surface of self-assembled monolayers," Adv Mater 8(9), 719-& (1996)
50. G. V. Nazin, X. H. Qiu and W. Ho, "Visualization and spectroscopy of a metal-molecule-metal bridge," Science 302(5642), 77-81 (2003)
51. M. A. Reed, C. Zhou, C. J. Muller, T. P. Burgin and J. M. Tour, "Conductance of a molecular junction," Science 278(5336), 252-254 (1997)
52. J. J. Parks, A. R. Champagne, G. R. Hutchison, S. Flores-Torres, H. D. Abruna and D. C. Ralph, "Tuning the kondo effect with a mechanically controllable break junction," Phys Rev Lett 99(2), - (2007)
53. J. Park, A. N. Pasupathy, J. I. Goldsmith, C. Chang, Y. Yaish, J. R. Petta, M. Rinkoski, J. P. Sethna, H. D. Abruna, P. L. McEuen and D. C. Ralph, "Coulomb blockade and the Kondo effect in single-atom transistors," Nature 417(6890), 722-725 (2002)
54. W. J. Liang, M. P. Shores, M. Bockrath, J. R. Long and H. Park, "Kondo resonance in a single-molecule transistor," Nature 417(6890), 725-729 (2002)
55. L. H. Yu and D. Natelson, "The Kondo effect in C-60 single-molecule transistors," Nano Lett 4(1), 79-83 (2004)
56. A. A. Houck, J. Labaziewicz, E. K. Chan, J. A. Folk and I. L. Chuang, "Kondo effect in electromigrated gold break junctions," Nano Lett 5(9), 1685-1688 (2005)
57. H. Yamaguchi, T. Terui, Y. Noguchi, R. Ueda, K. Nasu, A. Otomo and K. Matsuda, "A photoresponsive single electron transistor prepared from oligothiophene molecules and gold nanoparticles in a nanogap electrode," Appl Phys Lett 96(10), - (2010)
58. A. K. Mahapatro, J. W. Ying, T. Ren and D. B. Janes, "Electronic transport through ruthenium-based redox-active molecules in metal-molecule-metal nanogap junctions," Nano Lett 8(8), 2131-2136 (2008)
59. N. B. Zhitenev, H. Meng and Z. Bao, "Conductance of small molecular junctions," Phys Rev Lett 88(22), - (2002)
60. S. Kubatkin, A. Danilov, M. Hjort, J. Cornil, J. L. Bredas, N. Stuhr-Hansen, P. Hedegard and T. Bjornholm, "Single-electron transistor of a single organic molecule with access to several redox states," Nature 425(6959), 698-701 (2003)
61. S. Datta, Electronic Transport in Mesoscopic System, Cambridge University Press, Cambridge (2001).
62. H. B. Akkerman and B. de Boer, "Electrical conduction through single molecules and self-assembled monolayers," J Phys-Condens Mat 20(1), - (2008)
63. A. Salomon, D. Cahen, S. Lindsay, J. Tomfohr, V. B. Engelkes and C. D. Frisbie, "Comparison of electronic transport measurements on organic molecules," Adv Mater 15(22), 1881-1890 (2003)

64. K. Slowinski, R. V. Chamberlain, C. J. Miller and M. Majda, "Through-bond and chain-to-chain coupling. Two pathways in electron tunneling through liquid alkanethiol monolayers on mercury electrodes," J Am Chem Soc 119(49), 11910-11919 (1997)

65. J. G. Kushmerick, D. B. Holt, S. K. Pollack, M. A. Ratner, J. C. Yang, T. L. Schull, J. Naciri, M. H. Moore and R. Shashidhar, "Effect of bond-length alternation in molecular wires," J Am Chem Soc 124(36), 10654-10655 (2002)

66. J. G. Simmons, "Generalized Formula for Electric Tunnel Effect between Similar Electrodes Separated by a Thin Insulating Film," J Appl Phys 34(6), 1793-& (1963)

67. D. Bohm, Quantum Theory, Prentice-Hall, Inc., Englewood Cliffs, New Jersey (1951).

68. J. G. Zhu and C. Park, "Magnetic Tunnel Junctions," Materials Today 9(36-45 (2006)

69. G. W. Hanson, Fundamentals of Nanoelectronics, Pearson Prentice Hall, Upper Saddle River, NJ (2008).

70. R. Wilkins, E. Benjacob and R. C. Jaklevic, "Scanning-Tunneling-Microscope Observations of Coulomb Blockade and Oxide Polarization in Small Metal Droplets," Phys Rev Lett 63(7), 801-804 (1989)

71. R. Negishi, T. Hasegawa, K. Terabe, M. Aono, H. Tanaka, T. Ogawa and H. Ozawa, "I-V characteristics of single electron tunneling from symmetric and asymmetric double-barrier tunneling junctions," Appl Phys Lett 90(22), - (2007)

72. Y. Wakayama, T. Kubota, H. Suzuki, T. Kamikado and S. Mashiko, "Optical controllability of single-electron tunnelling through a molecular Coulomb island in a MOS structure," Nanotechnology 15(11), 1446-1449 (2004)

73. Y. Wakayama, K. Ogawa, T. Kubota, H. Suzuki, T. Kamikado and S. Mashiko, "Optical switching of single-electron tunneling in SiO2/molecule/SiO2 multilayer on Si(100)," Appl Phys Lett 85(2), 329-331 (2004)

74. A. Danilov, S. Kubatkin, S. Kafanov, P. Hedegard, N. Stuhr-Hansen, K. Moth-Poulsen and T. Bjornholm, "Electronic transport in single molecule junctions: Control of the molecule-electrode coupling through intramolecular tunneling barriers," Nano Lett 8(1), 1-5 (2008)

75. P. Peumans, A. Yakimov and S. R. Forrest, "Small molecular weight organic thin-film photodetectors and solar cells (vol 93, pg 3693, 2003)," J Appl Phys 95(5), 2938-2938 (2004)

76. H. Hoppe and N. S. Sariciftci, "Organic solar cells: An overview," J Mater Res 19(7), 1924-1945 (2004)

77. A. R. Murphy and J. M. J. Frechet, "Organic semiconducting oligomers for use in thin film transistors," Chem Rev 107(4), 1066-1096 (2007)

78. J. Zaumseil and H. Sirringhaus, "Electron and ambipolar transport in organic field-effect transistors," Chem Rev 107(4), 1296-1323 (2007)

79. C. W. Tang, "Two-layer organic photovoltaic cell," Appl Phys Lett 48(2), 183-185 (1986)

80. S. Banerjee, A. P. Parhi, S. S. K. Iyer and S. Kumar, "Method of determining the exciton diffusion length using optical interference effect in Schottky diode," Appl Phys Lett 94(22), - (2009)

81. H. Hansel, H. Zettl, G. Krausch, R. Kisselev, M. Thelakkat and H. W. Schmidt, "Optical and electronic contributions in double-heterojunction organic thin-film solar cells," Adv Mater 15(24), 2056-+ (2003)
82. P. E. Shaw, A. Ruseckas and I. D. W. Samuel, "Exciton diffusion measurements in poly(3-hexylthiophene)," Adv Mater 20(18), 3516-+ (2008)
83. G. Yu, J. Gao, J. C. Hummelen, F. Wudl and A. J. Heeger, "Polymer Photovoltaic Cells - Enhanced Efficiencies Via a Network of Internal Donor-Acceptor Heterojunctions," Science 270(5243), 1789-1791 (1995)
84. J. J. M. Halls, C. A. Walsh, N. C. Greenham, E. A. Marseglia, R. H. Friend, S. C. Moratti and A. B. Holmes, "Efficient Photodiodes from Interpenetrating Polymer Networks," Nature 376(6540), 498-500 (1995)
85. J. G. Xue, S. Uchida, B. P. Rand and S. R. Forrest, "Asymmetric tandem organic photovoltaic cells with hybrid planar-mixed molecular heterojunctions," Appl Phys Lett 85(23), 5757-5759 (2004)
86. Y. Y. Liang, Z. Xu, J. B. Xia, S. T. Tsai, Y. Wu, G. Li, C. Ray and L. P. Yu, "For the Bright Future-Bulk Heterojunction Polymer Solar Cells with Power Conversion Efficiency of 7.4%," Adv Mater 22(20), E135-+ (2010)
87. F. Yang, M. Shtein and S. R. Forrest, "Controlled growth of a molecular bulk heterojunction photovoltaic cell," Nat Mater 4(1), 37-41 (2005)
88. F. Gutman and L. E. Lyons, Organic Semiconductors, Wiley & Sons, New York (1967).
89. G. A. Chamberlain, "Organic Solar-Cells - a Review," Sol Cells 8(1), 47-83 (1983)
90. M. Hiramoto, Y. Kishigami and M. Yokoyama, "Doping Effect on the 2-Layer Organic Solar-Cell," Chem Lett 1), 119-122 (1990)
91. P. A. Lane, J. Rostalski, C. Giebeler, S. J. Martin, D. D. C. Bradley and D. Meissner, "Electroabsorption studies of phthalocyanine/perylene solar cells," Sol Energ Mat Sol C 63(1), 3-13 (2000)
92. I. Hiromitsu, Y. Murakami and T. Ito, "Electric field in phthalocyanine/perylene heterojunction solar cells studied by electroabsorption and photocurrent measurements," J Appl Phys 94(4), 2434-2439 (2003)
93. J. Rostalski and D. Meissner, "Photocurrent spectroscopy for the investigation of charge carrier generation and transport mechanisms in organic p/n-junction solar cells," Sol Energ Mat Sol C 63(1), 37-47 (2000)
94. N. S. Sariciftci, L. Smilowitz, A. J. Heeger and F. Wudl, "Photoinduced Electron-Transfer from a Conducting Polymer to Buckminsterfullerene," Science 258(5087), 1474-1476 (1992)
95. C. J. Ko, Y. K. Lin, F. C. Chen and C. W. Chu, "Modified buffer layers for polymer photovoltaic devices," Appl Phys Lett 90(6), - (2007)
96. G. Li, V. Shrotriya, J. S. Huang, Y. Yao, T. Moriarty, K. Emery and Y. Yang, "High-efficiency solution processable polymer photovoltaic cells by self-organization of polymer blends," Nat Mater 4(11), 864-868 (2005)
97. W. L. Ma, C. Y. Yang, X. Gong, K. Lee and A. J. Heeger, "Thermally stable, efficient polymer solar cells with nanoscale control of the interpenetrating network morphology," Adv Funct Mater 15(10), 1617-1622 (2005)

98. M. Reyes-Reyes, K. Kim and D. L. Carroll, "High-efficiency photovoltaic devices based on annealed poly(3-hexylthiophene) and 1-(3-methoxycarbonyl)-propyl-1-phenyl-(6,6)C-61 blends," Appl Phys Lett 87(8), - (2005)

99. M. Reyes-Reyes, K. Kim, J. Dewald, R. Lopez-Sandoval, A. Avadhanula, S. Curran and D. L. Carroll, "Meso-structure formation for enhanced organic photovoltaic cells," Org Lett 7(26), 5749-5752 (2005)

100. P. Tyagi, D. F. Li, S. M. Holmes and B. J. Hinds, "Molecular electrodes at the exposed edge of metal/insulator/metal trilayer structures," J Am Chem Soc 129(16), 4929-4938 (2007)

101. N. Chopra, W. T. Xu, L. E. De Long and B. J. Hinds, "Incident angle dependence of nanogap size in suspended carbon nanotube shadow lithography," Nanotechnology 16(1), 133-136 (2005)

102. W. F. Brinkman, R. C. Dynes and J. M. Rowell, "Tunneling Conductance of Asymmetrical Barriers," J Appl Phys 41(5), 1915-& (1970)

103. S. A. Campbell, The Science and Engineering of Microelectronic Fabrication, Oxford University Press, Inc., New York (2001).

104. D. M. Jeon, J. W. Park, D. H. Lee, S. Y. Yoon, D. H. Yoon and S. J. Suh, "Annealing effect on the barrier properties and TMR of magnetic tunneling junctions fabricated in various oxidation conditions," J Magn Magn Mater 272-76(1956-1958 (2004)

105. D. F. Li, S. Parkin, G. B. Wang, G. T. Yee, R. Clerac, W. Wernsdorfer and S. M. Holmes, "An S=6 cyanide-bridged octanuclear (Fe4Ni4II)-Ni-III complex that exhibits slow relaxation of the magnetization," J Am Chem Soc 128(13), 4214-4215 (2006)

106. C. E. Inman, S. M. Reed and J. E. Hutchison, "In situ deprotection and assembly of S-tritylalkanethiols on gold yields monolayers comparable to those prepared directly from alkanethiols," Langmuir 20(21), 9144-9150 (2004)

107. A. K. Mahapatro, S. Ghosh and D. B. Janes, "Nanometer scale electrode separation (nanogap) using electromigration at room temperature," Ieee T Nanotechnol 5(3), 232-236 (2006)

108. C. Joachim, J. K. Gimzewski, R. R. Schlittler and C. Chavy, "Electronic transparence of a single C60 molecule," Phys Rev Lett 74(11), 2102-2105 (1995)

109. M. Hyun and C. K. Rhee, "STM study of 2-mercaptoethanol self-assembled monolayer on Au(111)," B Kor Chem Soc 22(2), 213-218 (2001)

110. W. Chen, X. Q. Liu, Z. K. Tan, K. K. Likharev, J. E. Lukens and A. Mayr, "Fabrication and characterization of novel cross point structures for molecular electronic integrated circuits," J Vac Sci Technol B 24(6), 3217-3220 (2006)

111. G. J. Ashwell, P. Wierzchowiec, C. J. Bartlett and P. D. Buckle, "Molecular electronics: connection across nano-sized electrode gaps," Chem Commun 12), 1254-1256 (2007)

112. P. Tyagi, D. Li, S.M. Holmes and B. J. Hinds, "Insulator Film Thickness to Fix the Spacing between Electrodes to Molecular Length Scale," in Proceedings of the 2nd IEEE International Conference on Nano/Micro Engineered and Molecular Systems, pp. 191-194, Bangkok, Thailand (2007).

113. P. Tyagi and B. J. Hinds, "Mechanism of ultrathin tunnel barrier failure due to mechanical-stress-induced nanosized hillocks and voids," J Vac Sci Technol B 28(3), 517-521 (2010)

114. A. K. Mahapatro, A. Scott, A. Manning and D. B. Janes, "Gold surface with sub-nm roughness realized by evaporation on a molecular adhesion monolayer," Appl Phys Lett 88(15), - (2006)
115. J. S. Moodera, R. Meservey and P. M. Tedrow, "Artificial Tunnel Barriers Produced by Cryogenically Deposited Al2o3," Appl Phys Lett 41(5), 488-490 (1982)
116. H. C. Lin, P. D. Ye and G. D. Wilk, "Leakage current and breakdown electric-field studies on ultrathin atomic-layer-deposited Al2O3 on GaAs," Appl Phys Lett 87(18), - (2005)
117. M. D. Groner, J. W. Elam, F. H. Fabreguette and S. M. George, "Electrical characterization of thin Al2O3 films grown by atomic layer deposition on silicon and various metal substrates," Thin Solid Films 413(1-2), 186-197 (2002)
118. A. S. Ichimura, W. Lew and D. L. Allara, "Tripod self-assembled monolayer on Au(111) prepared by reaction of hydroxyl-terminated alkylthiols with SiCl4," Langmuir 24(6), 2487-2493 (2008)
119. B. Hu, J. Y. Yao and B. J. Hinds, "Nanogap electrodes formed at the exposed edge of Au/self-assembled monolayer/Al2O3/Au tunnel structures grown by atomic layer deposition," Appl Phys Lett 97(20), - (2010)
120. B. Q. Xu and N. J. J. Tao, "Measurement of single-molecule resistance by repeated formation of molecular junctions," Science 301(5637), 1221-1223 (2003)
121. J. M. Beebe, V. B. Engelkes, L. L. Miller and C. D. Frisbie, "Contact resistance in metal-molecule-metal junctions based on aliphatic SAMs: Effects of surface linker and metal work function," J Am Chem Soc 124(38), 11268-11269 (2002)
122. B. Hu, J. Yao and B. J. Hinds, "Nano-gap electrodes formed at the exposed edge of Au/SAM/Al2O3/Au tunnel structures grown by atomic layer deposition," Appl Phys Lett in press (2010)
123. J. Simmons and J. J. Andre, Molecular Semiconductors, Springer Verlag, Berlin (1985).
124. S. Karan and B. Mallik, "Power spectral density analysis and photoconducting behavior in copper(II) phthalocyanine nanostructured thin films," Phys Chem Chem Phys 10(45), 6751-6761 (2008)
125. R. D. Gould, "Dc Electrical Measurements on Evaporated Thin-Films of Copper Phthalocyanine," Thin Solid Films 125(1-2), 63-69 (1985)
126. L. Kreja and W. Czerwinski, "A Study of Iodine Influence on the Electrical-Properties of Phthalocyanines and Polyphthalocyanines of Some Metals," J Mater Sci Lett 11(9), 538-540 (1992)
127. N. Chopra, P. D. Kichambare, R. Andrews and B. J. Hinds, "Control of multiwalled carbon nanotube diameter by selective growth on the exposed edge of a thin film multilayer structure," Nano Lett 2(10), 1177-1181 (2002)
128. J. Lefebvre, M. Radosavljevic and A. T. Johnson, "Fabrication of nanometer size gaps in a metallic wire," Appl Phys Lett 76(25), 3828-3830 (2000)
129. Z. L. Wang, "Zinc oxide nanostructures: growth, properties and applications," J Phys-Condens Mat 16(25), R829-R858 (2004)
130. J. Park, H. H. Choi, K. Siebein and R. K. Singh, "Two-step evaporation process for formation of aligned zinc oxide nanowires," J Cryst Growth 258(3-4), 342-348 (2003)

131. M. H. Huang, S. Mao, H. Feick, H. Q. Yan, Y. Y. Wu, H. Kind, E. Weber, R. Russo and P. D. Yang, "Room-temperature ultraviolet nanowire nanolasers," Science 292(5523), 1897-1899 (2001)

132. F. Xu, Z. Y. Yuan, G. H. Du, T. Z. Ren, C. Bouvy, M. Halasa and B. L. Su, "Simple approach to highly oriented ZnO nanowire arrays: large-scale growth, photoluminescence and photocatalytic properties," Nanotechnology 17(2), 588-594 (2006)

133. E. Comini, G. Faglia, G. Sberveglieri, Z. W. Pan and Z. L. Wang, "Stable and highly sensitive gas sensors based on semiconducting oxide nanobelts," Appl Phys Lett 81(10), 1869-1871 (2002)

134. M. C. Jeong, B. Y. Oh, O. H. Nam, T. Kim and J. M. Myoung, "Three-dimensional ZnO hybrid nanostructures for oxygen sensing application," Nanotechnology 17(2), 526-530 (2006)

135. M. H. Huang, Y. Y. Wu, H. Feick, N. Tran, E. Weber and P. D. Yang, "Catalytic growth of zinc oxide nanowires by vapor transport," Adv Mater 13(2), 113-116 (2001)

136. P. D. Yang, H. Q. Yan, S. Mao, R. Russo, J. Johnson, R. Saykally, N. Morris, J. Pham, R. R. He and H. J. Choi, "Controlled growth of ZnO nanowires and their optical properties," Adv Funct Mater 12(5), 323-331 (2002)

137. E. C. Greyson, Y. Babayan and T. W. Odom, "Directed growth of ordered arrays of small-diameter ZnO nanowires," Adv Mater 16(15), 1348-+ (2004)

138. H. J. Fan, B. Fuhrmann, R. Scholz, F. Syrowatka, A. Dadgar, A. Krost and M. Zacharias, "Well-ordered ZnO nanowire arrays on GaN substrate fabricated via nanosphere lithography," J Cryst Growth 287(1), 34-38 (2006)

139. Y. W. Heo, V. Varadarajan, M. Kaufman, K. Kim, D. P. Norton, F. Ren and P. H. Fleming, "Site-specific growth of Zno nanorods using catalysis-driven molecular-beam epitaxy," Appl Phys Lett 81(16), 3046-3048 (2002)

140. Z. M. Zhu, T. L. Chen, Y. Gu, J. Warren and R. M. Osgood, "Zinc oxide nanowires grown by vapor-phase transport using selected metal catalysts: A comparative study," Chem Mater 17(16), 4227-4234 (2005)

141. W. Lee, M. C. Jeong and J. M. Myoung, "Evolution of the morphology and optical properties of ZnO nanowires during catalyst-free growth by thermal evaporation," Nanotechnology 15(11), 1441-1445 (2004)

142. J. F. Conley, L. Stecker and Y. Ono, "Directed assembly of ZnO nanowires on a Si substrate without a metal catalyst using a patterned ZnO seed layer," Nanotechnology 16(2), 292-296 (2005)

143. L. S. Wang, X. Z. Zhang, S. Q. Zhao, G. Y. Zhou, Y. L. Zhou and J. J. Qi, "Synthesis of well-aligned ZnO nanowires by simple physical vapor deposition on c-oriented ZnO thin films without catalysts or additives," Appl Phys Lett 86(2), - (2005)

144. J. S. Jie, G. Z. Wang, Y. M. Chen, X. H. Han, Q. T. Wang, B. Xu and J. G. Hou, "Synthesis and optical properties of well-aligned ZnO nanorod array on an undoped ZnO film," Appl Phys Lett 86(3), - (2005)

145. A. Sekar, S. H. Kim, A. Umar and Y. B. Hahn, "Catalyst-free synthesis of ZnO nanowires on Si by oxidation of Zn powders," J Cryst Growth 277(1-4), 471-478 (2005)

146. J. B. Baxter and E. S. Aydil, "Epitaxial growth of ZnO nanowires on a- and c-plane sapphire," J Cryst Growth 274(3-4), 407-411 (2005)

147. W. I. Park and G. C. Yi, "Electroluminescence in n-ZnO nanorod arrays vertically grown on p-GaN," Adv Mater 16(1), 87-+ (2004)

148. S. Y. Li, P. Lin, C. Y. Lee and T. Y. Tseng, "Field emission and photofluorescent characteristics of zinc oxide nanowires synthesized by a metal catalyzed vapor-liquid-solid process," J Appl Phys 95(7), 3711-3716 (2004)
149. P. X. Gao, J. Liu, B. A. Buchine, B. Weintraub, Z. L. Wang and J. L. Lee, "Bridged ZnO nanowires across trenched electrodes," Appl Phys Lett 91(14), - (2007)
150. J. B. K. Law and J. T. L. Thong, "Lateral ZnO nanowire growth on a planar substrate using a growth barrier," Nanotechnology 18(5), - (2007)
151. Y. Qin, R. S. Yang and Z. L. Wang, "Growth of Horizonatal ZnO Nanowire Arrays on Any Substrate," J Phys Chem C 112(48), 18734-18736 (2008)
152. J. S. Lee, M. S. Islam and S. Kim, "Direct formation of catalyst-free ZnO nanobridge devices on an etched Si substrate using a thermal evaporation method," Nano Lett 6(7), 1487-1490 (2006)
153. H. Tang, J. C. Chang, Y. Y. Shan, D. D. D. Ma, T. Y. Lui, J. A. Zapien, C. S. Lee and S. T. Lee, "Growth mechanism of ZnO nanowires via direct Zn evaporation," J Mater Sci 44(2), 563-571 (2009)
154. Z. W. Pan, J. D. Budai, Z. R. Dai, W. J. Liu, M. P. Paranthaman and S. Dai, "Zinc Oxide Microtowers by Vapor Phase Homoepitaxial Regrowth," Adv Mater 21(8), 890-+ (2009)
155. S. N. Cha, B. G. Song, J. E. Jang, J. E. Jung, I. T. Han, J. H. Ha, J. P. Hong, D. J. Kang and J. M. Kim, "Controlled growth of vertically aligned ZnO nanowires with different crystal orientation of the ZnO seed layer," Nanotechnology 19(23), - (2008)
156. V. A. L. Roy, A. B. Djurisic, W. K. Chan, J. Gao, H. F. Lui and C. Surya, "Luminescent and structural properties of ZnO nanorods prepared under different conditions," Appl Phys Lett 83(1), 141-143 (2003)
157. H. Kim and W. Sigmund, "ZnO nanocrystals synthesized by physical vapor deposition," J Nanosci Nanotechno 4(3), 275-278 (2004)
158. L. Feng, C. Cheng, M. Lei, N. Wang and M. M. T. Loy, "Spatially resolved photoluminescence study of single ZnO tetrapods," Nanotechnology 19(40), - (2008)
159. D. S. Kim, U. Gosele and M. Zacharias, "Surface-diffusion induced growth of ZnO nanowires," J Cryst Growth 311(11), 3216-3219 (2009)
160. S. Rackauskas, A. G. Nasibulin, H. Jiang, Y. Tian, G. Statkute, S. D. Shandakov, H. Lipsanen and E. I. Kauppinen, "Mechanistic investigation of ZnO nanowire growth," Appl Phys Lett 95(18), - (2009)
161. R. S. Wagner and W. C. Ellis, "Vapor-Liquid-Solid Mechanism of Single Crystal Growth (New Method Growth Catalysis from Impurity Whisker Epitaxial + Large Crystals Si E)," Appl Phys Lett 4(5), 89-& (1964)
162. S. S. Brenner and G. W. Sears, "Mechanism of Whisker Growth .3. Nature of Growth Sites," Acta Metall Mater 4(3), 268-270 (1956)

VITA

Bing Hu was born on 3rd June, 1977 in Xuzhou, Jiangsu, China. He completed his high school from XuZhou No.1 Middle School, Xuzhou in 1995. He obtained a bachelor degree of science in Chemical Physics from University of Science and Technology of China, Hefei in year 2000 and a master degree of engineering in Materials Chemistry from Shanghai Institute of Ceramics, Chinese Academy of Sciences, Shanghai in 2003. Then, he became a process engineer at Grace Semiconductor Manufacturing Corp., Shanghai in 2003-2004.

Publications

1. Bing Hu, Xin Zhan, Jingyuan Yao, Bruce J. Hinds, “Molecular transport at the exposed edge of Au/SAM/Al_2O_3/Au tunnel junctions”, preparing.

2. Bing Hu, Bruce J. Hinds, “Photocurrent enhancement of Copper (II) Phthalocyanine film on nano-gap electrodes”, *IEEE Transactions on Nanotechnology,* revised.

3. Bing Hu, Nitin Chopra, Bruce J. Hinds, “Selective Lateral ZnO Nanowire Growth by Surface Diffusion on nm-Scale Patterned Alumina on Silicon”, *Journal of Materials Research,* accepted.

4. Bing Hu, Jingyuan Yao, Bruce J. Hinds, “Au/Al_2O_3/Au tunnel junctions grown by atomic layer deposition on self-assembled monolayer’, *Applied Physics Letters,* 2010, 97, 203111 (1-3).

5. Xinghua Sun, Bing Hu, Xin Su and Bruce J. Hinds, "Manipulation of molecular transport using electrochemically generated nanobubbles confined in porous alumina membrane", *ACS Nano*, ready for submission.

6. Nitin Chopra, Bing Hu, Bruce J. Hinds, "Selective growth and kinetic study of copper oxide nanowires from patterned thin-film multilayer structures", *Journal of Materials Research*, 2007, 22, 2691-2699.

7. Bing Hu, Jianlin Shi, "Synthesis and characterization of lanthanide-containing MCM-41 molecular sieves", *Journal of Inorganic Materials*, 2004, 19, 329-334.

8. Xueguo Zhao, Jianlin Shi, Bing Hu, Lingxia Zhang and Zile Hua, "In situ formation of silver nanopaticles inside pore channels of ordered mesoporous silica", *Materials Letters*, 2004, 58, 2152-2156.

9. Bing Hu, Jianlin Shi, "A novel MCM-41 templet route to Eu8(SiO4)6 crystalline nanorods in silica with enhanced luminescence", *Journal of Materials Chemistry*, 2003, 13, 1250-1252.

10. Xueguo Zhao, Jianlin Shi, Bing Hu, Lingxia Zhang, "Confinement of Cd3P2 nanoparticles inside the pore channels of MCM-41", *Journal of Materials Chemistry*, 2003, 13, 399-403.